Enhancing EPR Capabilities: From ^{19}F-ENDOR Refinement to Extreme Condition Measurements and Sensitivity Improvements

Dissertation submitted for the degree:

Doctor of Natural Science

Faculty of Chemistry and Chemical Biology

Technical University Dortmund

Submitted by

Simon Lennard Schumann

Dortmund, January 2025

The Doctor Thesis research has been performed from January 2021 till September 2024 at the Faculty of Chemistry and Chemical Biology at the Technical University Dortmund and has been examined by a committee as follows:

Principal advisor: **Prof. Dr. Müge Kasanmascheff**
Faculty of Chemistry and Chemical Biology
Technical University Dortmund

Second Examiner: **Prof. Dr. Guido Clever**
Faculty of Chemistry and Chemical Biology
Technical University Dortmund
Submission Date: **10.01.2025**

Abstract

Electron paramagnetic resonance (EPR) spectroscopy is a technique with many different application fields. It is gaining popularity in medicine, material science, and biochemistry. As EPR was further established in other research fields, several new methodologies arose. Over the years, methods have been developed to detect interactions between two paramagnetic centers and a paramagnetic center and a magnetic nucleus. These diverse methodologies allow for structural and function analysis through distance measurements and coupling analysis.

The need for higher precision measurements of minimal distances grew, and methods were developed and employed to satisfy this need. This thesis modifies ^{19}F ENDOR measurements for very short distances from 94 GHz to 34 GHz, enhancing the technique's accessibility for a broader scientific audience. It also investigates DNA G-quadruplexes (GQ), which are critical to essential biological processes such as telomerase maintenance and gene expression. This research showcases the successful application of the ^{19}F-ENDOR methodology at 34 GHz, overcoming the limitations posed by the complexity and scarcity of higher-frequency spectrometers. Notably, the approach retains sensitivity and orientational resolution, enhancing our understanding of GQs and expanding the methodological toolbox for studying other macromolecules.

Furthermore, analyzing biological processes sometimes means looking outside the established boundaries. In some cases, life exists in extreme environments that are not easily reproduced in lab scenarios, like high-pressure deep-sea environments, and are not always reliant on abundant amounts of substances; in some cases, a low amount of molecules can already change biological function. Both of these edge cases are not easily accessible for EPR spectroscopy. A robust high-pressure EPR setup for pressures up to 4 kbar was constructed and tested during this thesis. This not only allows for basic EPR experiments but also opens the door to the full variety of dipolar spectroscopy methods available in EPR by following an out-of-spectrometer approach. This allows the application to be independent of the later spectrometer setup, simplifying the application drastically. Additionally, a high-sensitivity resonator with an extra large sample entrance for microwave and radio frequency double resonance experiments was built and established to allow for measurements of very low-concentration samples that were not feasible in a timely manner with commercially available resonators.

Zusammenfassung

Die paramagnetische Elektronenresonanzspektroskopie (EPR) ist eine Technik mit vielen verschiedenen Anwendungsbereichen. Sie wird in der Medizin, den Materialwissenschaften und der Biochemie immer häufiger verwendet. Durch die steigende Verbreitung der EPR Spektroskopie in anderen Forschungsbereichen entstanden mehrere neue Methoden.

Der Bedarf an präziseren Messungen minimaler Abstände wuchs, und es wurden Methoden entwickelt und eingesetzt, um diesen Bedarf zu decken. In dieser Arbeit wurde die Anwendung von ^{19}F ENDOR-Messungen für diese sehr kurzen Entfernungen bei 94 GHz auf 34 GHz übertragen, um die Nutzung der Technik für ein breiteres wissenschaftliches Publikum zu ermöglichen, und mit der Erforschung von DNA-G-Quadruplexen kombiniert, die aufgrund ihrer Beteiligung an entscheidenden biologischen Prozessen wie der Telomerase-Erhaltung und der Genexpression von großem Interesse sind. Diese Forschungsarbeit zeigt die erfolgreiche Anwendung der ^{19}F-ENDOR-Methode bei 34 GHz und überwindet die Einschränkungen, die sich aus der Komplexität und dem Mangel an Spektrometern mit höheren Frequenzen ergeben. Vor allem behält der Ansatz die Empfindlichkeit und die Orientierungsauflösung bei, was unser Verständnis von GQs verbessert und den methodischen Werkzeugkasten für die Untersuchung anderer Makromoleküle erweitert.

Außerdem bedeutet die Analyse biologischer Prozesse manchmal, dass man über die etablierten Grenzen hinausschauen muss. In einigen Fällen findet Leben in extremen Umgebungen statt, die in Laborszenarien nicht einfach reproduziert werden können, wie z. B. die Hochdruck-Tiefseeumgebungen, und sie sind nicht immer auf große Mengen von Substanzen angewiesen; in einigen Fällen kann bereits eine geringe Menge von Molekülen die biologische Funktion verändern. Beide Grenzfälle sind für die EPR-Spektroskopie nicht einfach zu untersuchen. Im Rahmen dieser Arbeit wurde ein robuster Hochdruck-EPR-Aufbau für Drücke bis zu 4 kbar konstruiert und getestet. Dies ermöglicht nicht nur grundlegende EPR-Experimente, sondern öffnet auch die Tür zur gesamten Vielfalt der dipolaren Spektroskopiemethoden, die in der EPR zur Verfügung stehen, indem ein Out-of-Spectrometer-Ansatz verfolgt wird. Dadurch wird die Anwendung unabhängig vom späteren Spektrometeraufbau, was diese drastisch vereinfacht. Darüber hinaus wurde ein hochempfindlicher Resonator mit einem extra großen Probeneingang für Mikrowellen- und Radiofrequenz-Doppelresonanzexperimente gebaut und etabliert, um Messungen an sehr niedrig

konzentrierten Proben zu ermöglichen, die mit Standard-Bruker-Resonatoren nicht in angemessener Zeit durchführbar waren.

List of Publications and Presentations

Publications:

- **S. L. Schumann**, S. Kotnig, Y. Kutin, M. Drosou, L. M. Stratmann, Y. Streltsova, A. Schnegg, D. A. Pantazis, G. H. Clever, M. Kasanmascheff, *Chem. Eur. J.* **2023**, 29, e202302527.
- F. Attar, H. Yin, **S. L. Schumann**, J. Langley, N. Cox, Z. Zeng, K. Catchpole, S. K. Karuturi, Z. Yin, *Energy Environ. Sci.* **2024**, DOI 10.1039/d4ee00445k.
- S. A. Ekanayake, A. Seeber, J. F. Olorunyomi, H. Mai, S. Mahasivam, D. Shah, J. Lu, X. Wen, N. Sampath, **S. L. Schumann**, N. Cox, D. Chen, R. A. Caruso, *J. Mater. Chem. A* **2024**, DOI: 10.1039/d4ta01202j
- Double electron-electron resonance spectroscopy for precise reaction tracking in DNA dimerization, **2025**, in preparation
- Investigating RNR class 1a PCET pathways through the application of model substances and advanced EPR measurements, **2025**, in preparation

Oral presentations:

- Applications of ^{19}F electron-nuclear double resonance distance measurements for structure elucidation on G-Quadruplexes, Tag der Chemie, TU Dortmund, **2024**
- ^{19}F ENDOR: From proof of concept to catalytic research, RESOLV Klausurtagung 2024, **2024**
- EPR introduction and DNA G-Quadruplex structures and dynamics investigated by ^{19}F ENDOR at 34 GHz, Open faculty seminar Cox group, Australian National University Canberra AUS, **2023**

Poster presentations:

- RESOLV Klausurtagung 2021, **2021**
- 55th annual international meeting of the ESR Spectroscopy group of the Royal Society of Chemistry, St. Andrews GB, **2022**
- EUROMAR 2022, Utrecht NL, **2022**

Acknowledgments

First and foremost, I want to thank my supervisor, Prof. Dr. Müge Kasanmascheff. She always supported me with my studies during my bachelor's, master's, and PhD studies in her lab. I was allowed a vast amount of freedom on what I worked on and how without any interference from her, while she was always available for questions. I’m very grateful she enabled me to visit the ANU in Canberra as a visiting researcher during my PhD studies to further broaden my knowledge of EPR techniques and spectrometer hardware. She trusted me enough to not only plan but also supervise the reconstruction of her EPR labs, and included me in various teaching roles over the years, which I am very honored by.

I also want to extend my gratitude to Prof. Dr. Guido Clever, who served as my second supervisor. He provided me with the opportunity to work on the DNA G-quadruplexes and MetalloDNAzymes developed by his group, a collaboration that has been incredibly productive. This success is not only due to his guidance but also to the contributions of his past and present group members, who provided the necessary samples for my investigations. I am particularly grateful to Simon Kotnig for his ideas and stimulating discussions that led to new approaches and projects, as well as his consistent and timely production of the desired samples.

Furthermore, I want to thank all the past and present members of the Kasanmascheff group. Over the last seven years, it has been a constant pleasure to work with all of them in a relaxed atmosphere, help each other, and have lively conversations. I would especially like to thank Dr. Shari Meichsner for always listening and for all her advice on not only work-related topics during and after working hours, as well as Dr. Melanie Heghmanns for all the encouragement and reality checks, especially during the last year of my PhD and writing this thesis.

Finally, I want to thank my family and friends, who always supported me during my studies, even when understanding little to nothing.

I want to acknowledge the financial support by the Cluster of Excellence RESOLV, which enabled me to visit the ANU in Australia. I also want to thank Prof. Nick Cox and Martyna Judd for all their help and the warm welcome they gave me at the ANU and in their working group.

One degree later…

Dobby is free!

Table of Content

1. Introduction and Motivation

Modern science is heavily reliant on analytical techniques. Before every scientific experiment, a hypothesis is made, which needs to be confirmed. Before the rise of precise analytical methods, multiple experiments were made to exclude or confirm specific hypotheses; nowadays, science uses various powerful analytical techniques to resolve structures or processes with fewer experiments. Depending on the techniques, information that was never accessible before can now be investigated.

Nuclear magnetic resonance (NMR) is one of the most commonly used techniques in chemistry, biochemistry, and chemical physics for resolving high-resolution structures of new compounds. One drawback of NMR spectroscopy is the struggle to resolve unpaired electrons sufficiently.[1,2] Systems containing unpaired electrons are not commonly observed in chemistry for the same reason that they are of increasing interest, their high reactivity. Additionally, biochemistry has a large variety of processes heavily reliant on unpaired electron systems, like the synthesis of deoxyribonucleic acid (DNA) building blocks,[3,4] photosynthesis,[5,6] cellular respiration,[7,8] and much more. One technique specially designed to investigate unpaired electrons, their structure, and dynamics is electron paramagnetic resonance spectroscopy, shortened to EPR.[9,10]

Thereby, the applications of EPR are vast: structural determination can be done by investigating electron-electron and electron-nucleus interaction, and a multitude of techniques can observe dynamics. The opportunity to observe systems in a rigid state, solids or frozen solutions, as well as in dynamic surroundings, liquid or gas phase, enables the extraction of many parameters. EPR works by irradiation of samples with electromagnetic waves. The resolution of standard field-swept experiments can be improved partly through higher frequencies. In EPR, the most commonly used frequencies are 9.4 GHz (X-Band) and 34 GHz (Q-Band), with 94 GHz (W-Band) already being a rarely seen machine.

In the last decades, a clear trend in EPR for the use of electron-electron interaction methods, like DEER, with artificial spin labels emerged as the primary tool for distance and structural determination.[11–14] Recently, electron nuclear double resonance (ENDOR) began to move back into focus using W-Band machines and ^{19}F isotope labeling.[9,15–19] Contrary to Double Electron-Electron Resonance (DEER), which probes the interactions between two unpaired electrons, Electron Nuclear Double Resonance (ENDOR) specifically resolves the interactions between an unpaired electron and nearby magnetic nuclei, providing detailed insights into the local electronic environments. The technique is by no means a new development; already in 1988, Wells and Makinen tried ^{19}F ENDOR distance calculations,[20] and Zänker et al. implemented a version with ^{31}P in 2005.[21] Still, it went out of interest in the early 2000s due to its nuclear resolution limitation at the low-frequency machines of that time. With its ability to resolve structures below the distance limit of electron-electron interaction techniques (limited to distances > 1.5 nm[12,14]), it complements the current structural elucidation toolbox perfectly.[9,18] Furthermore, the incorporation of single isotope labels like ^{19}F is much less likely to disturb the overall structure than the incorporation of large artificial spin labels like TEMPO or even Gd-complexes.[9,18,22–24] For our research in the working group, this technique showed to be of interest. The DNA G-Quadruplex rulers, developed in cooperation with the group of Prof. Clever, are well studied in their dimerization behavior by DEER.[25–27] Still, we lacked structural information on the direct surroundings of the incorporated Cu^{2+} paramagnetic center and single G-Quadruplexes due to the DEER distance limitations. Here, as well as for the following catalytic and binding research, ENDOR distance determination is an ideal tool for structural elucidation.

Another niche application of EPR is the study of the behavior of proteins under pressure.[28–30] The approach of high pressure in a chemical context is only roughly a hundred years old, starting with the development of the *Haber-Bosch Synthesis* of Ammonia in the early 20th century.[31] From a general point of view, using high pressure often influences the energy barrier of processes and can lead to the occupation of otherwise inaccessible energy states.[32–35] For industrial applications, the possible use of high pressure to accelerate or access specific processes is important.[31,36] Under these considerations, developing and applying high-pressure EPR methods are not only interesting but advantageous as catalytic processes often involve paramagnetic[a] metal centers, which EPR ideally investigates.

---

[a] Paramagnetism is a form of magnetism due to the presence of unpaired electrons in the material.

1.1. DNA G-Quadruplex

All living organisms are built around one essential macromolecule, the Deoxyribonucleic acid (DNA). Through biological translation and transcription into messenger ribonucleic acid (mRNA), DNA builds templates for all the protein production in the organism, acting as the genetic storage of the organism. While responsible for all life, DNA is built from four main building blocks called nucleotides bound together as a linear polymer chain. The base of each nucleotide is a desoxyribose sugar with a phosphate group at the 5' carbon atom and one of four nucleobases (adenine, guanine, cytosine, thymine) at the 1' carbon atom. The single nucleotides are connected by phosphodiester groups, formed between the phosphate group and the 3' carbon of the following nucleotide.[37]

Commonly, the best-known secondary structure of DNA is the antiparallel double helix (B-DNA), in which two complementary DNA strands coil around each other (Figure 1B). A particular hydrogen bond interactions are needed, so-called *Watson-Crick base pairing. Watson-Crick* π-stacked base pairs only appear between adenine (A) and thymine (T), as well as guanine (G) and cysteine (C), respectively (Figure 1A). For the elucidation of the DNA duplex structure, with the outwards pointing negatively charged sugar-phosphate backbone and the nearly perpendicular to the helix axis located base pairs, James Watson, Francis Crick, and Maurice Wilkins were awarded the Nobel price in Medicine or Physiology in 1962.[37–39] The *Watson-Crick base pairing* can also be observed in other secondary structure motifs of DNA, such as hairpin loops, three-way junctions, and holiday junctions (four-way junctions).[40–43]

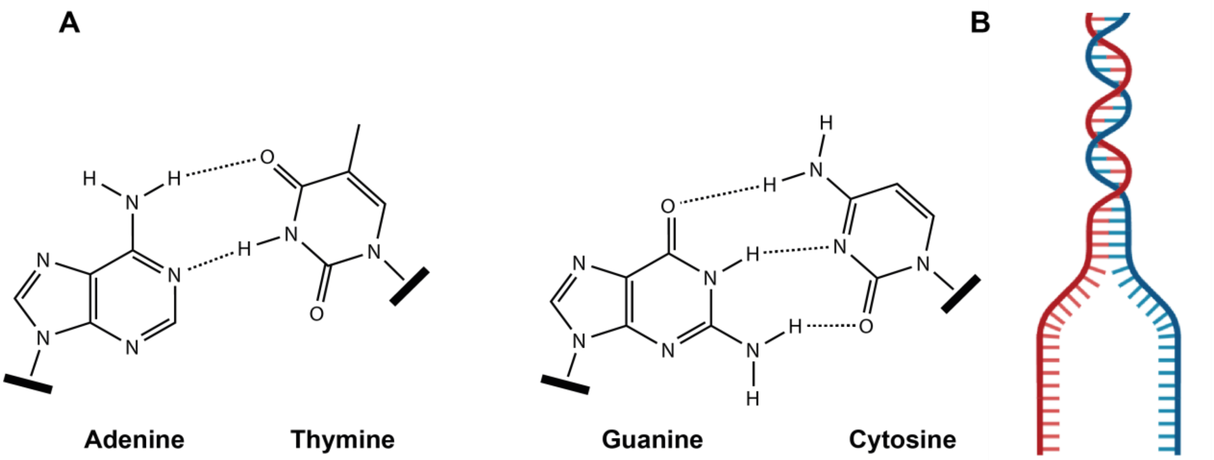

Figure 1: DNA building blocks and B-DNA structure. **A**: Nucleobase pairs of Adenine/Thymine and Guanine/Cytosine with the *Watson-Crick* hydrogen bonds marked as dashed lines. **B**: Schematic drawing of the formation of B-DNA in a cartoon fashion. Drawing generated with BioRender.

In addition to *Watson-Crick base pairs*, a different kind of hydrogen bond interaction appears in DNA strands, leading to the formation of *Hoogsteen base pairs*.[44] In these interactions, the N7 atoms of adenine and guanine serve as hydrogen bond acceptors (Figure 2A). Thus, new secondary structure motifs are formed, prominently the i-motif and G-quadruplexe (GQ).[45]

G-Quadruplexes are often formed in guanine-rich DNA sequences. The assembly can be split into two parts. The planar G-tetrads (or G-quartets) formed out of four guanine nucleobases are the basic structural motifs, which, by π-stacking, form four-stranded G-Quadruplexes (Figure 2).[45–48] To compensate for the partial negative charge from the inward-pointing carbonyl oxygen, metal ions, typically K^+ or Na^+, are localized between the stacked G-tetrads.[49] High structural diversity of G-Quadruplexes is achieved due to the different stabilizing metal ions and other parameters such as the number of G-quartets and the number of DNA strands (uni-, bi-, and tetramolecular GQs).[50] The structural diversity is further increased through differences in the loops at the ends of each GQ. The loops can differ in length, composition, and connectivity. A distinction is made between propeller-shape (double-chain-reversal), diagonal, and lateral (edgewise) loop configurations (Figure 2B). These loop configurations dictate the directionalities of the following guanines, resulting in parallel or antiparallel configurations (with respect to each other). Also, accommodating the different directions of DNA strands results in either *syn* or *anti*-conformation of the N-glycosidic bonds in the different guanosines. Overall, these conformational differences allow for many different topologies, inter alia all-parallel and antiparallel.[50–54] In general, outside influences, like pH, electrolyte and DNA concentration, cosolvents, and GQ binders, can influence the topology, as guanine-rich sequences can often adopt several different topologies due to similar energy levels.[55–61] Additionally, GQs tend to form higher-order structures such as dimers,[59,62–64] G-wires,[65,66] and other motifs, which are thought to influence their function in vivo.[67–70]

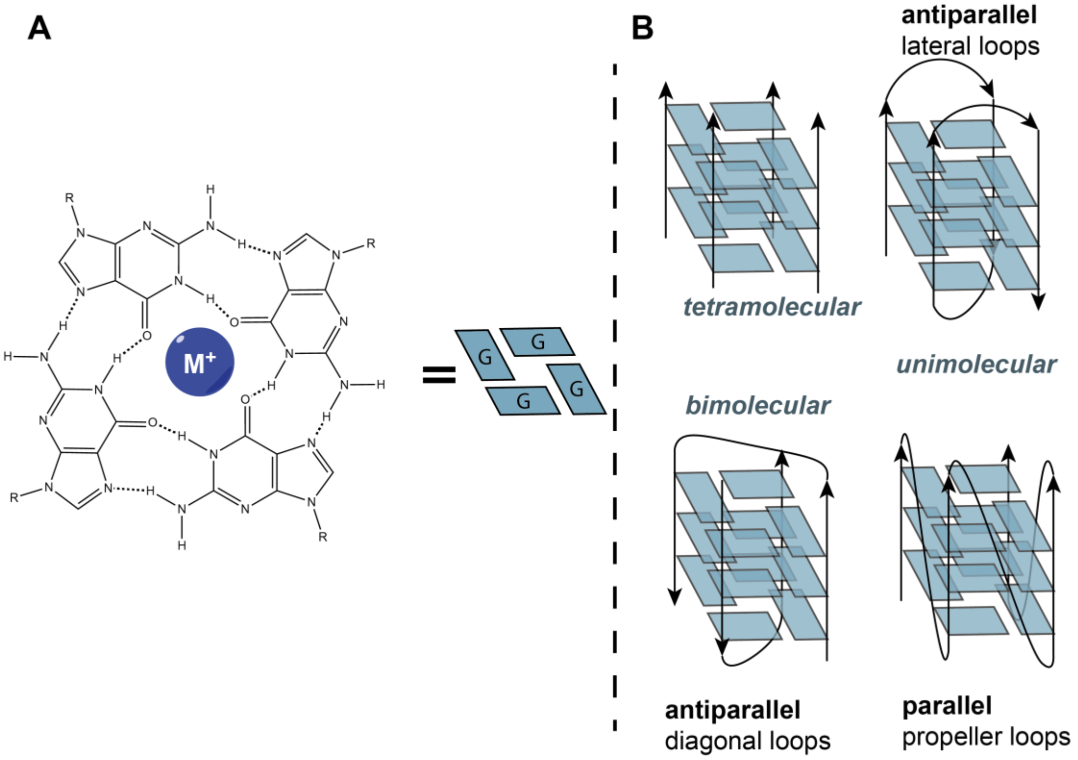

Figure 2: Structure and topology examples of G-Quadruplexes. **A**: Structure of one G-quartet with *Hoogsteen* hydrogen bonds marked as dashed lines with central alkali cation. **B**: Topologies of tetramolecular, bimolecular and unimolecular G-Quadruplexes. For uni- and bimolecular G-Quadruplexes, one example of diagonal, lateral, and propeller loops is given, as well as parallel and antiparallel DNA strand orientation. Additional strand orientations like hybrid, bulge, G-vacancy, and hairpin are not shown. Figure adapted from [71].

For quite some time, GQs were thought to appear only in lab experiments *in-vitro*, but in the 1980s, they were found in guanine-rich sequences in the telomeric ends of chromosomes.[72–75] Balasubramanian et al., in 2013, gave visual evidence of GQs in human cells by using a specifically engineered fluorescence antibody.[76,77] GQs are mainly found in promoter regions of genes, DNA replication origins, control regions of mRNA, and most prominently in telomers. All these locations indicate the important role of GQs in regulating key biological processes, like gene expression and telomeric maintenance.[54,55,78–80] It is, for example, not yet understood if and how the multitude of GQs in the direct neighborhood interact within the telomeric overhangs.[55,70,81–84] GQs have been identified as interesting drug targets in anticancer research due to their regulatory function in pathological processes.[48,85,86] Beyond their biological role, GQs gained much interest as a structural motif in the field of DNA nanotechnology.[87–89] DNA's highly predictable and programmable interactions are ideal for exploiting molecular switches and machines,[90–95] leading to the development of DNA origami in 2006.[92]

1.2. High-Pressure in Chemical Biology

In the field of chemical research, it is generally agreed that most of the fundamental principles are understood and established. Much of the research currently focuses on the supramolecular chemistry of biological molecules, polymeric macromolecules, and nanoparticles. Nevertheless, much of this research is done at or around standard conditions, while many processes that take place under extreme temperature and pressure conditions inside the earth's crust, stars, or deep inside oceans are relatively infrequently investigated.[96] Only at the beginning of the 20th century did pressure start gaining interest for chemical applications, such as the synthesis of ammonia, diamonds, and polyethylene, or the application of pressure for food conservation.[32,97,98] Besides classical chemistry, biochemistry is a field with increased interest in pressure effects. These effects can be used to investigate essential but low-populated states of proteins and enzymes.

In biological processes, structure determines function.[99] Particular conformations (foldings) of biomacromolecules (proteins, nucleosides, etc.) are known to fluctuate under normal conditions, and the low occupancy of higher-energy conformations of the native state makes them hard to investigate (Figure 3).[100–103] While well-ordered native state predominates for many proteins under normal conditions, higher energy states may be required for their biological function,[99,104] like in the case of ubiquitin binding to the Cin85 protein[105] or enzymatic activity of, for example, dihydrofolate reductase[106] and protein folding.[99,107] Not only the structural changes during the transition to a higher energy excited state, like local unfolding or rigid-body motion,[107–110] but also the timescale of transition might be relevant to protein function.[111]

These excited states often have only a few kcal/mol higher energy than the native states, making them difficult to investigate.[29] The different states can be accessed via either chemical or physical perturbation, like pH, ionic strength, chemical denaturation (e.g., urea), the addition of small molecules, temperature, or the above-mentioned pressure. Pressure effects are especially interesting as small energy differences are often difficult to access by temperature or chemical means.[103,112–115]

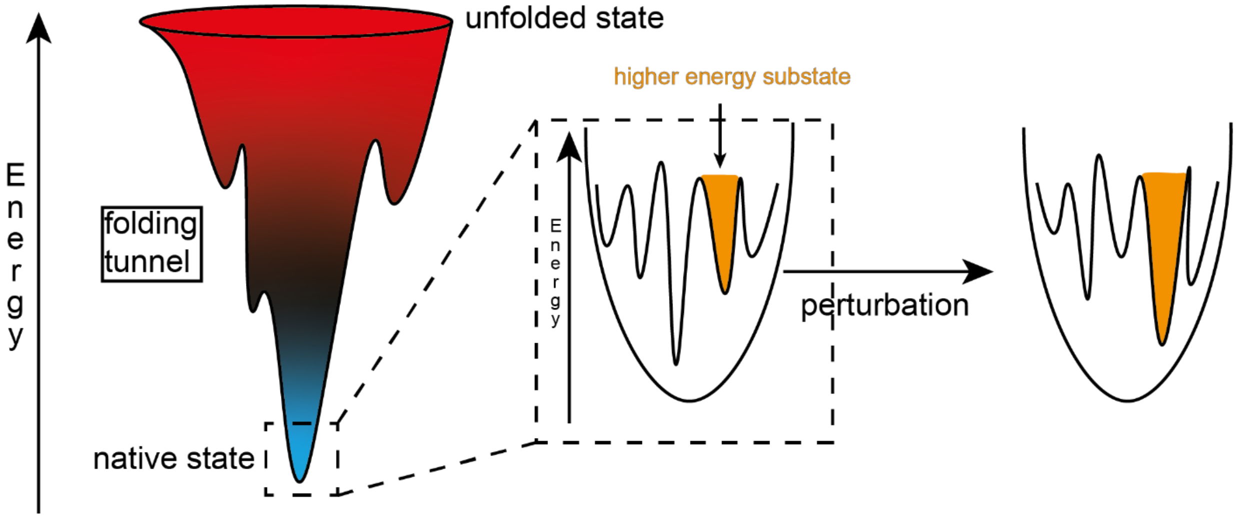

Figure 3: Simplified illustration of the energy landscape of proteins. Insert shows the conformational substates inside the protein's native state. The energy landscape can be manipulated through different perturbation methods to facilitate the occupation of higher energy conformations. Figure adapted from Ref.[103]

High pressure helped to investigate folding intermediates and low-lying excited states with functional roles.[115–118] This effect is facilitated as proteins in solution fluctuate in their energy and volume, differentiating folded, partly folded, and unfolded conformations. Studies in this field are most often done in a pressure range from 1 bar to 10 kbar. In these ranges, only intermolecular distances, hydrophobic interactions, and conformations are affected; 10 kbar is generally not enough to affect covalent bond lengths or angles.[96,103,112,119] Oligomeric proteins tend to dissociate under pressures ranging from 1 to 2 kbar,[120] while smaller monomeric proteins typically denature within the 3 to 8 kbar range.[121,122] This suggests that pressures up to 3 kbar primarily affect the quaternary protein structures, whereas higher pressures have a greater impact on the secondary and tertiary structures. Notably, the primary structures of proteins remain unaffected by pressures up to 20 kbar.[123] The unfolding of proteins under pressure is primarily attributed to the void spaces within the protein structure, which result from imperfect packing. When pressure is applied, these void spaces are eliminated, reducing the overall system volume.[124] Water penetration into the protein interior can also weaken hydrophobic interactions, contributing to pressure-induced unfolding. Conversely, pressure-induced dissociation can be explained by the imperfect packing of atoms at the subunit interface and the disruption of polar and ionic bonds at these interfaces, ultimately leading to negative volume changes.[123]

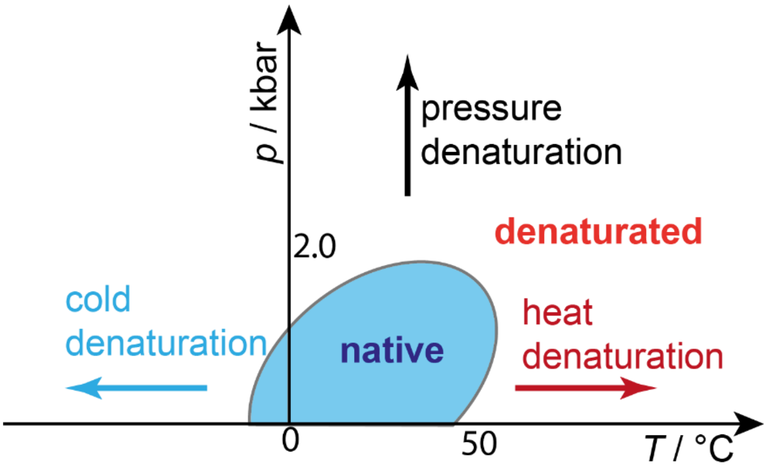

Figure 4: Theoretical temperature-pressure stability phase diagram of an oligomeric protein. Adapted from Ref.[112]

The volume of a protein is largely determined by the size of its individual atoms, the empty spaces within its internal cavities, and the impact of solvation by peptide bonds and amino acid side chains. When applied, pressure can lead to significant changes in the protein's structure, inducing local and global conformational alterations as well as subunit dissociation and association processes. These changes ultimately result in the protein's denaturation (Figure 4).

Not only is the investigation of higher energy states of proteins interesting for understanding their function and structure, reaction acceleration or tuning are subjects gaining interest for biomolecular-based industrial processes.

1.3. High-Pressure equipment in EPR

High-pressure setups are commonly used for different spectroscopic methods, such as NMR, Fourier-transform infrared spectroscopy, or circular dichroism spectroscopy.[115,121] Multiple different, very specific setups have been developed for EPR spectroscopy. The development focuses on three system types: solid-state applications, primarily used in physics; liquid state; and frozen solution, the latter two used primarily in chemistry and biochemistry for protein research.[29,30,125–128] For solid-state applications, anvil or diamond pressure cells generate pressure by mechanical compression and are integrated into special or commercial resonators,[126,127,129] or the investigation is performed on standard atmospheric EPR spectrometers for solids generated under high-pressure when stable under atmospheric pressure.[130] A further unique application is high-pressure generated by supercritical CO_2 in a specially designed pressure cell; in this case, the CO_2 is not only the pressure medium but also the solvent.[125]

Two magnetic resonance groups are known especially for liquid state and frozen solution applications: the Akasaka group[108,115–118,131] in the field of NMR spectroscopy and the Hubbell group [28–30,128,132,133] in EPR spectroscopy. For EPR, two types of liquid pressure cells are used, most commonly for experiments with site-directed spin labeling by the Hubbell group. The first is made of a fused silica capillary, which is polytetrafluoroethylene-coated (PTFE) and folded into bundles containing 15-25 loops. These bundles are fragile, and handling is difficult to avoid scratching when inserted into 5 mm outer diameter (OD) NMR/EPR tubes (Figure 5A).[28] One end of the capillary is sealed while the other is connected to a pressure intensifier, allowing pressures of roughly 4 kbar. The advantage of this technique is the use of standard tubes and EPR resonators. A disadvantage is the small sample volume; due to the folding and material of the fused silica capillary, the sample volume in a standard X-band Bruker resonator (tube size 5 mm OD) is less than 2 µL, making high sample concentrations necessary. This disadvantage could be minimized by using higher frequencies and capillaries in different sizes,[29] as capillaries with 1.6 mm OD could be used in standard Bruker D2 Q-Band resonators without additional EPR tubes and folding. Alternatively, an experimental but commercially available yttria-stabilized zirconia ceramic cell (HUB440-Cer, Pressure BioScience, Inc.) can be used with a custom-made resonator from Bruker (ER4123D) (Figure 5B).[134]

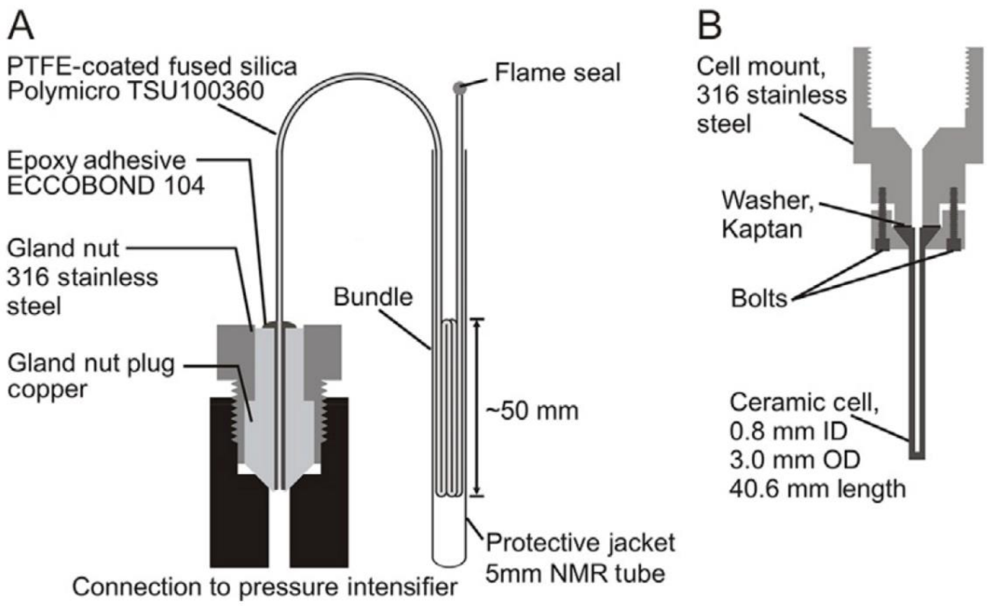

Figure 5: High-pressure cells for liquid state EPR measurements. **A**: PTFE-coated fused silica bundles inside a 5 mm OD EPR tube. The sample is filled into the fused silica capillary before insertion. **B**: yttria-stabilized zirconia ceramic pressure cell. Both cells mainly find application in continuous wave X-Band EPR. Figure taken and modified from Ref.[29] under the RightsLink license number 5942930825598.

The sample volume of around 5 µL is higher, allowing the concentration to be reduced to roughly 200 µM for a satisfying signal-to-noise ratio (SNR). Depending on the specific cells, a pressure of around 2.4 kbars can be achieved. A larger disadvantage is the strong background signal exhibited by the cell. The pressure-independent signal overlaps with a typical nitroxide spectrum at different pressure values.[29] Both high-pressure cell versions are currently mainly used for continuous wave X-band measurements.[29] Standardized connectors connect the cells to different pressure intensifiers.

For pulse EPR applications and advanced EPR experiments, the tumbling and relaxation properties of the paramagnetic centers in solution are problematic due to averaging out of most interactions. Therefore, these samples are often frozen to gain better insight into additional properties like hyperfine coupling or distance measurements like DEER depending on dipolar interaction, which is averaged out in fast-tumbling environments (Chapter 3.1). The previously described equipment is not applicable to these measurements as the sample inside a standard resonator is inside an additional Helium-flow cryostat, making high-pressure connections and nearly all pressure media (besides Helium gas itself) impossible. Therefore, an alternative approach was developed: freezing the investigated sample under high-pressure conditions (Figure 6).[133]

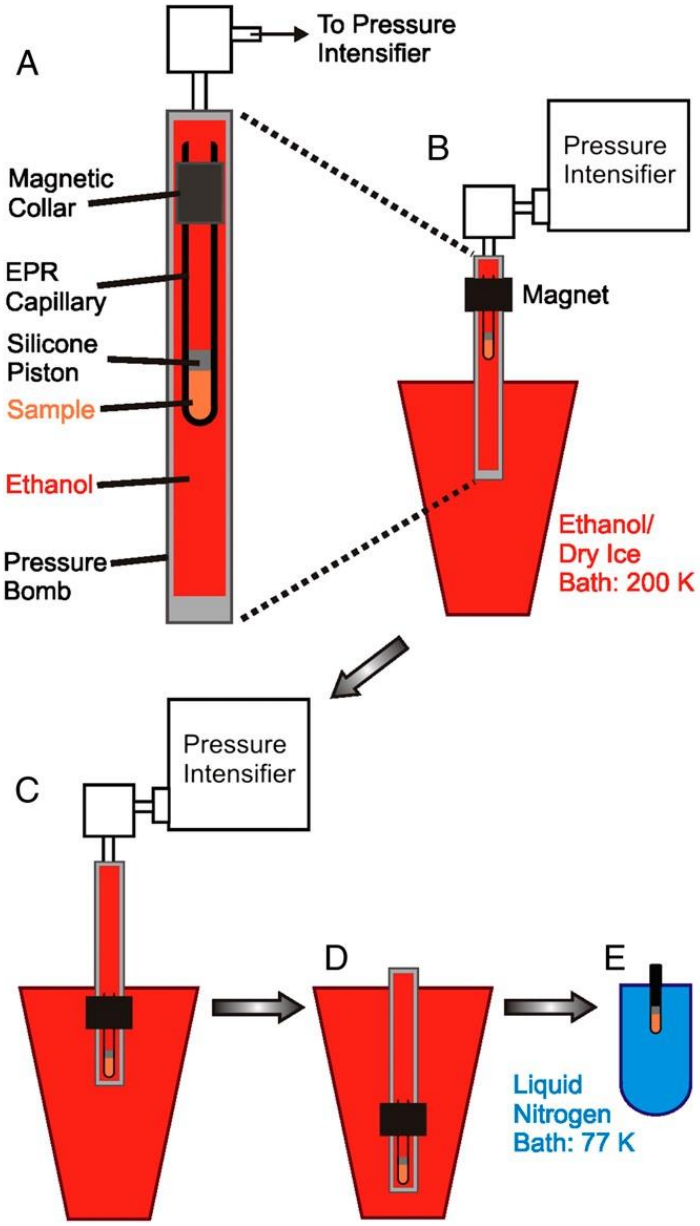

Figure 6: Principle of freezing EPR samples under pressure. **A**: Schematic drawing of the full pressure cell with an EPR tube inside. The tube has a silicon piston inside to separate pressure media and sample solvent. Additionally, a magnetic ring is attached. Pure ethanol is used as a pressure medium. **B**: The pressure cell is attached to a pressure intensifier and halfway inserted into a dry ice ethanol bath. **C**: After pressure generation, the sample is lowered to the bottom of the pressure cell with the help of magnets and the metal ring. **D**: the pressure cell is fully immersed in the cooling bath to freeze the sample fully. **E**: After releasing the pressure, the frozen sample is transferred to liquid nitrogen for storage or transfer into the EPR spectrometer.

The principle is based on the condition that water solvents (buffers) are used to trap high-pressure conformations. The samples are filled into borosilicate capillary cells, which act as EPR tubes, and sealed with silicon pistons before the cells are filled with ethanol (Figure 6A).

In this case, the ethanol acts as the pressurizing medium, and freezing is achieved by insertion into an ethanol/dry ice bath. The water-based sample will thereby fully freeze in a stiff matrix while the ethanol stays liquid, allowing it to get the sample out after pressurization. To pressurize the sample, the capillary is inserted with a metal collar into a pressure bomb (cylindric pressure cell), connected to a pressure intensifier, and halfway submerged in the ethanol/dry ice cooling bath (Figure 6B). Due to the metal collar, the sample can be moved from the outside, allowing it to be lowered into the cooled part of the pressure bomb after pressurization for freezing. After freezing, the pressure is relieved, and the sample can be either transferred to the spectrometer for low-temperature measurements or to liquid nitrogen for storage (Figure 6C-E). Therefore, it is crucial to keep the sample below the glass transition temperature of the investigated system to prevent it from relaxing out of the high-pressure configuration.[134,135] A quick transition to liquid nitrogen is thereby advised.[133]

1.4. Motivation

Electron paramagnetic resonance spectroscopy has only been employed for roughly 80 years and is still under constant development. Higher frequencies, new measurement approaches, and utterly new measurement techniques are continuously developed. Many of these cases have very specific uses and are not widely applied for one reason or another. One of life's most crucial building blocks, the DNA, still has many unknown interactions and functions in its different secondary structures outside the well-known B-DNA. This work investigates DNA G-quadruplexes, a secondary structural motif often related to cancer drug research and possible use in metalloDNAnzymes. To enable investigations of Angström distance resolutions, the relatively new technique of ^{19}F ENDOR measurements is ideal but needs to be adjusted and implemented for 34 GHz spectrometers. This research should not only shed light on these vital DNA structures but also help to establish a novel and powerful technique, before only used on rare 94 GHz spectrometers, for a broader scientific audience at 34 GHz.

Further, establishing high-pressure EPR equipment was necessary to investigate the tuning of midpoint potentials for higher H_2 production in Fdx1 by high pressure. While some high-pressure measurements were performed in EPR, a commercially available method has yet to be established. This work should demonstrate a simple but reliable way to pressurize EPR samples up to 4 kbar for all available EPR methods. This allowed investigations on the promising Fdx1 protein for industrial H_2 production through biocatalysts. For this purpose, an additional new EPR resonator was built and tested in cooperation with the working group of Prof. Nick Cox at the Australian National University in Australia. This should allow one sample to be used in all our commercially available EPR spectrometers and methods under atmospheric and high-pressure conditions.

As identified in the preceding sections, the limitations in current EPR techniques for studying DNA G-Quadruplexes and high-pressure effects on proteins highlight significant gaps in our understanding. The following theory and methodology section details the advanced EPR techniques, including 19F ENDOR and high-pressure protein research, specifically chosen to address these gaps.

2. Theory on high pressure in proteins

Chemical reaction rates and equilibria can be manipulated using high pressure following the application of *Le Chatelier's* principle. Therefore, reactions always tend to go toward the smaller volume.[136]

In general, the change in the free Gibbs energy ΔG in equilibrium state determined by the thermodynamical quantities of entropy S and internal energy U is given as:

$$\Delta G = -RTln(K) = \Delta U + p\Delta V - T\Delta S \tag{1.1}$$

Connected by the gas and equilibrium constants R and K, respectively, as well as the volume V and the temperature T.[121] The direct pressure effect on the volume is apparent, and the impact at equilibrium between two distinct states is given by the volume difference ΔV:

$$\Delta V = V_B - V_A = \left(\frac{\partial \Delta G}{\partial p}\right)_T = -RT\left(\frac{\partial \ln(K)}{\partial p}\right)_T. \tag{1.2}$$

A change in conformation population towards higher energy states can be obtained if ΔV is sufficiently negative and stable conformers are trapped under pressure. As mentioned before, 2 kbar can be enough to denature some proteins. Under physiological conditions, the free Gibbs energy is slightly positive, as the native state is more stable than the unfolded one. Typical globular proteins with a volume difference of -20 to -100 cm^3 mol^{-1} (when compressed) get denatured at 2 kbar as ΔG will get slightly negative.[112]

During reactions or biological activity, an activation volume $\Delta V^\#$ can be written with the rate constant k:[137]

$$\Delta V^\# = -RT\left(\frac{\partial \ln(k)}{\partial p}\right)_T \tag{1.3}$$

Negative activation volumes for reactions imply that the transition state has a smaller volume than the equilibrium/starting state; under increased pressure, these reactions will be accelerated, and vice versa (Figure 7).

The main effect pressure has on biomolecules is the change in hydration surrounding and interactions, like hydrogen bonding and hydrophobic interactions. Hydrogen bonds are often strengthened under pressure, while hydrophobic interactions are weakened upon compression or solvent insertion.[112]

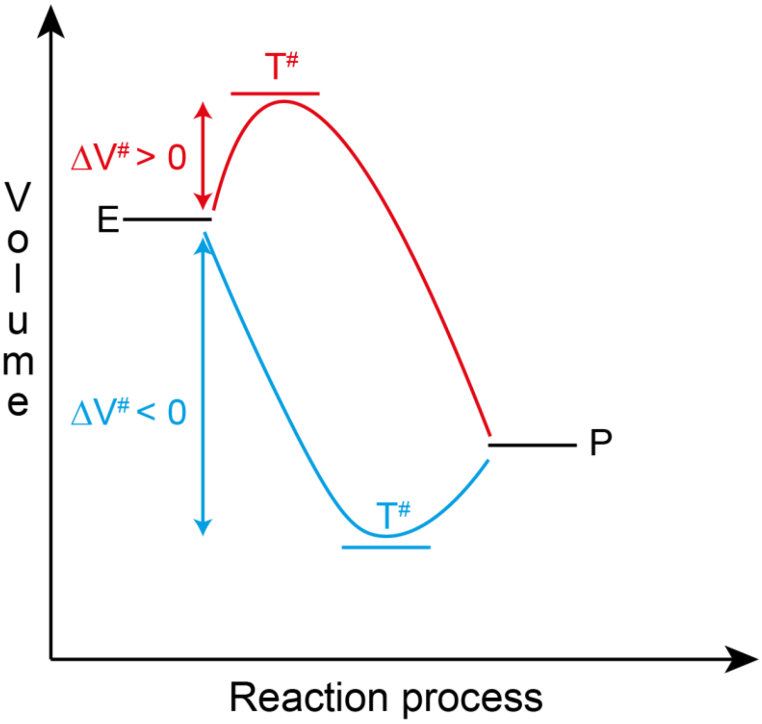

Figure 7: Reaction process profiles depending on their respective activation volumes. The reaction of the educts (E) to the products (P) via their transition state (T) is either accelerated or slowed down depending on the activation volume under pressure. Red: Positive activation volume slows down the reaction process under the effect of pressure. Blue: Negative activation volume; the reaction is accelerated.

For biochemical processes, characteristic values of ΔV and $\Delta V^{\#}$ are around +50 to −50 mL/mol.[121,138]

As the structure and folding of a protein are often ordered, the activation volume is partly influenced by intrinsic-, solvation-, and steric factors, providing information about the mechanisms of a reaction by the magnitude and sign of the activation volume. Three general propositions can be made:[112,139]

1) The activation volume is negatively influenced by associative processes, including bond formation in the rate-determining step, formation of charged species, and the volume change from the solvation of newly formed charges.
2) The activation volume is positively influenced by dissociative processes, bond breaking, and the neutralization of charges due to the relaxation of solvation.
3) In multistep reactions, the activation volume is the sum of the rate-determining step activation volume and the reaction volumes of any pre-equilibria occurring before the slower step.

3. Electron paramagnetic resonance

Electron paramagnetic resonance, or electron spin resonance (ESR), is a powerful technique for studying paramagnetic centers. In 1944, Soviet physicist *Yevgeny Zavoisky* recorded the first EPR spectrum at Kazan State University.[140] Initially, salts of different transition metal ions were mostly investigated via EPR spectroscopy.[141,142] This sensitive method is increasingly applied in various fields, such as medicine, material science, biochemistry, and others. Diverse samples, such as crystalline solids, liquid solutions, and powders, are investigated over a broad range of temperatures.[143,144]

EPR measurements are based on the following three basic requirements: a paramagnetic center in the form of an unpaired electron gets irradiated with microwaves (mw) inside an external magnetic field. Examples of unpaired electrons range from transition metal ions and amino acid radicals to more complex bioradicals.[144] Two exceptional cases in EPR spectroscopy are molecules with two or more unpaired electrons interacting, like triplet states or transition metals, and non-paramagnetic molecules. Spin labels, which are molecules with a stable unpaired electron (e.g., a TEMPO radical) and a linker to attach them to other molecules, are introduced to investigate non-paramagnetic molecules such as DNA and proteins.[24,144–148]

The following section will introduce important and necessary EPR terms and concepts for this thesis. This information is well-known textbook knowledge, such as that found in the books of Goldfarb et al.[149] and Schweiger et. al.[144].

3.1. The spin system

From the Stern-Gerlach experiment, it is known that every electron exhibits a spin angular momentum described by the spin operator $\hat{\boldsymbol{S}}$,[b] which is quantized in the units of the reduced Planck constant $\hbar$, and the primary spin quantum number S.[144,150] The spin angular momentum is often called “spin” for short. The unpaired electron of the paramagnetic center in a sample can not be seen as a “free electron”. Inside a sample, the electronic ground state of the electron is influenced by interactions with its surroundings. These interactions are described by the static spin Hamiltonian, which sums up all separate possible magnetic interaction Hamiltonians:[144]

---

[b] Operators are indicated with a circumflex, and vectors and matrixes are written in bold.

$$\hat{\mathcal{H}}_S = \hat{\mathcal{H}}_{EZ} + \hat{\mathcal{H}}_{NZ} + \hat{\mathcal{H}}_{HF} + \hat{\mathcal{H}}_{ZFS} + \hat{\mathcal{H}}_{EE} + \hat{\mathcal{H}}_{NQ} + \hat{\mathcal{H}}_{NN} \tag{2.1}$$

The Hamiltonians are, $\hat{\mathcal{H}}_{EZ}$, the *electron Zeeman interaction*, $\hat{\mathcal{H}}_{NZ}$, the *nuclear Zeeman interaction*, $\hat{\mathcal{H}}_{HF}$, the *hyperfine interaction* between the electron and a nucleus, $\hat{\mathcal{H}}_{ZFS}$, the *zero-field interaction* for *S* > 1/2, $\hat{\mathcal{H}}_{EE}$, the *electron-electron interaction* if more than one unpaired electron is in the system, $\hat{\mathcal{H}}_{NQ}$, the *nuclear quadrupole interaction* for nuclear spin *I* > 1/2 and $\hat{\mathcal{H}}_{NN}$, the *nuclear-nuclear interaction*. As many of the terms are irrelevant to the systems and applications in this work, only $\hat{\mathcal{H}}_{EZ}$, $\hat{\mathcal{H}}_{NZ}$ and $\hat{\mathcal{H}}_{HF}$ will be examined further on the following pages.

The electron, with its angular momentum as well as a mass and a nonzero charge, gives rise to a magnetic moment:

$$\boldsymbol{\mu} = -g\mu_B\boldsymbol{S}. \tag{2.2}$$

Where μ_B is the *Bohr magneton* and the factor g is a correction for the deviation between the quantum object and classical charged particle behavior. For a free electron, it is exceptionally accurately known with $g_e = 2.00231930436082(52)$,[149] while real systems derive from it. The deviation from the free electron g-factor is relatively small for organic radicals, while for transition metal ions, it can be large.

The name g-factor originates from the gyromagnetic factor in the gyromagnetic ratio $\gamma_e = -\frac{g_e\mu_B}{\hbar}$, linking the angular momentum and magnetic moment directly:

$$\boldsymbol{\mu} = \gamma_e\boldsymbol{S} \tag{2.3}$$

The interaction of the magnetic moment with an external magnetic field $\boldsymbol{B}$ is then described by the *electron Zeeman Hamiltonian*:

$$\hat{\mathcal{H}}_{EZ} = \frac{\mu_B}{\hbar}\boldsymbol{B}^T\boldsymbol{g}\hat{\boldsymbol{S}}. \tag{2.4}$$

Here the g-factor is given as a symmetric $\boldsymbol{g}$-tensor as magnetic interaction make it orientation-dependent. The electron in a sample, bound to a nucleus, exhibits spin-orbit coupling, giving rise to the effective $\boldsymbol{g}$-tensor. This coupling is unique for each paramagnetic center, resulting in a unique $\boldsymbol{g}$-tensor for a specific sample, which is often used as a fingerprint. In general, a cartesian frame is chosen as a molecular frame of reference to diagonalize the $\boldsymbol{g}$-tensor into three eigenvalues. Further the symmetry of the $\boldsymbol{g}$-tensor can be categorized into three cases: isotropic ($g_1 = g_2 = g_3$) representing the cubic symmetry, axial symmetry ($g_1 = g_2 \neq g_3$) and rhombic symmetry ($g_1 \neq g_2 \neq g_3$). All other interactions discussed here are also given in their respective cartesian frame and can be transferred to the molecular reference frame of the $\boldsymbol{g}$-tensor via rotations by three Euler angles α, β and γ.

This anisotropy is not only dependent on the electron-harboring atom but on its surroundings. Organic radicals often exhibit rhombic symmetry, while transition metal complexes with symmetric ligands are often axial or even isotropic. In a liquid solution, the anisotropy is averaged out through the rapid tumbling of the molecule, resulting in an isotropic $\boldsymbol{g}$-tensor ($g_{iso} = \frac{g_1+g_2+g_3}{3}$).

As it is only possible to determine one special component at a time, the usual convention was made that the z-component is the reference point. Therein the projection of $\hat{\boldsymbol{S}}$ results in the components $\hat{S}_x, \hat{S}_y$ and $\hat{S}_z$ ranging in their eigenvalues from $+S$ to $-S$ with $(2S+1)$ components with the restriction to their secondary magnetic quantum numbers, $m_s = \pm\frac{1}{2}$ for $S = \frac{1}{2}$.

By applying an external magnetic field, B_0, along the z-axis parallel to the S_z, the electron spin energy E can be calculated with the magnetic moment:

$$E = -\mu_z B_0 = g_e \mu_B m_S B_0. \tag{2.5}$$

According to equation 2.5, the degenerated spin states get split depending on m_S by the magnetic field (Figure 8). This splitting in the *α* (parallel) and *β* (antiparallel) energy state in the presence of B_0 is called *Zeeman* splitting.

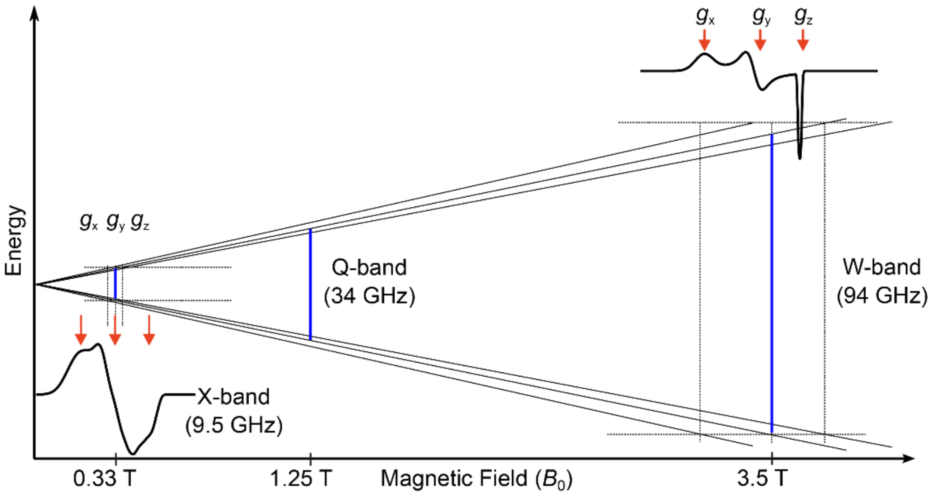

Figure 8: *Zeeman splitting* for an electron with $S = \frac{1}{2}$ in an external magnetic field B_0. The difference frequency bands are indicated inside the figure. An abortuary simulation at 9.5 GHz and 94 GHz shows an example of the separation of eigenvalues at higher fields

To induce a transition between the *α* and *β* states, the energy difference ΔE between them must equal the energy of the mw photons. Thus, an EPR transition is only induced when the irradiation frequency v fulfills the so-called the *resonance condition*:

$$hv = \Delta E = E_\alpha - E_\beta = g\mu_B B_0. \tag{2.6}$$

As the energy difference ΔE is proportional to the magnetic field B_0, different magnetic field positions require different frequencies. The energy difference can be determined by holding the mw frequency steady and sweeping the magnetic field. Both continuous wave (CW) and pulse EPR experiments are based on this principle. In contrast to pulse EPR, in CW experiments, a continuous low-power mw radiation of a fixed frequency is applied while the magnetic field is swept. The further difference between pulse and CW EPR is the modulated magnetic field. In most EPR experiments, the resonator is critically coupled, meaning that the resonator entirely absorbs the input power. If the sample now absorbs power at resonance, the resonator detunes and reflects MW power, which gets recorded. The modulation of the magnetic field in CW experiments increases the signal-to-noise ratio considerably and results in the first derivative shape of the spectrum.

As the external magnetic field lifts the degeneracy of the spin states, the spins are distributed to the different states. The population ratio between the two states is given via the *Boltzmann distribution*

$$\frac{N_\alpha}{N_\beta} = e^{\frac{-g\mu_B B_0}{k_B T}}. \qquad (2.7)$$

N_x: the number of spins in the state x; k_B: *Boltzmann* constant; T: temperature.

The *Boltzmann distribution* shows that lowering the temperature increases the population difference and the EPR signal intensity.

As briefly mentioned before, EPR experiments can be performed at different frequencies/field ranges (Figure 8). 9.5 GHz (X-band) and 34 GHz (Q-band) are commonly used. Furthermore, some high-field/high-frequency spectrometers up to 263 GHz are available, such as the commercial 95 GHz W-band spectrometer. The advantage of higher frequencies is that the resolution of g-eigenvalues is improved due to the higher separation of energy levels of the spin states (Figure 8).

For nuclear spins, the basic principle is the same. *Nuclear Zeeman effects* arise when a *nuclear spin* I, with the *nuclear spin operator* $\hat{\boldsymbol{I}}$*,* couples with the *magnetic field* $\boldsymbol{B}$:

$$\hat{\mathcal{H}}_{NZ} = -g_N \mu_N \boldsymbol{B}\hat{\boldsymbol{I}}. \qquad (2.8)$$

In this case, g_N is the nuclear g-factor, which is a constant for each isotope and not environment depended, and μ_N the nuclear magneton. This interaction is the base of the closely related NMR spectroscopy, as the g-factors are constant changes in resonance frequency through the environment are given in the form of the so-called *chemical shift*. In EPR, the *Nuclear Zeemann effect* is often not observable as these transitions are EPR forbidden. Instead, the hyperfine interaction (hf) expresses the interaction between magnetic nuclei and the electron. While at higher frequencies (≤94 GHz) *chemical shift* effects can appear, distorting the EPR line shape.[151]

3.2. Hyperfine Interactions

A nucleus in the surroundings of the electron generates an additional magnetic field, which the electron spin experiences and which is independent of the external magnetic field. This interaction is described by the *hyperfine interaction* (hf) *Hamiltonian* $\widehat{\mathcal{H}}_{HF}$.

$$\widehat{\mathcal{H}}_{HF} = \boldsymbol{\hat{S}A\hat{I}} \tag{2.9}$$

The *hyperfine coupling tensor* $\boldsymbol{A}$ can be separated into two parts. The isotropic, or *Fermi contact*, interaction $\widehat{\mathcal{H}}_F$, and the electron-nuclear dipole-dipole interaction $\widehat{\mathcal{H}}_{DD}$. In general, the coupling is always due to dipole interactions, but as there is a non-zero electron spin density at the nucleus position ($|\psi_0|^2$) this part is termed isotropic. In this case, no distance dependency occurs, and the coupling is only proportional to the nuclear spin density.

$$\widehat{\mathcal{H}}_F = a_{iso}\boldsymbol{\hat{S}\hat{I}} \tag{2.10}$$

With

$$a_{iso} = \frac{2}{3}\frac{\mu_0}{\hbar} g_e \mu_B g_n \mu_n |\psi_0|^2. \tag{2.11}$$

Thereby μ_0 being the *vacuum permeability*.

The dipolar interaction is dependent on the inter-spin vector $\boldsymbol{r}$ and is described by the orientation-dependent electron-nuclear *dipole-dipole Hamiltonian* $\widehat{\mathcal{H}}_{DD}$

$$\widehat{\mathcal{H}}_{DD} = \frac{\mu_0}{4\pi} g_e \mu_B g_n \mu_n \left[\frac{3(\boldsymbol{\hat{S}}\cdot\boldsymbol{r})(\boldsymbol{r}\cdot\boldsymbol{\hat{I}})}{r^5} - \frac{\boldsymbol{\hat{S}}\cdot\boldsymbol{\hat{I}}}{r^3}\right]. \tag{2.12}$$

The *dipole-dipole Hamiltonian* is thereby often written as:

$$\widehat{\mathcal{H}}_{DD} = \boldsymbol{\hat{S}T\hat{I}} \tag{2.13}$$

With $\boldsymbol{T}$**,** the traceless dipolar coupling tensor. By considering $\boldsymbol{T}$ in the principal axes system of the hyperfine interaction, we get the classical equation:

$$\boldsymbol{T} = \frac{\mu_0}{4\pi\hbar}\frac{g_e\mu_B g_n\mu_n}{r^3}\begin{pmatrix} -1 & & \\ & -1 & \\ & & 2 \end{pmatrix} = \begin{pmatrix} -T & & \\ & -T & \\ & & 2T \end{pmatrix}. \tag{2.14}$$

In the form of equation 2.14, the dipolar coupling tensor is only correct for distances $\gtrsim 3$ Å, as in this case, the point-dipole approximation, can be used for electrons as well as the nucleus; below 3 Å, the ground state electron spin distribution has to be taken into account. Further, this expression is strictly only correct for isotropic electron Zeeman interactions (g_{iso}), but is often used also for systems with small g anisotropy as an approximation.[9]

The hyperfine coupling tensor $\boldsymbol{A}$ is then expressed as:

$$\boldsymbol{A} = a_{iso}\begin{pmatrix} 1 & & \\ & 1 & \\ & & 1 \end{pmatrix} + \boldsymbol{T}. \tag{2.15}$$

The hyperfine interactions together with the nuclear Zeeman interaction change the energy levels of the electron in the magnetic field.

$$E_{m_S,m_I} = g\,\mu_B m_s B\, - g_N \mu_N B m_I + A m_I m_S. \tag{2.16}$$

The second term thereby describes the nuclear *Zeeman* interaction. The last term is the hyperfine interaction. It is only dependent on the magnetic quantum numbers of the nuclei and the electron and the hyperfine coupling constant A but is independent of the applied magnetic field.

The splitting of each *electron Zeeman* level with each *nuclear Zeeman* level results in $2NI + 1$ EPR lines (Figure 9, with N = 1), where N is the number of nuclei with the same hyperfine coupling value.

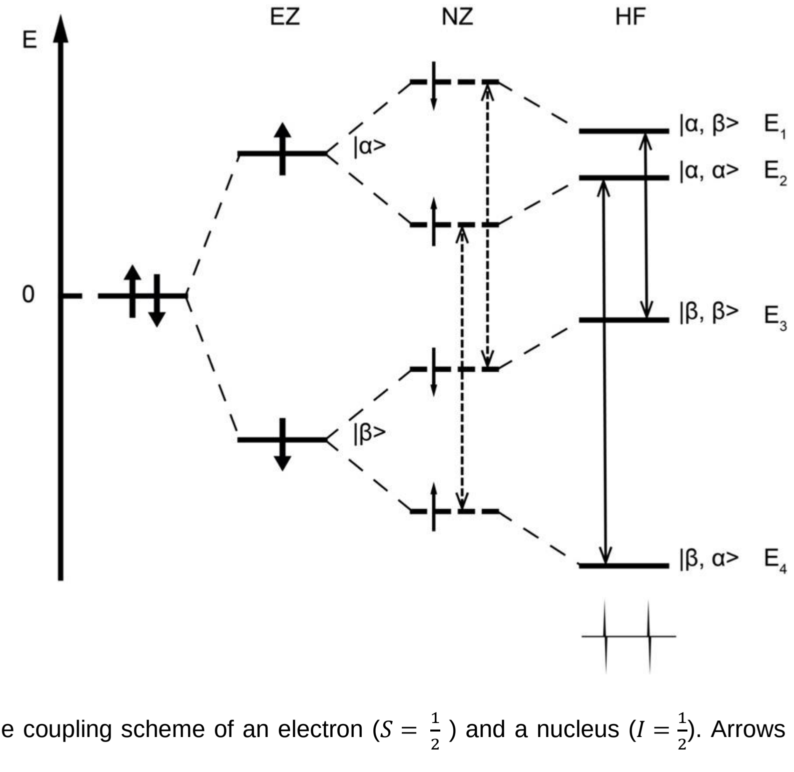

Figure 9: Hyperfine coupling scheme of an electron ($S = \frac{1}{2}$) and a nucleus ($I = \frac{1}{2}$). Arrows indicate the allowed EPR transitions.

The selection rule for allowed EPR transitions is $\Delta m_S = \pm 1$ with $\Delta m_I = 0$. The hyperfine coupling constant A can directly be obtained from the splitting between two corresponding signals in the EPR spectrum. Several peaks can overlap as a result of multiple couplings from multiple identical nuclei. In that case, the intensity of the signal is the sum of the associated signals, following the principle of the *Pascale* triangle. Similarly to the $\boldsymbol{g}$-tensor, the hyperfine coupling can be classified into two states: the isotropic and the anisotropic. Sole isotropic coupling is observed in liquid solutions, where the molecules' rapid tumbling averages out the hyperfine coupling's orientation dependence. Solid and liquid crystals, powders, and frozen solutions often have anisotropic hyperfine coupling.

3.3. EPR application

In general, EPR can be applied using two different methods: continuous wave (CW) and pulse EPR. CW EPR is the commonly used method, which applies continuous mw irradiation of low intensity to a sample. In contrast, short and powerful mw pulses are used in pulse EPR experiments.[149,152,153] The following will explain the most important pulse experiments for this thesis. As no CW measurements were made, a detailed explanation will be skipped.

3.4. The Hahn Echo Experiment

The most straightforward pulse experiment is a single mw pulse, called *free induction decay.* However, this is often unfeasible in EPR due to the spectrometer's intrinsic dead time in combination with the relaxation of the spins.[149]

The Hahn echo, also called primary electron spin echo (ESE), is the most straightforward two-pulse technique in EPR, developed and named after the physicist *Erwin Hahn* (Figure 10).[154] During the experiment, not a single but all unpaired electron spins in the sample are examined. These electron spins are summed up to the sample magnetization, which rotates around $\boldsymbol{B_0}$ like one single electron magnetic moment. Through irradiation with a $\boldsymbol{B_1}$ field (mw irradiation), the magnetization changes its direction. For a simplified presentation, the concept of a rotating frame is used. Within the rotating frame, the magnetization vector is stationary, and the frame rotates around the z-axis of the principal axis system with the *Larmor* frequency ω_L of the magnetization.[148]

$$\omega_L = -\gamma_e B_0 \tag{2.17}$$

In a pulse EPR experiment, the absorption is often not measured directly; instead, an echo is detected. A Hahn echo experiment contains a $\frac{\pi}{2}$ and a π pulse. The $\frac{\pi}{2}$ pulse, flips the magnetization by 90 degrees into the xy-plane. Afterward, the single spins start to dephase in the xy-plane due to the field inhomogeneity before the π pulse flips the system by 180 degrees. The spins are still precessing in the same direction as before. After the 180-degree flip, they gather back together after the time τ, resulting in the echo.

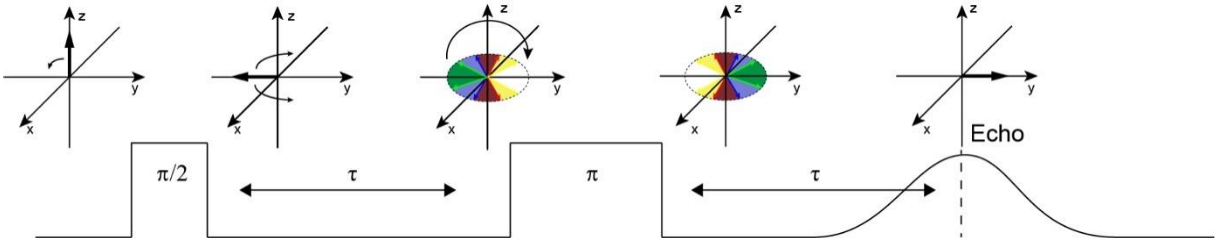

Figure 10: *Hahn* echo pulse sequence with an indicated corresponding change of magnetization.

This pulse sequence is the fundamental sequence used in many different pulse measurements, such as Davies electron nuclear double resonance experiments.

3.5. Relaxation times and their measurements

Relaxation principles and theories are one of the most complex mathematical constructs in magnetic resonance, and large computational power is required to describe even small systems sufficiently. Therefore, this thesis uses a phenomenological approach to describe relaxation effects in magnetic resonance.

Two relaxation effects are observed after the application of an mw pulse, working towards restoring the thermal equilibrium. *Longitudinal* (spin-lattice) relaxation, characterized by the time constant T_1, is the effect of the spins dispersing their energy towards their surroundings, the lattice, and thus restoring the thermal equilibrium, i.e. returning the magnetization towards the z-axis of the rotating frame. *Transversal* (spin-spin) relaxation, characterized by the time constant T_2, describes the decay of the transverse magnetization component due to spin-exchange mechanisms, for example, spin flip-flops,[155] in the x,y-plane (Figure 10). In general, T_2 is much shorter than T_1, and in real systems, the *phase memory time* T_m is recorded instead of T_2. The phase memory time includes additional effects of a real sample, like diffusion effects and contributions from the *longitudinal relaxation*.

T_1 is measured using the inversion recovery pulse sequence, by inversion of the overall magnetization with a π pulse and increasing the time delay T before a Hahn echo sequence, the recovery from full inversion can be detected. Alternatively, the saturation recovery pulse sequence can be applied. For the determination of T_2 or actually T_m the *Hahn echo* sequence is used by varying τ.[144]

In experiments targeting dipolar couplings, T_m plays a crucial role as long pulse sequences or evolution time is needed to observe dipolar couplings. Effects influencing the T_m time are the local spin concentration, with higher concentration shortening T_m, and magnetic moments of nuclei, with lager moments shortening the T_m time.

Therefore, in dipolar spectroscopy, samples are often deuterated to lengthen T_m, by reducing the magnetic moment and, with that, the nuclear spin diffusion.[156]

3.6. Electron Nuclear Double Resonance Experiments

One EPR method to gain detailed information on the hyperfine interaction and types of nuclei in the vicinity of the electron is Electron Nuclear DOuble Resonance (ENDOR). Typically, only electron spin transitions are generated in EPR spectroscopy via microwaves. ENDOR, however, is a double-frequency experiment with a combination of mw and radio frequency (RF) irradiation. The additional RF pulse is used to drive a nuclear spin transition of magnetic nuclei ($I \neq 0$). The EPR transition rule remains $\Delta m_s = \pm 1$ and $\Delta m_I = 0$, while the NMR transition induced by the RF pulse follows the $\Delta m_s = 0$ and $\Delta m_I = \pm 1$ rule. In ENDOR experiments, the RF pulse frequency is swept, and the spectrum is recorded as a function of the frequency.

The detected signal at the end of an ENDOR experiment is the difference between the EPR intensities depending on whether a nuclei transition is driven or not. Thus, the x-axis of the plotted spectrum displays the swept RF. One signal line is obtained when the irradiated RF resonates with the E_1 to E_2 transition. Another signal is obtained when there is a resonance between the RF and the E_4 to E_3 transition (Figure 9 and Figure 12).

The influence of the strength of the hyperfine interaction should not be overlooked. The expected peak position ($w_\pm$) is directly dependent on the nuclear *Larmor* frequency w_I:

$$w_\pm = \left| w_I \pm \frac{A}{2} \right|, \tag{2.18}$$

the peaks get centered around w_I for $w_I > \frac{A}{2}$ (weak coupling case) split by A. In the case of $w_I < \frac{A}{2}$ (strong coupling case) the peaks are centered around $\frac{A}{2}$ and split by $2w_I$.

This centering of the spectrum can be used to isolate different nuclei. At Q-Band (34 GHz), the proton *Larmor* frequency is around 51 MHz, and the one of deuterium is 8 MHz. Choosing the optimal frequency band can simplify the spectrum significantly, and couplings of different isotopes can be identified. As a result, ENDOR spectra often appear less complicated than ESE spectra (if hf is resolved in the ESE spectra). Each hyperfine coupling results in a line for each electron manifold.

For example, an $m_s = \pm½$ system with three coupled nuclei possessing different hyperfine couplings ($m_I = \pm½$) shows six lines around the *Larmor* frequency for an ENDOR spectrum but eight lines for the ESE spectrum. Nuclei with the same hyperfine coupling only result in a one-line set in ENDOR. The number of lines for *N* nuclei ($m_I = \pm½$), therefore, can be calculated as 2*N* instead of 2^N in an ESE spectrum.

Two typical ENDOR applications exist *Mims*- and *Davies*-ENDOR.[157,158] *Davies* is used for larger hyperfine couplings due to the disadvantage of a "blind spot" at the *Larmor* frequency resulting from the excitation bandwidth of the first inversion pulse (Figure 11). *Mims*-ENDOR uses a stimulated echo sequence mainly for small hyperfine couplings (Figure 13). However, it has the disadvantage of periodic "blind spots" due to the pulse sequence.

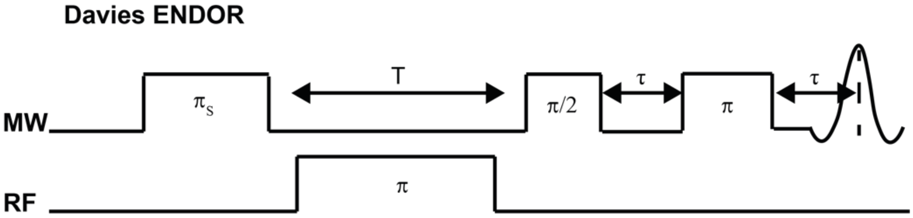

Figure 11: *Davies* ENDOR pulse sequence.

While performing an ENDOR experiment, the magnetic field remains constant at the position where the EPR resonance condition is fulfilled, and the radio frequency is swept. The first MW pulse shown in the Davies pulse sequence (Figure 11) is a selective inversion pulse with reduced power (also called soft pulse) to induce only one of the allowed EPR transitions (Figure 12, middle). The length of the inversion pulse can be adjusted depending on the investigated hf coupling. More prolonged inversion pulses resolve smaller couplings better; if large couplings are investigated, pulses of similar length to the *Hahn* echo sequence can be used. Afterward, the radio frequency is swept, followed by a *Hahn* echo sequence for detection (Figure 11). The *Hahn* echo sequence, in this case, consists of hard pulses, meaning higher microwave power and shorter pulse length, to detect all allowed transitions. The partial inversion of the echo is a result of the first inversion mw pulse. *Davies*-ENDOR is sometimes called the "hole burning" experiment because of the selective excitation of the first pulse, which burns a narrow hole in the electron spin population.

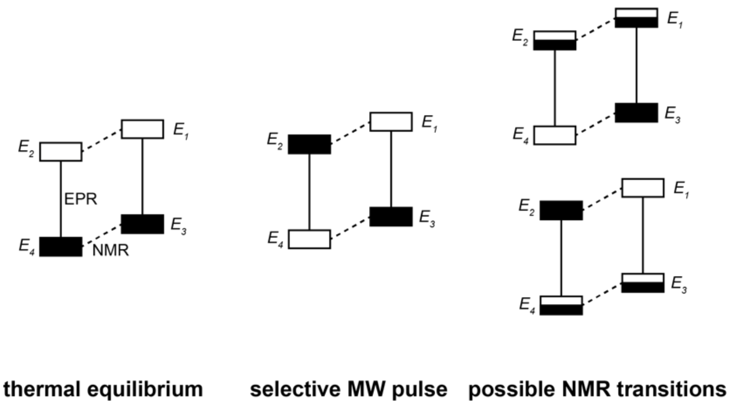

Figure 12: Principle of ENDOR spectroscopy for *I* = ½ and *S* = ½. Population changes after pulses from **Figure 11**. Full lines are EPR transitions, and dashed lines are NMR transitions. Full boxes mark the higher population. At thermal equilibrium (left), the lower energy levels are higher populated following the Boltzmann equation. The selective MW pulse excites only one specific EPR transition (middle), here the E_4 to E_2 transition. Sweeping the RF frequency can excite a possible NMR transitions (right). Depending on the RF frequency, either one gets excited, restoring the population difference partly.

For basic pulse experiments, the *Boltzmann* distribution is the central aspect. In the beginning, the lower energy levels (E_3 and E_4 of Figure 12*)* are populated with more spins than the upper energy levels. The first selective π-pulse saturates the EPR transition from E_4 to E_2. As a result, the EPR signal detected via *Hahn* echo decreases. With the RF pulse, the two possible NMR transitions are excited. Thus, if an NMR transition is hit, the population difference in the energy states is partly restored (Figure 12, right), resulting in a higher EPR signal than off-resonance.

Furthermore, changing the magnetic field results in an orientation-dependent ENDOR experiment. The same principle differentiates two paramagnetic species in the same sample. During such an experiment, the magnetic field is moved to the position of a specific *g*-value or the resonance field of the second species. A distinct distance between the *g*-values of the examined species is necessary for an orientation-selective ENDOR measurement. Thereby, higher frequencies can be advantageous, A is not field-dependent, and the resolution is not increased. Still, the g-factor resolution can be improved, making orientation-selective measurements feasible. These measurements allow the extraction of multiple information from A, like the length and angle (in regards to a chosen axis) of the vector between the electron and nuclei. A further advantage of higher frequencies is that less sample amount is needed for the measurement compared to lower frequencies. In general, ENDOR has a higher resolution but a lower sensitivity than standard ESE measurements, meaning a higher spin density inside the sample is needed for the measurement.

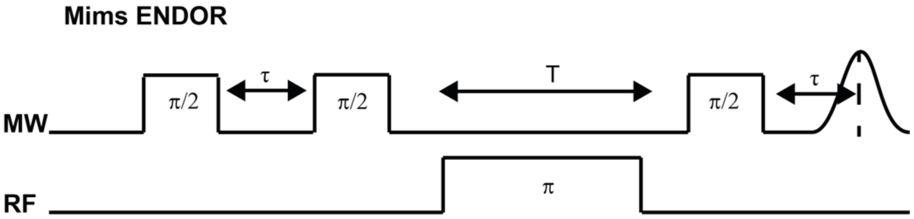

Figure 13: *Mims* ENDOR pulse sequence.

The second major ENDOR technique, *Mims*, is based on the stimulated echo technique with two preparation $\frac{\pi}{2}$ pulses and one $\frac{\pi}{2}$ detection pulse with the RF pulse in between (Figure 13). Compared to *Davies,* the two preparation pulses are not selective and excite the whole spin envelope. One disadvantage is the periodic zero-intensity transitions, called "blind spots". These blind spots result from the stimulated echo sequence and can be fine-tuned by considering both the *phase memory time* and the expected coupling value. As the *Mims intensity* I is dependent on the *phase memory time:*

$$I = I_0 e^{-\left(\frac{2\tau}{T_m}\right)^c}, \tag{2.19}$$

with c the *stretching factor* extracted from the T_m measurements and τ the *inter pulse delay* of the preparation pulses in the *Mims* sequence (Figure 13). The *ENDOR efficiency* F can be calculated from the hypothetic coupling value and τ:

$$F = 0.5\ (2\pi \frac{A}{2} \tau), \tag{2.20}$$

which generates zero efficiency ($F = 0$) for all ($A\ = \frac{n}{\tau}$ with $n = 0,1,2,3, \ldots$). The product of the two values yields the *ENDOR sensitivity* S:

$$S = F \cdot I = 0.5\ (2\pi \frac{A}{2} \tau) I_0 e^{-\left(\frac{2\tau}{T_m}\right)^c}. \tag{2.21}$$

In general, longer τ can shorten the space between blind spots; at the same time, very small coupling values can be investigated by prolonging τ extensively.[9,19] As these blind spots significantly distort the resulting ENDOR spectrum, the entire coupling tensor is often unresolved. This is often compensated by measuring *Mims* spectra with different τ values and adding them to a full spectrum in post-processing.

4. ^{19}F ENDOR investigation of metal-incorporated G-Quadruplexes

The incorporation of transition metals introduces additional functionality to the GQs. In a first attempt, pyridine or imidazole on artificial ligands attached to the 5'-end of short guanine-rich sequences were synthesized. These sequences formed tetramolecular GQs, generating coordination environments for metal cations like Cu^{2+} and K^+ (Figure 14A).

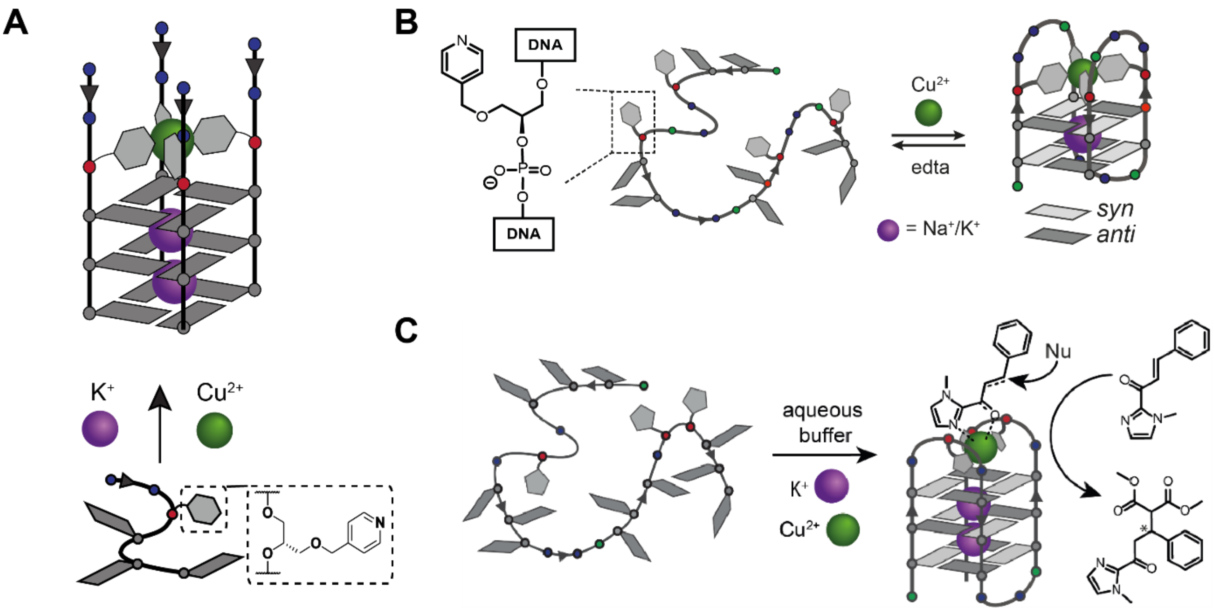

Figure 14: Different GQ systems developed by the Clever group for EPR applications. **A**: Tetramolecular GQ with pyridine linker for Cu^{2+} coordination (adapted from Ref.[27]). **B**: Unimolecular GQ with pyridine-incorporated artificial nucleotides replacing one G quartet (adapted from Ref.[18]). **C**: Unimolecular GQ with pyridine-incorporated artificial nucleotides incorporated into the loop with open coordination for Micheal-addition educt (adapted from Ref.[159]).

In this thesis, Cu^{2+} ions incorporated in these GQ are especially interesting as they are EPR active (Figure 14A).[160–162] Here, the main focus lies on unimolecular GQs, with the detection of the Cu^{2+} position and their possible applications in research. To modify unimolecular GQs, artificial nucleotides with pyridine or imidazole functions attached to a glycol backbone were used (Figure 14B),[163,164] replacing one G-quartet in the GQ with a ligand quartet. These metal-incorporated unimolecular GQs have a wide variety of topologies and possible applications. By choosing the correct position, topology switches were achieved upon metal ion binding. One exciting application is using Cu^{2+}-modified unimolecular GQs as catalysts for the Michael addition reaction in water (Figure 14C).[159] These catalysts were shown to have very high conversion rates and enantioselectivities of up to $\geq 99\%$. In the long term, this could be a valuable step towards a greener chemistry, away from the use of organic solvents towards the use of water and less energy.

When three ligands are introduced into the loop region, one metal coordination site is unoccupied, enabling substance binding during catalysis. The location of the ligands in the loop can tune the enantioselectivity. If this technique could be applied to more reaction types and better understood how the ligand position influences the enantioselectivity, this would be a large step toward greener chemistry.

Accessing information on the Cu^{2+} position inside an unimolecular GQ is troublesome by most methods. ^{19}F ENDOR allows examining the Cu^{2+} in detail with minimal structural interference. The Cu^{2+} incorporated GQs are labeled with ^{19}F isotopes at single positions in the GQ, replacing a ^{1}H, to determine the distance and angle between the Cu^{2+} and ^{19}F. This information allows for structural conclusions about the Cu^{2+} surroundings and the GQ's overall structure, as this information was inaccessible before.

Detecting Cu^{2+}-^{19}F distances relies on dipolar spectroscopy between the paramagnetic center Cu^{2+} and the nuclear magnetic spin of ^{19}F. The use of ^{19}F as a magnetic spin probe has the advantage, especially in biological applications, that these systems naturally do not include ^{19}F. Artificially labeling positions with ^{19}F, replacing ^{1}H, leads only to minor structural changes due to its inert nature and similar volume and size compared to other spin labels. Here, the application of this technique is optimized on a 34 GHz spectrometer. Previously, most applications were only performed at 94 GHz due to the large enough separation of ^{19}F and ^{1}H.[9,16,151] At 34 GHz, the hyperfine signals overlap strongly, as only 3 MHz separates the nuclear *Larmor* frequencies.

In the following, Cu-F ENDOR distance measurements are used to resolve the positioning of the Cu^{2+} ion in the overall GQ structure and show the feasibility of these studies at 34 GHz. Further, the application advantages and disadvantages of ^{19}F ENDOR at 34 GHz compared to 94 GHz are investigated, and the limits of this technique at 34 GHz are analyzed. These results provide an approach to examining the application of GQs as catalysts and possible binder interactions, as shown in later chapters.

4.1. Initial Characterizing Cu^{2+} in unimolecular GQ

*Parts of the following chapters are published in S. L. Schumann, S. Kotnig, Y. Kutin, M. Drosou, L. M. Stratmann, Y. Streltsova, A. Schnegg, D. A. Pantazis, G. H. Clever, M. Kasanmascheff, Chem, **2023**, 29, e202302527.*[18]

Naturally, the unimolecular GQ investigated in this thesis is not EPR active. Artificially incorporating Cu^{2+} allows for EPR measurement with $S = 1/2$. For the incorporation, the top G quartet is replaced by pyridine incorporated in unnatural nucleotides (Figure 15A). Additionally, one guanosine is replaced with 2′-fluoro-2′-deoxyguanosine to introduce ^{19}F into the system (Figure 15B). For a full analysis of the Cu^{2+} environment, subsequently, all four guanosines of the second G quartet are labeled (**GQ1** – **GQ4**). A sample without ^{19}F modifications was prepared as a background to check if any structural changes were observable (**GQ0**). CD-measurement analysis revealed that **GQ1** – **GQ4** adopted the same overall structure as **GQ0** without ^{19}F tags.[18] These initial checks were performed on 0.5 mM samples with 5 v/v% glycerol content. **GQ0**'s ESE spectrum has axial symmetry (Figure 16A), with clearly defined Cu hyperfine coupling in the g parallel ($g_{\|}$) region. It shows an identical line shape to tetramolecular GQ with Cu^{2+} incorporation.[27] For all samples measured in this thesis, a small manganese signal of resonator background or buffer impurities is visible between 1200 mT and 1230 mT.

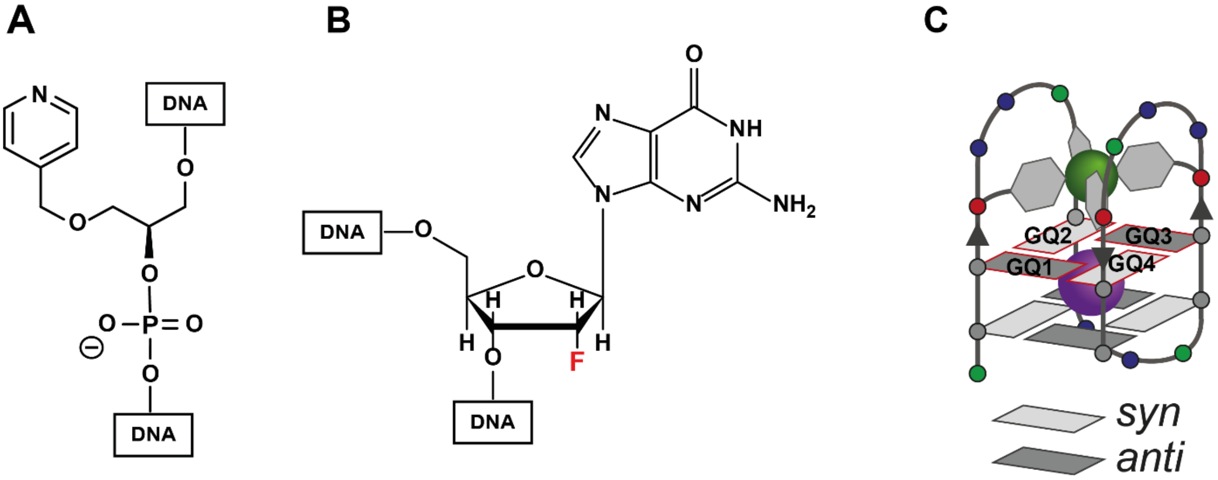

Figure 15: Modified unimolecular GQ with pyridine unnatural nucleobases (**A**) and 2′-fluoro-2′-deoxyguanosine (**B**). **C**: Schematic structure of the folded GQ modified with four pyridine-ligands (**GQ0**). One ^{19}F-containing guanosine was incorporated at one of the highlighted G positions in **GQ1**-**GQ4**. Bound Cu(II) and K(I) cations are represented as a green and purple sphere, respectively.

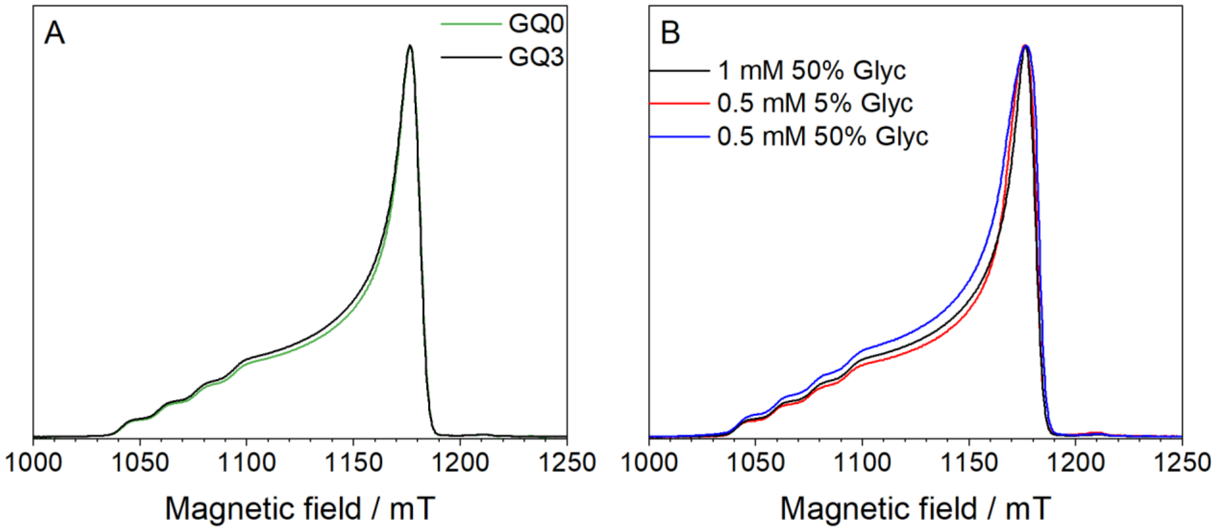

Figure 16: **A**: Comparison of **GQ0** (green) and **GQ3** (black) ESE spectra at 15 K and 34 GHz. Spectra are normalized to the maximum intensity. **B**: Comparison of **GQ3** ESE spectra for different concentrations of GQ and glycerol content. All spectra are recorded at 15 K and 34 GHz and normalized to the maximum intensity.

No further investigations of the origin were performed as the signals lie outside the Cu^{2+} EPR envelope. Direct comparison of **GQ0** and **GQ3**, as a ^{19}F harboring sample, show no differences in ESE line shape. The influence of ^{19}F on the overall structure can be excluded, while minor changes are still possible and are investigated with ENDOR later. Additionally, comparisons of glycerol content and GQ concentration were performed to optimize sample preparation. An increase from 5 %v/v to 50%v/v glycerol content showed no EPR intensity or line shape change (Figure 16B). Further, the concentration was increased from 0.5 mM to 1 mM to shorten ENDOR measurement time. Figure 16B showed no aggregation or dimerization effects on the ESE spectrum of 1 mM **GQ3** compared to 0.5 mM, while slight differences in the intensity are due to differences in the power optimization (Figure 16B). The Cu^{2+} spectrum is broad compared to organic radicals, with a spectral width of roughly 150 mT. One effect of this wide spectrum is that the spin packages have different properties, resulting in slightly different optimal measurement parameters. This effect results in optimal power differences of around 2 dB between $g_\perp$ and $g_\parallel$. Small differences in the MW power, therefore ,result in fluctuations of the intensity ratios between $g_\perp$ and $g_\parallel$ (Figure 16B).

The incorporation of ^{19}F resulted in the same overall line shape for all GQ samples. During the melting curve experiments of **GQ2** and **GQ4**, a destabilizing effect was discovered when ^{19}F was incorporated into syn-conformation guanosines, lowering the melting temperature of these GQs by up to 21 °C.[18]

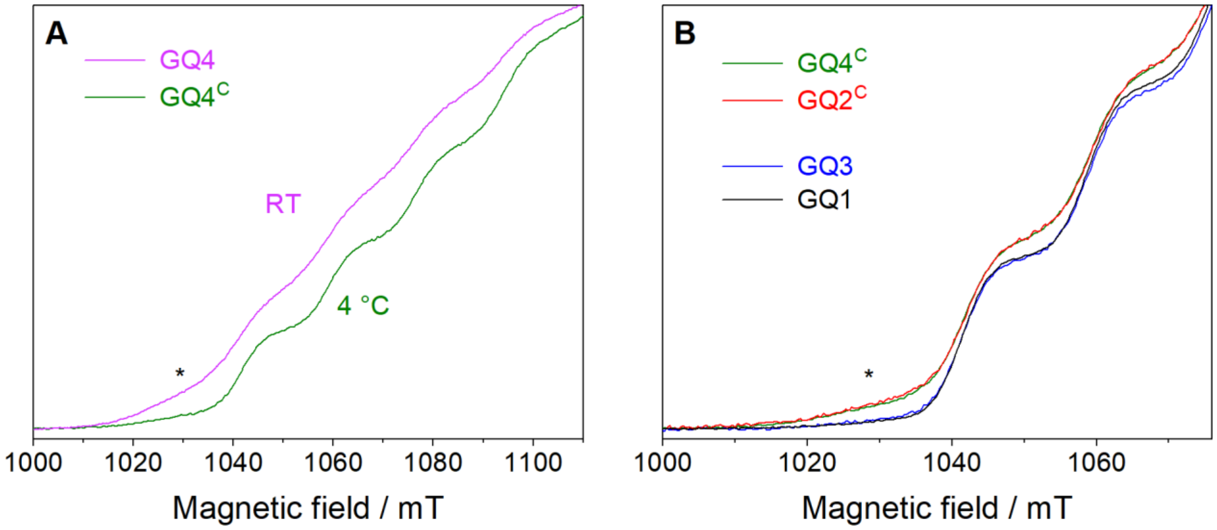

Figure 17: A: ESE spectra of **GQ4^C** (green) and **GQ4** (at room temperature, RT, pink) zoomed into the $g_{\parallel}$ region. **B**: ESE spectra of **GQ1**, **GQ2^C**, **GQ3**, and **GQ4^C** (colors are indicated in the graph). Intensities were normalized to the first (low-field) hyperfine feature of the Cu^{2+} spin-label. As discussed in our previous work, the asterisk (*) indicates the spectral feature of free or non-specifically bound Cu^{2+}.[27]

The destabilization effect originates from electrostatic repulsion between the phosphate and fluorine, which has been reported before in the literature.[165–167]

The ESE spectra of **GQ2** and **GQ4** showed broad unresolved features in the $g_{\parallel}$ region (Figure 17A asterisks), which are attributed to free or unspecifically bound Cu^{2+}, as discussed by Stratmann et al.[27] While **GQ0**, **GQ1**, and **GQ3** can be prepared at room temperature, with nearly no free Cu^{2+} in the spectra (Figure 17B), **GQ2** and **GQ4** showed to be partly denatured when prepared at room temperature. Lowering the sample preparation temperature to 4 °C stabilized the GQ, **GQ2^C** and **GQ4^C** (index C for cold room preparation at 4 °C), showing only a minor amount of free or unspecifically bound Cu^{2+} (Figure 17A). Additionally, the hyperfine structure of **GQ2** and **GQ4** is broadened significantly, and even with preparation at 4 °C, the broadening compared to **GQ1** and **GQ3** partly remains. As the samples are all directly flash-frozen after preparation, the hyperfine broadening, as well as an observed slight general EPR line broadening, are ascribed to greater conformational freedom of these GQs compared to **GQ1** and **GQ3** (Figure 17B). Surprisingly, compared to **GQ0**, the none ^{19}F labeled GQ, the melting temperatures of **GQ1** and **GQ3** are higher, indicating increased stability. ^{19}F incorporation into the anti-configured guanosines stabilizes the GQ, possibly due to the electron-pulling effect of the fluorine.

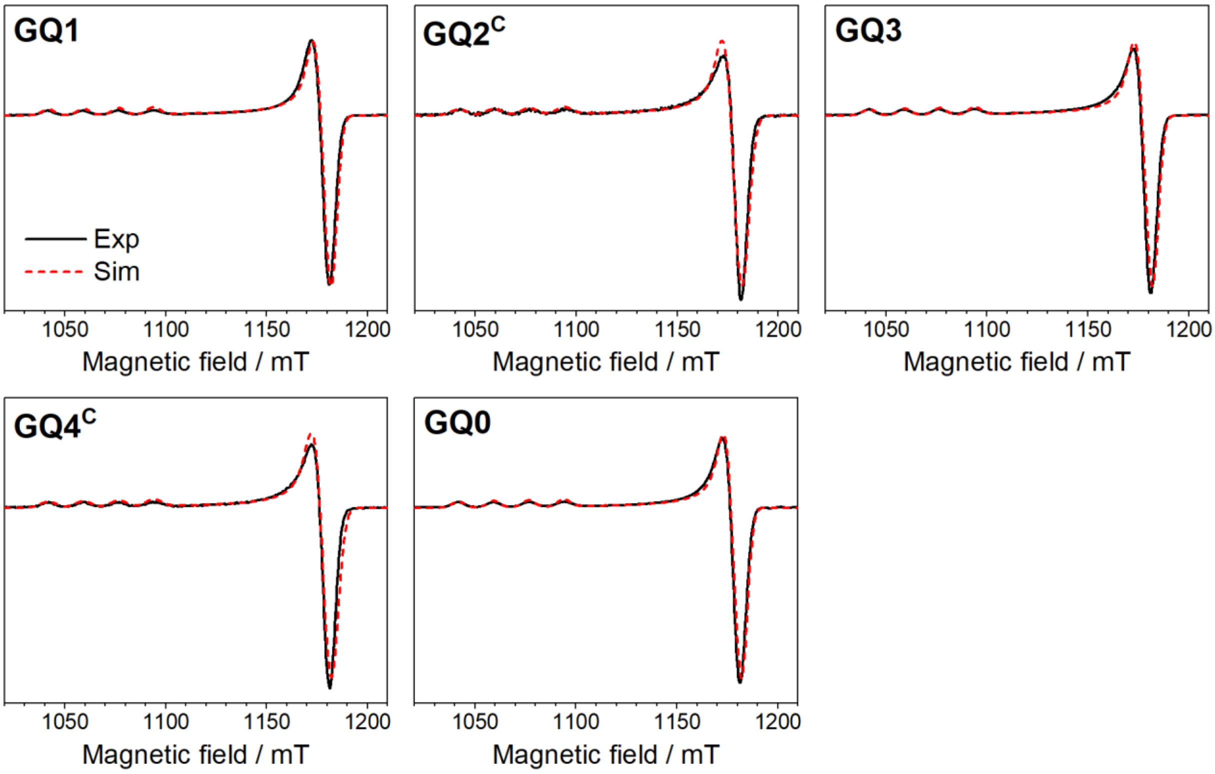

Figure 18: First-derivative ESE spectra of **GQ0** – **GQ4** recorded at 34 GHz (black traces) with simulations (red dashed traces). The simulation parameters are $g_{\perp}$ = 2.061, $g_{\parallel}$ = 2.275, $A_{\parallel}$ = 555 MHz for **GQ0** – **GQ5**. The first-derivative spectra were obtained with a modulation amplitude of 4 mT by pseudo field modulation.[168]

Simulations of the pseudo-modulated ESE spectra support the analysis of CD spectra of an overall identical structure (Figure 18). All samples are simulated with the identical parameter set shown in Table 1, with the major difference being the added line broadening for **GQ2^{C}** and **GQ4^{C}** (Figure 18). All spectra show a square planar coordinated Cu^{2+} spectrum represented by a strong axial shape with hyperfine coupling only resolved at the $g_{\parallel}$ due to the line width exceeding the coupling value in the $g_{\perp}$ region,[169,170] as previously reported for these systems.[27,160,171] For simulation purposes, a value of $A_{\perp} = 50$ MHz is used. Overall, the ^{19}F labeling has a negligible effect on the electronic structure of Cu^{2+}, as no visible changes are seen in the ESE spectra.

Table 1: Simulation parameters for **GQ0** – **GQ4^{C}**. g values and hyperfine constants for Cu^{2+} are identical for all five samples with the only variation being the line broadening introduced via H-Strain. H-Strain introduces line broadening due to added uncertainty of g and unresolved hyperfine coupling or other transition-independent effects.

	GQ0	**GQ1**	**GQ2^{C}**	**GQ3**	**GQ4^{C}**
g value	[2.061 2.275]				
A_{Cu} / MHz	[50 555]				
H-Strain / MHz	[200 240]		[240 300]	[200 240]	[240 300]

4.1.1. Optimization of ^{19}F ENDOR measurements at 34 GHz

The relatively broad EPR spectrum of Cu^{2+} requires both Davies and Mims ENDOR measurements to record orientation-selectively and gain the full hyperfine tensor (Figure S1). For a clearer visualization, the ESE spectrum of **GQ3** is used from here on for further demonstrative purposes with the chosen field positions marked in Figure 19.

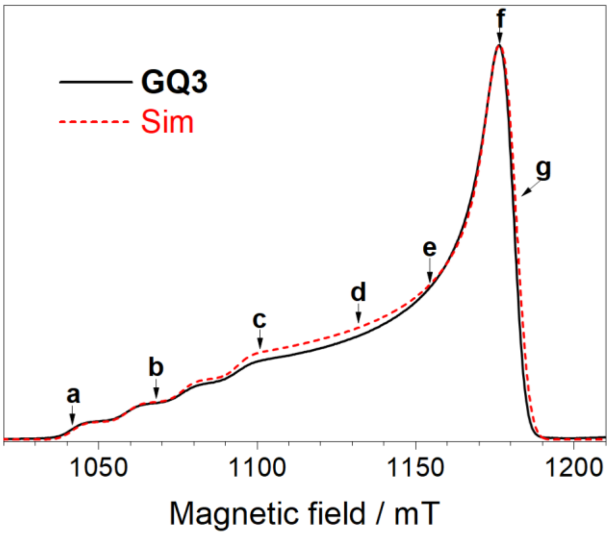

Figure 19: A representative echo-detected EPR spectrum for **GQ3** recorded at 34 GHz (black solid trace) with the corresponding simulation (red dashed trace). Simulation parameters are listed in Table 1. Field positions where ENDOR spectra were measured are marked a to g.

Previous molecular dynamic (MD) simulations for **GQ0** indicated that the expected distances to the respective hydrogen atoms, replaced by ^{19}F in **GQ1** – **GQ4**, are in the 1 nm range.[163] Application of Equation 2.15 allows the conversion of this distance to an expected coupling of approximately 0.1 MHz. As Mims ENDOR measurements are highly sensitive to couplings smaller than 3 MHz,[158] it is employed for this project. Due to the antiparallel folding of the GQ, the guanosines have different orientations depending on whether the strand is going up or down and, thereby, the ^{19}F tags. In **GQ1**/**GQ3**, the ^{19}F tag points upwards toward the Cu^{2+}, while the ^{19}F tag faces away (downwards) from Cu^{2+} in **GQ2**/**GQ4** (Figure 20). When applying ENDOR at 34 GHz, the separation of nuclear Larmor frequencies of ^{19}F and ^{1}H is only about 3 MHz, making the spectral analysis complicated due to the strong overlap of spectral features. To gain a clean ^{19}F Mims ENDOR spectrum, it is necessary to subtract a proton background (**GQ0**).

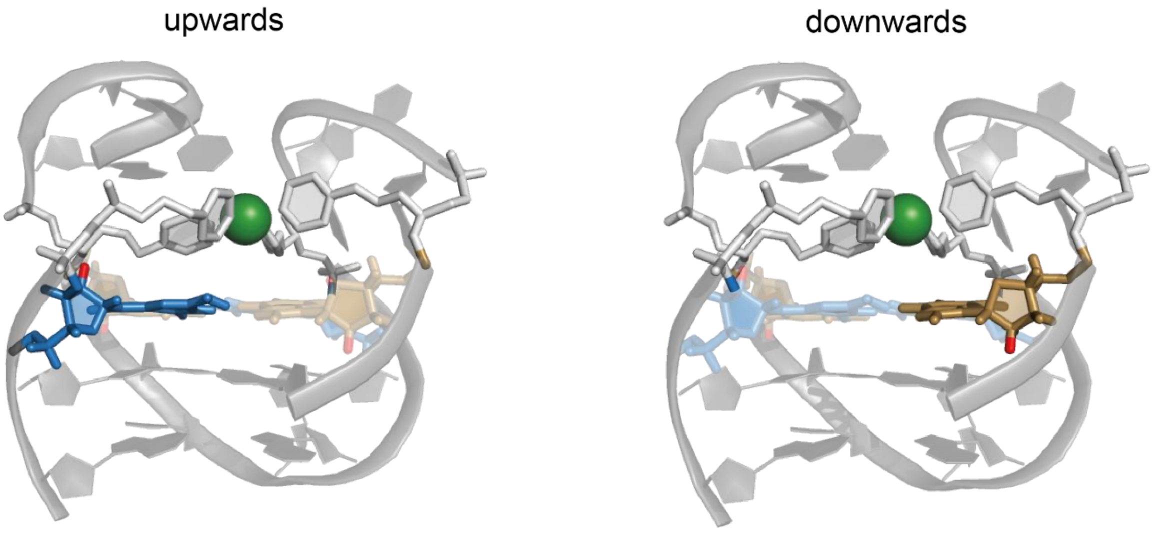

Figure 20: The upwards and downwards-facing guanosines in blue and golden sticks, respectively. The incorporated ^{19}F is shown in red.

Further, the correct optimization of the Mims sequence plays an essential role. If the τ value is too short, small hyperfine couplings can get suppressed due to a lack of sensitivity (Eq. 2.20). While the features might not be fully suppressed, the sensitivity is not sufficient to optimize the ^{19}F coupling. The first measurements were performed with a τ value of 300 ns, chosen to have a Mims blind spot frequency of 1 MHz with the anticipation that the expected smaller ^{19}F couplings are clearly and fully resolved between blind spots without the need for the otherwise often necessary τ depended multiple Mims measurements. Figure 21A shows a Mims ENDOR of **GQ3** at position **f** with $\tau = 300$ ns, which is already background corrected/subtracted and should show a clean ^{19}F spectrum. A clean spectrum could not be achieved as the large blindspot separation and a known field-dependent field shift of the 34 GHz Bruker standalone spectrometer made it very complicated to match the primary spectrum and background. To avoid these problems for the background correction from thereon onwards, the field positions were calculated instead of read out from the spectrometer software. In general, XEPR (Brukers EPR spectrometer software) shows the *g* value by hovering the mouse over the EPR line; while this gives good values for a good background match, a near-identical spin package must be probed at best. To guarantee this, the exact *g* values of the main ^{19}F measurement field position were written down and used to calculate the background field position with the given spectrometer frequency. Although this procedure resulted in significantly improved background fits, some minor manual adjustments were required during post-processing. Overall, the EPR spectrometer has certain technical limitations, as neither the field nor frequency sensor is entirely precise. Consequently, small deviations in one or both of these sensors are to be expected. The background spectra are always hand-fitted to the primary spectrum by adjusting the field position; shifting the spectrum in the x-axis. Further, due to a different number of scans or sensitivity differences, their intensities were matched by multiplying a constant by the background spectrums y-axis. This procedure resulted in a cleaner ^{19}F spectrum (Figure 21B) but did not help improve the sensitivity. Application of Eq. 2.21 helped to improve ^{19}F sensitivity from roughly 2% to nearly 20% by adjusting τ to 2000 ns. While improving sensitivity, the prolonged pulse sequence led to more relaxed spins, leading to noisier spectra for identical scan numbers (Figure 21B vs. A). Additionally, the used 17 µs RF pulses are optimized for ^{1}H ENDOR. In general, this is not problematic as ^{19}F and ^{1}H are very similar in RF terms (optimal RF length for ^{19}F 19 µs); this said ENDOR resolution scales with the inverse of the RF pulse length, meaning longer RF pulse lengths increase the resolution of small hyperfine couplings (Figure 21C). For the correct optimization of τ, the phase memory time T_m must be determined correctly. If the interpulse delay T of the stimulated echo sequence is increased, the resulting T_m changes as well. Optimizing the RF pulse length, therefore, included re-optimization of τ (Figure 21E). The longest RF pulse length achieved, without risking burning the ENDOR coils of the standard D2 Bruker resonator with our 600 W amplifier, was 45 µs; additional longer pulse lengths could not clearly be distinguished in RF nutation experiments as no complete oscillation was visible. A 1000 ns delay before and after the RF pulse was included, bringing the inter-spin delay to $T = 47$ µs. While initially chosen for the hoped effect of diminishing proton background effects, the use of deuterated water and glycerol was shown to be much more important for the prolonging of relaxation times than for the proton background (Figure S2). The effect of deuteration of the buffer has a neglectable effect on the ^{1}H ENDOR line shapes in the ^{19}F Larmor frequency range. Davies ENDOR measurements show that coupling from these exchangeable protons lies outside of the ^{19}F Mims measuring range and is not attributed to the reduction of background intensity. In contrast, Mims measurements are unfeasible due to the very short phase memory time together with spin diffusion in H_2O (Figure S3). Meanwhile, the phase memory times nearly tripled, significantly improving SNR and sensitivity due to longer possible τ values (Figure S2). Similar to the varying optimal power throughout the EPR envelope of Cu^{2+}, T_m is influenced as well, resulting in orientation-dependent T_m values (Figure 21E).

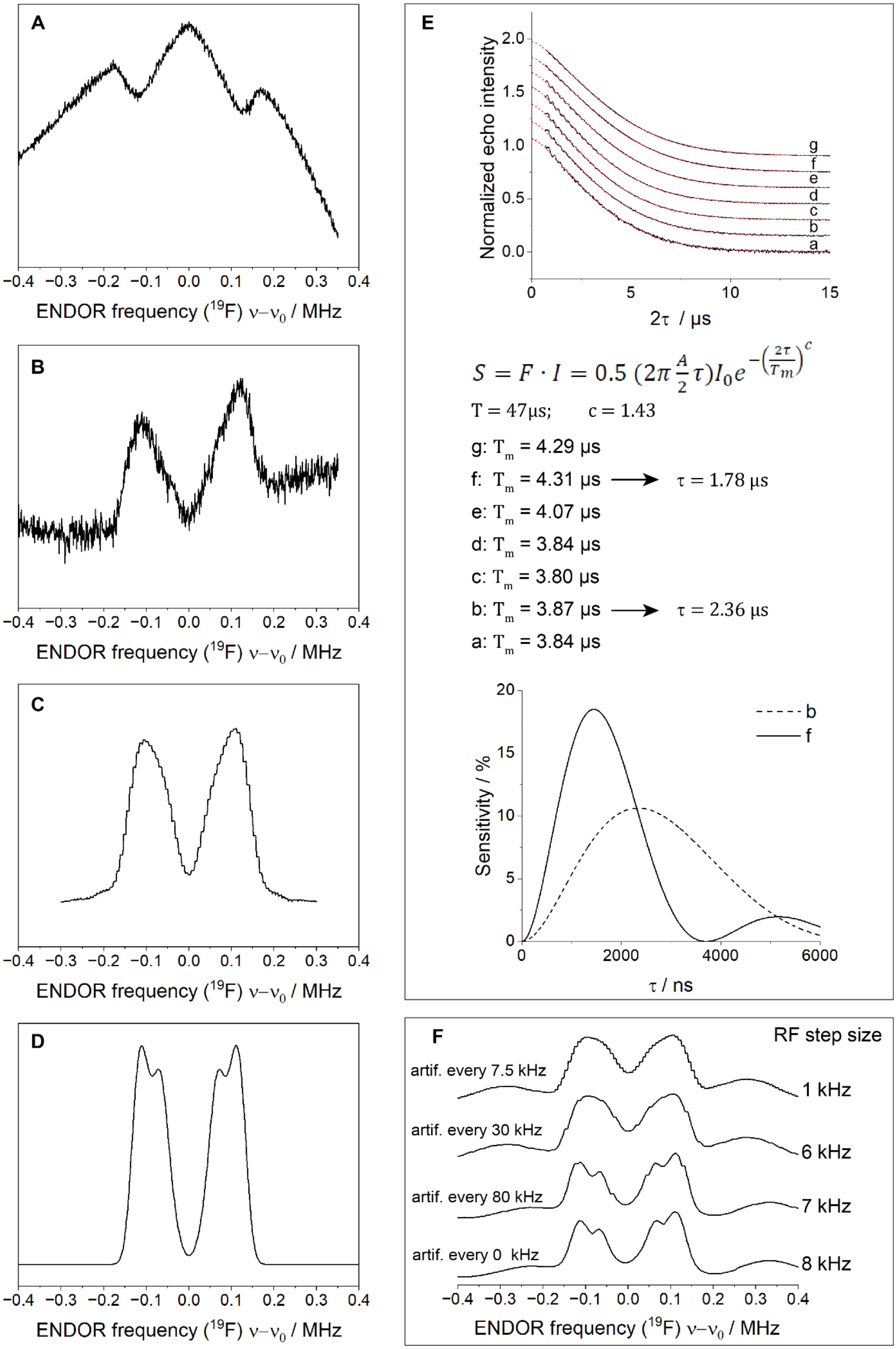

$$S = F \cdot I = 0.5\,(2\pi \frac{A}{2}\tau) I_0 e^{-\left(\frac{2\tau}{T_m}\right)^c}$$

T = 47µs; c = 1.43

g: T_m = 4.29 µs

f: T_m = 4.31 µs ⟶ τ = 1.78 µs

e: T_m = 4.07 µs

d: T_m = 3.84 µs

c: T_m = 3.80 µs

b: T_m = 3.87 µs ⟶ τ = 2.36 µs

a: T_m = 3.84 µs

Figure 21: Mims optimization procedure for 34 GHz ^{19}F Mims ENDOR measurements at the example of **GQ3** position **f** from Figure 19. **A**: 1 GHz sweep width ^{19}F Mims ENDOR spectrum with τ = 300 ns and an Rf pulse length of 17 µs. **GQ0** Background measurement was done identically and subtracted to gain a clean ^{19}F spectrum. **B**: 1 GHz sweep width ^{19}F Mims ENDOR spectrum with optimized τ = 2000 ns and an Rf pulse length of 17 µs. **GQ0** Background measurement was done identically and subtracted to gain a clean ^{19}F spectrum. **C**: 1 GHz sweep width ^{19}F Mims ENDOR spectrum with τ = 2000 ns and an optimized Rf pulse length of 47 µs. **GQ0** Background measurement was done identically and subtracted to gain a clean ^{19}F spectrum. **D:** 1 GHz sweep width ^{19}F Mims ENDOR spectrum with τ = 2000 ns and an optimized Rf pulse length of 47 µs and an adjusted RF step size of 8 kHz. **GQ0** Background measurement was done identically and subtracted to gain a clean ^{19}F spectrum. **A – C** RF stepsize is 1 kHz, and the early ending of the sweep results from shifting the main measurement and background onto each other; wider spectra were recorded later to avoid cuts in the shown MHz range. **E**: Optimization procedure for τ. Top: T_m measurements using the simulated echo sequence (T = 47 µs) of **GQ3** (black) at all field positions indicated in Figure 19 fitted with a stretched exponential decay function (Eq. 2.19, red) the resulting T_m times are listed below the graph (c = 1.43). Bottom: An illustrative graphical determination of optimal τ values for field positions **b** and **f** of **GQ3** through the employment of Eq. 2.21 (also shown in the figure). The resulting optimal τ values are written behind their representative T_m value. Estimated hyperfine values A for application of Eq. 2.21 were determined from short 200 scan Mims measurements with τ = 2000 ns (not shown). **F**: RF step size optimization for **GQ3** position **f**. Rf steps between 1 – 7 kHz result in visible repeating artifacts (art.) in the spectrum.

While the variation is within 15% of the lowest value, each field position is optimized separately to get the best measurement parameters to minimize measurement time as much as possible (Table 2).

After these optimization steps, a major flaw of the EPR spectrometer could be seen clearly; while the software allows to change the RF step size in 1 kHz steps all the way down to 1 kHz, the spectrometer RF dice box itself could not provide such small steps. This resulted in resampling the same frequency multiple times until the subsequent achievable RF frequency, showing in the spectrum as “step-like” artifacts (Figure 21C, F). While Bruker is aware of this issue and offers a workaround for some spectrometers, our spectrometer is equipped with a DICE II box, including an Arm 9 CPU chipset, which still lags firmware updates to implement this workaround. Therefore tests for the best RF stepsize were conducted, revealing the minimum stepsize without artifacts to be 8 kHz (Figure 21F).

Table 2: Chosen τ values (in µs) for each field position for samples **GQ1**–**GQ5**. The optimal values might vary slightly. If a similar sensitivity, <1% deviation of the maximum, could be achieved with shorter τ values, sensitivity was sacrificed for shorter overall measurement times, especially for positions **a**-**c**.

Position	GQ1	GQ2	GQ3	GQ4
a	2.00	2.50	2.00	2.65
b	2.00	2.50	2.00	2.50
c	2.00	2.50	2.00	2.50
d	2.00	2.10	2.00	2.10
e	1.90	2.50	1.90	2.50
f	1.62	3.00	1.78	3.00
g	1.62	2.50	1.75	2.50

This information was also shared with other research groups in the field, struggling with identical problems. A step size of 8 kHz compared to 1 kHz first seems to lower the spectral resolution. Still, no couplings this small are expected for GQ samples, and more importantly, the general line width of the sample is wider than 8 kHz, making resolving such couplings impossible.

Similar to the concentration test of the ESE spectra in the beginning, additional measurements were performed to investigate the concentration limits of ^{19}F ENDOR (Figure S7). Even concentrations as low as 10 µM could be measured without a problem, while optimization at this very low concentration is time-consuming and inaccurate. Optimization requires some test scans and visible ^{19}F coupling to input a rough hf coupling value into Eq. 2.21. At position **f** with high EPR intensity, this might be possible in 60 min or less, while positions **a** – **c** would already require 6 hours or more of test scans. In this regard, the shown measurements in Figure S7 demonstrate the high utility of this technique at even very low concentrations while simultaneously revealing the advantage of higher concentration: Time-saving. This thesis mostly used 1 mM concentration, and the measurements took 3 to 18 hours for positions **f** and **a**, respectively. The measurement time doubles as the background measurements of **GQ0** needed at least as long as the primary measurement to avoid reintroducing noise to the spectra through background subtraction.

All optimization steps together produce a very clean ^{19}F spectrum with high sensitivity and excellent SNR (Figure 21D). In the following, all ^{19}F Mims spectra are optimized with this procedure, and Figure S4 shows an example of the necessary background subtractions to gain clean ^{19}F spectra.

4.1.2. Determination of Cu^{2+} position in unimolecular GQs

^{19}F ENDOR distance measurements allow us to determine structural features by comparing different labeling positions. Labeling all four guanosine in the first quarter of the GQ, thereby, allows us to draw structural conclusions of the Cu^{2+} ion between them. Following the optimization procedure, clear ^{19}F spectra could be achieved for all positions and GQs, with very distinguishable orientation-dependent hyperfine patterns. Comparing the different labeling positions shows a clear separation into two conformational states (Figure 22). **GQ1/3** and **GQ2^{C}/4^{C}** being in the same anti/syn conformation, respectively, opposite each other with identical line shapes (Figure S6), leads to the conclusion that well-defined and fully symmetric GQs are formed with the Cu^{2+} ion located centrally above the lower quartets.

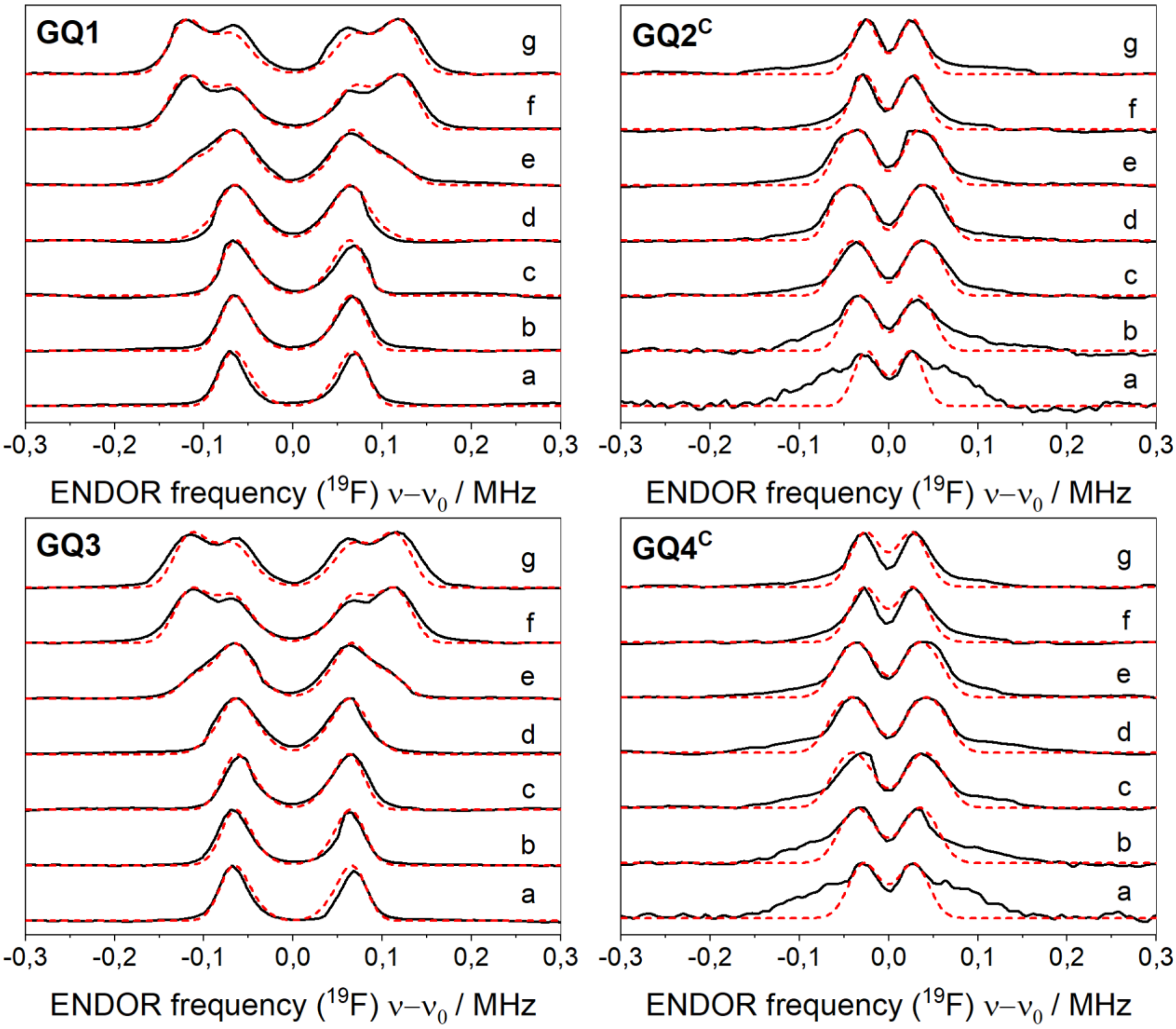

Figure 22: Background-subtracted orientation-selective ^{19}F Mims ENDOR spectra of **GQ1** - **GQ4** at the field positions marked in Figure 19 (black traces), with spectral simulations (red dashed traces, simulation parameters are listed in **Table 3**). Each spectrum was normalized to its maximum intensity; the traces were shifted vertically for clarity. The broad spectral features for **GQ2^{C}** and **GQ4^{C}** positions **a** and **b** originate from the denatured GQ fraction. A comparison with room temperature prepared **GQ2** and **GQ4** is shown in **Figure S5**.

A clear difference between GQ's up- and downwards-facing ^{19}F positions was expected. For example, the broadest ENDOR features of **GQ1**/**GQ3** and **GQ2^{C}**/**GQ4^{C}** are observed in the traces of position **g**, and **c** – **d**, respectively.

The differences between **GQ1**/**GQ3** and **GQ2^{C}**/**GQ4^{C}** can be rationalized based on the nuclear position coordinate β with respect to the Cu^{2+} g-tensor (Figure 23). This coordinate affects the angle θ between the static magnetic field (**B$_0$**) and the inter-spin vector excited at each observer field (**a** – **g**), which, in turn, determines the frequencies of ENDOR transitions.[172,173] As mentioned before, Equations 2.14 and 2.15 are a simplification and mostly only applicable to isotropic systems; the strong anisotropy in the Cu^{2+} system requires the consideration of additional parameters such as θ (Equation 3.1).

$$A = \frac{\mu_0 \mu_B \mu_N g_N g_e}{4\pi h}\frac{1}{d^3}(3cos^2\theta - 1) + A_{iso} \tag{3.1}$$

The perpendicular component of the dipolar tensor (for $\theta = 90°$) is usually the one that can be easily read off a spectrum for distance determination. However, a complication arises due to the g-anisotropy of the Cu^{2+}: it leads to the explicit dependence of ENDOR peak positions on the electron *g*-tensor.[172,173] Thus, for the ENDOR simulations, an explicit form of the *full* ^{19}F hyperfine tensor $\hat{A}$ expressed within the *g*-Frame is used:

$$A_{ij} = \frac{-\mu_0 \mu_B \mu_N g_N}{4\pi h}\frac{1}{d^3} g_i\left(3r_i r_j - \delta_{ij}\right) + A_{iso}\delta_{ij}, \tag{3.2}$$

where g_i are canonical values of the Cu^{2+} g-tensor, δ_{ij} is the Kronecker delta; $r_x = sin\,(\beta)$, $r_y = 0$, $r_z = cos\,(\beta)$, where β is the polar angle that the inter-spin vector forms with the g_z axis, i.e., β defines the angular position of the nucleus with respect to the Cu^{2+} g-tensor (Figure 23). Additionally, the expressions for r_i are simplified by the axial symmetry of the Cu^{2+} g-tensor, which eliminates the azimuthal angle.[173]

This very technical explanation can be simplified into a more visualized explanation of canonical g-tensor orientations.

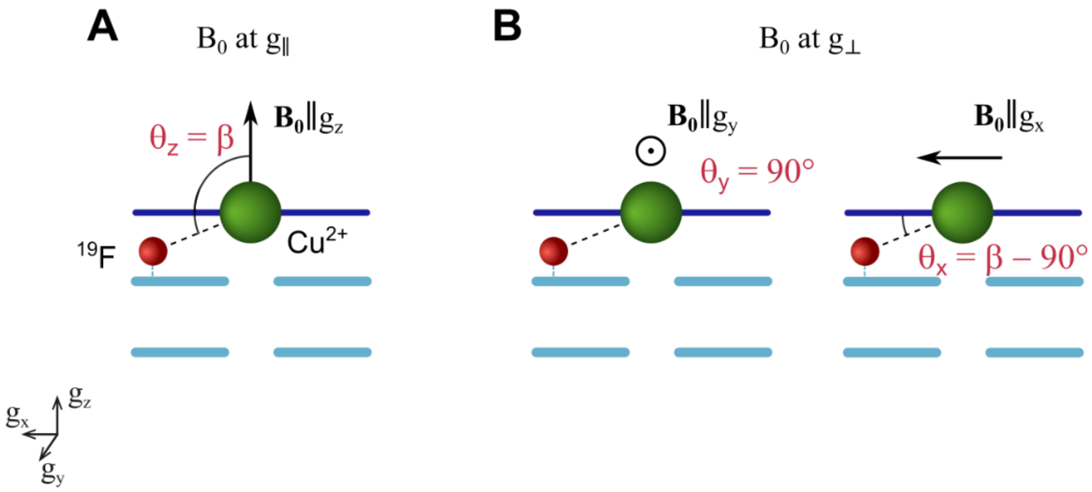

Figure 23: **A**, **B**: Angle θ between *d* and **B₀** for the three orientations of the magnetic field along the canonical directions of the Cu^{2+} g-tensor for the ^{19}F labeling in positions **a**/**f**. Due to the structural similarity of the species GQ1/GQ3, the two cases are described by the same diagram. **C**, **D**: The same for **GQ2**/**GQ4**, characterized by a larger nuclear angle $\beta_{2.4} > \beta_{1,3}$ and longer inter-spin distance $d_{2,4} > d_{1,3}$

At the field position **a**, the **B₀** vector is along the parallel orientation of the Cu^{2+} g-tensor (**B₀** ∥ g_z), and microwave pulses excite strictly $g_{\|}$ (g_z, Figure 23A). Here, angle θ_z coincides with β; and the expected value of β (and θ_z) for **GQ1**/**GQ3** is slightly higher than 90° (Figure 23A). Thus, an ENDOR experiment performed at position **a** excites a single dipolar tensor orientation close to the perpendicular one. This results in one narrow ENDOR feature on each side of the ^{19}F nuclear Larmor frequency. In contrast, when the **B₀** vector is in the $g_\perp$ (g_x, g_y) plane, a broad range of inter-spin vector orientations are excited, with **B₀** ‖ g_y and **B₀** ‖ g_x imposing two limiting cases. For **B₀** ‖ g_y, θ_y is strictly 90°, while for **B₀** ‖ g_x, θ_x is expected to be close to zero ($\theta_x = \beta - 90°$) for the ^{19}F tag at **GQ1**/**GQ3** (Figure 23B). Thus, sampling a large range of θ values at $g_\perp$ from strictly perpendicular(θ_y) to nearly parallel (θ_x) results in a broad ENDOR feature with two maxima, as observed at the field position **g**.

For the intermediate field positions between the $g_\parallel$ and $g_\perp$ regions (labeled **b** – **f**), the spectra become too complicated for the simple geometrical analysis. Nevertheless, building on this semi-qualitative analysis in combination with the full explicit hyperfine tensor, all ENDOR traces could be reproduced well in the spectral simulations (dashed red traces in Figure 22). Note that the distinct ENDOR pattern observed for **GQ2^{C}**/**GQ4^{C}** is based on the same geometrical considerations and explained by a larger β angle compared to **GQ1**/**GQ3**.

Table 3: The isotropic hf term (A_{iso}), ^{19}F angular position (β), and distance between Cu^{2+} and ^{19}F (*d*) obtained from the orientation-selective ENDOR simulations for the GQ species **GQ1**–**GQ4**. The experimental uncertainties were estimated as ranges where the RMSD reaches 115% of its minimal value (**Figure S8**).

Sample	$A_{iso,sim}$ / kHz	β_{sim} /deg	d_{sim} / Å
GQ1	−1 ± 6	98 ± 5	8.2 ± 0.1
GQ3	-1 ± 6	100 ± 4	8.3 ± 0.1
GQ2^{C}	0 ± 8	131 ± 7	10.7 ± 0.4
GQ4^{C}	2 ± 10	130 ± 10	10.5 ± 0.5

Spectral simulations accompanied by root-mean-square deviation (RMSD) analysis between the simulated and experimental traces yielded precise values for the length of the Cu^{2+}–^{19}F inter-spin vector (*d*) and the orientation of the inter-spin vector with respect to the g_z axis (β) (Table 3). The pepper and saffron functions of Easyspin were applied to best match the echo-detected EPR and ENDOR data, respectively.[174]

When simulating ENDOR, the inter-spin distances (*d*), nuclear orientation (β), and the isotropic hyperfine term (A_{iso}) were varied individually in small increments. Every orientation-selective ENDOR trace was simulated for each parameter set, and the RMSD value was calculated between the simulated and experimental traces. The optimal set of *d*, *β*, and A_{iso}, representing the parameters that yielded the lowest RMSD, was selected.

The isotropic hf term was found to be nearly zero for all labeling positions. Both *d* and *β* are smaller for **GQ1**/**GQ3** than for **GQ2^C^**/**GQ4^C^** (*d* ≈ 8.2 Å and *β* ≈ 100° *vs* *d* ≈ 10.7 Å, *β* ≈ 130°, respectively). Due to broader lines and remains of unfolded GQ in the positions **a**/**b** of **GQ2^C^**/**GQ4^C^**, the error margins are larger for these samples compared to **GQ1**/**GQ3**, nicely visible in the larger blue areas in the RMSD plots (Figure S8). The detected *β* angles agreed well with the expected values for 'up' and 'down' conformations (Figure 20). To relate the experimentally derived data to computationally derived models, Dr. Lukas Stratmann, from the Clever group, first performed MD simulations on the ^{19}F-labeled species **GQ1** and **GQ3** and selected structural snapshots with matching Cu-F distances and high symmetry.[18] Based on these structural models, density functional theory (DFT) calculations were made by the group of Dr. Dimitrios Pantazi at the Max-Planck Institut für Kohleforschung. DFT calculations on MD snapshots with *d* = 8.359 Å and *d* = 8.391 Å for **GQ1** and **GQ3**, respectively, reproduce the hf coupling tensor determined by ^{19}F ENDOR, which confirms the consistency of the point dipole approximation for this system. Moreover, the spin density distribution is correctly described by DFT (**Figure 24**).[175] The computed tensors agree well with the experimental values.[18]

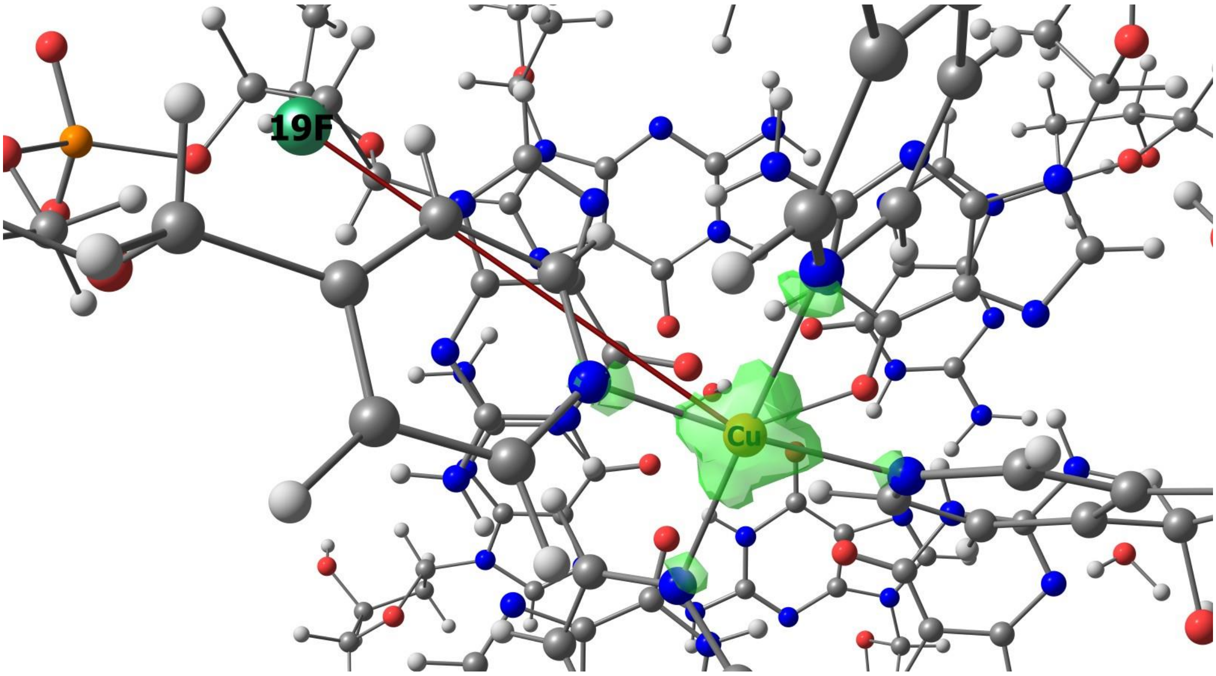

Figure 24: Spin density distribution of **GQ3** visualized from the DFT results. Cu^{2+} is shown in gold and ^{19}F in dark green. The connecting vector is shown as a red line. The electron density is shown as a light green cloud with 78% on the Cu^{2+} atom and 5% on each coordinating nitrogen (blue) atom.

Overall, the position of the Cu^{2+} ion in the center above the G-quartets could be determined. Additionally, ^{19}F ENDOR shows to be very precise in this system, with errors of 0.5 Å and less. Computational chemistry methods confirmed these results. The next step involves investigating the performance between 34 GHz and 94 GHz.

4.1.3. Comparison of ^{19}F ENDOR results at 34 GHz and 94 GHz.

While the previous section shows the efficiency and accuracy of ^{19}F ENDOR distance measurements at 34 GHz, the question remains about additional advantages or disadvantages compared to the application at 94 GHz, besides the necessity of background subtractions. For direct comparison, **GQ3** and **GQ4** were measured at both 34 GHz and 94 GHz. As the 94 GHz sample tubes are too thin for frozen transportation, the sample was filled at the MPI CEC in the group of Dr. Alexander Schnegg. In the case of **GQ4**, this procedure resulted in the broadening of EPR and ENDOR signals due to partial denaturation of the GQ when prepared at room temperature.

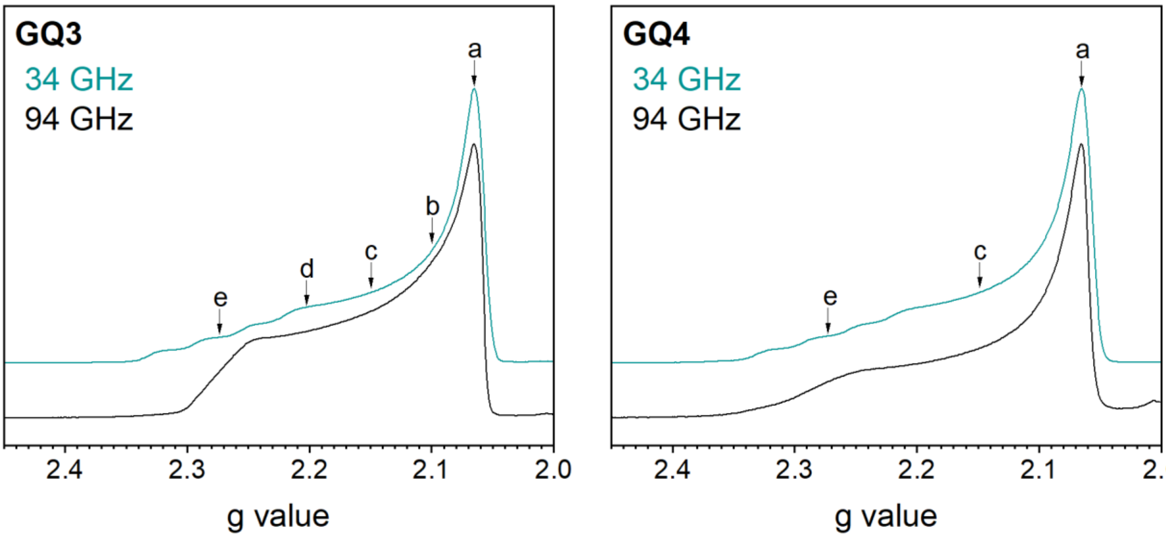

Figure 25: Echo-detected EPR spectrum for **GQ3** (left) and **GQ4** (right) recorded at 34 GHz (blue) and 94 GHz (black). The respective resonance positions for Mims ENDOR are indicated with **a** – **e**.

For comparison purposes, the resonance positions for the Mims ENDOR measurements are chosen by g-value. **a** to **e** are attributed to a fixed g-value, and the corresponding field position is calculated for the respective microwave frequency. As 94 GHz measurements are susceptible to subtle differences in g-value, the loss of hyperfine resolution in the low field area is attributed to visible g-Strain broadening (Figure 25).[170,176]

Further, the large g anisotropy results in different spin package behaviors over the whole envelope. This is especially visible when comparing the 94 GHz EPR spectra of **GQ3** and **GQ4**; slight differences in power optimization led to an intensity shift between the $g_{\parallel}$ and the $g_{\perp}$ regions. In general, the power optimization of the $g_{\perp}$ leads to an overrotation of the spin packages at the $g_{\parallel}$ region, resulting in lower intensities, similar to the 34 GHz measurements (Figure 16B).

A significant difference between the two frequencies was observed concerning the relaxation times. At 94 GHz, T_m time decreased by around 25% at 15 K compared to 34 GHz (Figure 26). The same trend is visible for both stimulated echo and Hahn echo sequence T_m measurements. Lowering the temperature to 5 K leads to a decrease in T_m differences for the stimulated echo sequences. The difference between the frequencies remained in the Hahn echo (primary) sequence. Similar differences in T_m for copper complexes at 34 GHz and 94 GHz were reported before.[177] Multiple papers discussed them as dependent on shortening spin-lattice T_1 relaxation through direct process relaxation or molecular liberations at high frequencies.[178,179] These papers could not prove a clear correlation with T_1 or molecular liberations, but the topic remains highly interesting.

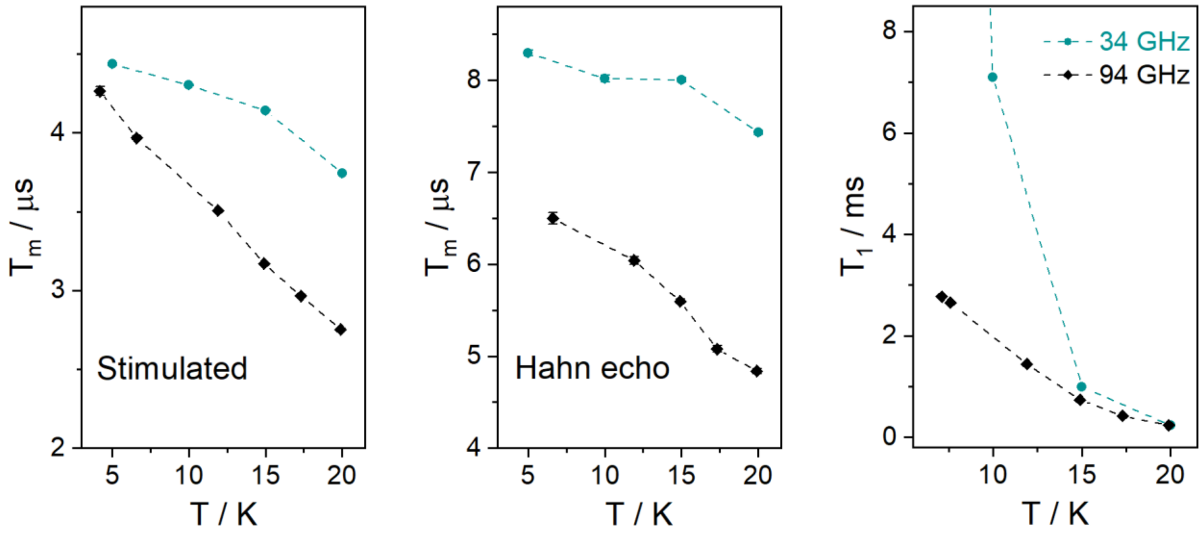

Figure 26: Overview of the temperature- and mw-frequency-dependent T_m and T_1 relaxation times of **GQ3** at position **a**. The types of electron spin echo used for the T_m measurements are indicated in the plots (for the stimulated echo sequence, the T interval was 49 µs). The T_1 times were determined from mono-exponential simulations of the inversion recovery traces. The T_m times were determined from stretched-exponential simulations of the decay traces (stretching exponents *c* = 1.46 and 1.52 were used for the stimulated and primary echoes at 34 GHz; *c* = 1.39 and 1.16 for the stimulated and primary echo at 94 GHz). While similar T_m behavior has been reported for copper and vanadium complexes, the exact mechanisms of the T_m frequency dependence are still debated.[177,178] Dr. Yury Kutin performed some of the measurements.

In this system, a clear difference in T_1 relaxation is visible below 10 K, while for 34 GHz T_1 starts to grow exponentially; for 94 GHz, a further linear increase (for the observed temperature region 20 – 4 K) is visible.

Cooling the system down to 4 K prolonged T_m at 94 GHz to a similar length as at 34 GHz. Enabling to optimize the Mims measurement for ^{19}F sensitivity identically. As T_1 increased, as expected for lower temperatures, the measurement time at 94 GHz increased to nearly double the time necessary at 34 GHz for the same amount of scans. Here we see a correlation with the shortening of the shot repetition time (SRT), representing T_1. At 94 GHz and 4.4 K, the SRT is roughly ten times shorter than at the comparable temperature of 5 K at 34 GHz. Thereby supporting the hypothesis of field-dependent T_m through the dependence on T_1.

The disadvantage of necessary background measurements is diminished as the combined measurement time of primary spectra and background at 34 GHz lays lower or equal, depending on the field position, as the 94 GHz measurement time at the same position.

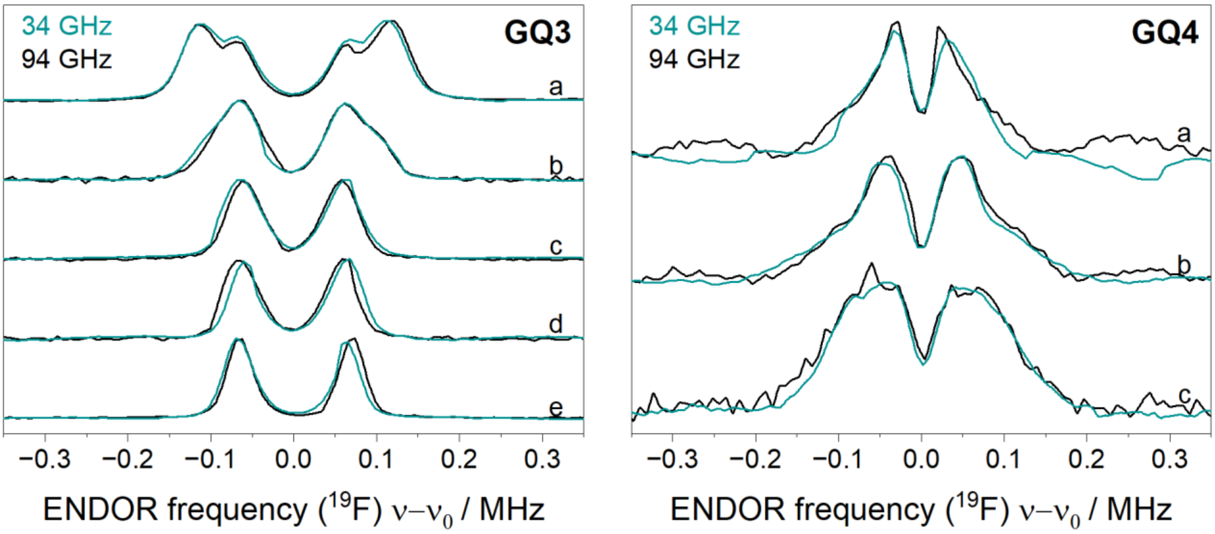

Figure 27: Comparison of orientation-selective Mims ^{19}F ENDOR spectra collected at the marked field positions (**Figure 25**) at 34 GHz (15K, blue) and 94 GHz (4.4 K, black) for **GQ3** (left) and **GQ4** (right), respectively. Each spectrum was normalized to its maximum intensity.

Comparing ^{19}F ENDOR spectra at 34 GHz and 94 GHz showed almost identical line shapes due to significant g-anisotropy already resolved at 34 GHz (Figure 27). The 94 GHz spectra did not provide additional structural information and could be simulated using the ^{19}F hf tensor determined at 34 GHz for **GQ3** (Figure 28) and did not reveal any chemical shift anisotropy reported for 94 GHz ENDOR spectroscopy in the literature.[151]

Remarkable **GQ4** exhibits similar behavior in both cases, indicating specific conformations of GQs in the sample (Figure 25). The multitude of possible configurations due to denaturation makes it not feasible to fit multiple ^{19}F atoms into the spectrum, as no specific number of configurations could be determined. As the necessary equipment was not available during the stay at the MPI, no **GQ4$^{\mathbf{C}}$** sample could be prepared for 94 GHz measurements.

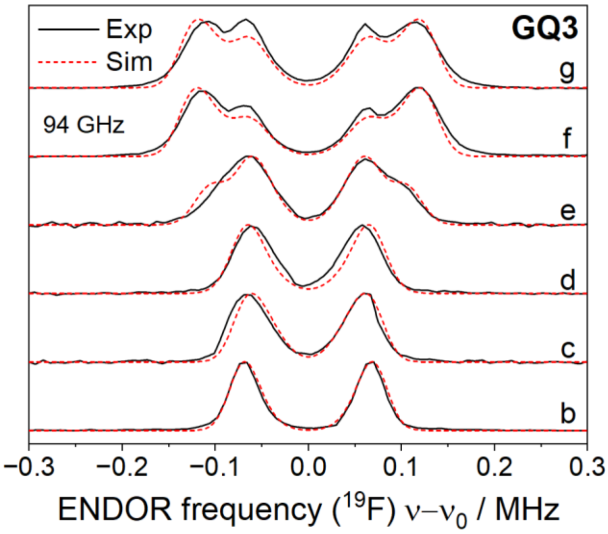

Figure 28: Normalized orientation-selective ^{19}F Mims ENDOR spectra of **GQ3** in deuterated buffer recorded at 94 GHz (black traces), overlaid with spectral simulations (red dashed traces). Simulations employed the ^{19}F hf tensor obtained from the 34 GHz dataset without additional optimizations (**Table 3**).

Notably, the ENDOR line width remained almost unchanged between the two frequencies in this project (FWHM ≈ 36 kHz for **GQ3** at $g_{\|}$). On this basis, the analysis of SNR was performed on **GQ3**.

The signal-to-noise ratio per 1-hour measurement time (SNR_{1h}) is assessed for the ^{19}F ENDOR traces at 34 and 94 GHz, as depicted in Figure 29, obtained at the EPR intensity maximum (field position **a,** Figure 25). SNR_{1h} was computed as the ratio of the ENDOR peak intensity (I) to the representative value of the noise standard deviation (σ), normalized to the square root of the acquisition time (t_{acq}) in hours.[180]

$SNR_{1h} = \frac{I}{\sigma\sqrt{t_{acq}}}$ (see Table 4).

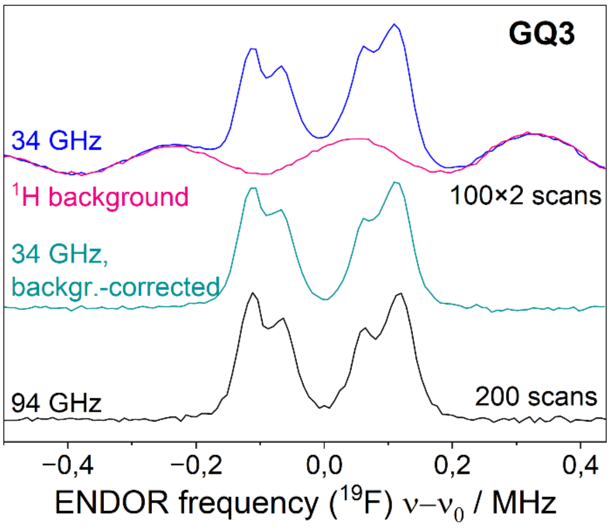

Figure 29: ^{19}F ENDOR spectra of **GQ3** at 94 GHz (black trace) and 34 GHz (blue trace: as recorded; green trace: background-corrected; the ^{1}H background is shown in pink) collected at the field position **a** (**Figure 25**). To visualize

the SNR comparison, the 94 GHz trace was accumulated for 200 scans (SRT = 4 ms), while the 34 GHz ^{19}F trace and ^{1}H background were each accumulated for 100 scans (SRT = 3 ms).

The SNR calculations for the 34 GHz spectrum were affected by the proton background subtraction. The acquisition time was derived from the combined measurement times of ^{19}F ENDOR and ^{1}H background. Interpolating the background trace to its respective ^{19}F ENDOR frequency axis smoothed the background signal slightly, reducing its noise standard deviation. Additionally, the background subtraction residuals perturbed the calculated σ values as their magnitude was similar to the noise intensity. Therefore, the SNR comparison between the 34 GHz and 94 GHz data is approximate. Moreover, shorter mw pulses are typically achievable at 34 GHz, enhancing the SNR.

Table 4: The signal-to-noise ratio normalized to the measurement time (SNR_{1h}) for the ^{19}F ENDOR traces at 34 GHz and 94 GHz. The uncertainty was estimated by determining the σ value for the low- and high-frequency parts of the noise background.

Field position	SNR_{1h} 34 GHz	SNR_{1h} 94 GHz
a	230 ± 30	170 ± 60

The ENDOR SNR1h value at 94 GHz remained relatively constant within the 5–15 K temperature range. As the temperature decreased, the increase in signal intensity, attributed to Curie's law and the extended relaxation time (T_m), was balanced by the rise in shot repetition time (SRT) due to the increasing T_1 time (see Figure 26). As a result, at 94 GHz, the optimal temperature can only be determined concerning the T_m time and, consequently, τ optimization.

In general, ^{19}F ENDOR is better applied on metal-incorporated GQs at 34 GHz. Cooling down below 5 K at 94 GHz, which is only possible with rare cryo-free setups, is necessary for optimal ^{19}F performance due to T_m times. This prolongs measurement times in a way that overcompensates all benefits, like the absence of background subtractions. To test this further, the limits of 19F ENDOR at 34 GHz are tested in the following chapter.

4.1.4. Distance and resolution limits of ^{19}F distance determination

After the general determination of the Cu^{2+} position relative to the remaining tetrads in the GQ and the feasibility of ^{19}F ENDOR distance measurements at 34 GHz, the edge cases are investigated. What is the distance limit achieved by these methods, and how well can dynamic systems be investigated?

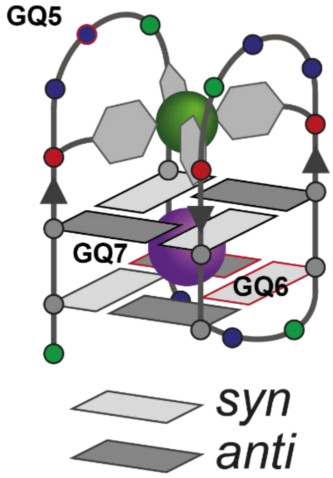

Figure 30: Schematic structure of the folded GQ modified with four pyridine-ligands. One ^{19}F-containing guanosine was incorporated at one of the highlighted G positions in **GQ5**-**GQ7**. Bound Cu^{2+} and K^{+} cations are represented as green and purple spheres, respectively.

To answer these questions, the GQ was modified at three new positions (Figure 30). One thymidine in the loop region was replaced with 2′-fluoro-2′-deoxyuridine (**GQ5**). Additionally, two positions in the lower tetrad were labeled with 2′-fluoro-2′-deoxyguanosine again (**GQ6**/**7**).

GQ5 in the loop is a unique case; the melting temperature is 4 °C higher than that of **GQ1** and **GQ3**, indicating a more stable conformation of the GQ while at the same time showing more flexibility due to the visible ESE line broadening (between **GQ3** and **GQ4**, Figure 17B).[18] While ^{19}F incorporation into the anti-configured guanosines stabilizes the GQ, possibly due to the electron-pulling effect of the fluorine, the seemingly stabilizing properties of the **GQ5** position are less explainable due to the loop's fully flexible position. Coordination of uridine, replacing the thymine, to the Cu^{2+} could not be observed directly in any EPR measurements for **GQ5** (Figure 31).

In general, all three samples exhibit the same expected axial Cu^{2+} symmetry as the previous sample and can be simulated with the same parameters as **GQ1** – **GQ4** (Figure 31). While **GQ6** is simulated with slightly different g-values, this very small change can be explained by differences in the sample optimization between me and

Thorsten Bürger, who conducted his master thesis in the research group of Prof. Kasanmascheff.

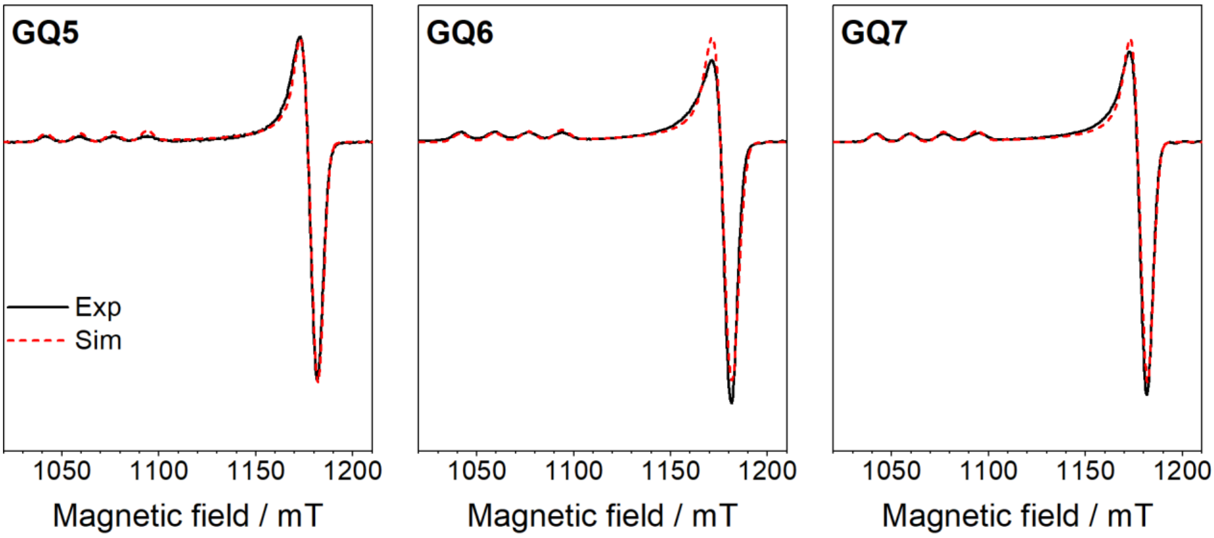

Figure 31: First-derivative ESE spectra of **GQ5** – **GQ7** recorded at 34 GHz (black traces) with simulations (red dashed traces). The simulation parameters are $g_{\perp}$ = 2.061, $g_{\parallel}$ = 2.275, $A_{\parallel}$ = 555 MHz, H-Strain = [200 240] MHz for **GQ5** and **GQ7,** and $g_{\perp}$ = 2.062, $g_{\parallel}$ = 2.275, $A_{\parallel}$ = 555 MHz, H-Strain = [250 300] MHz for **GQ6**. The first-derivative spectra were obtained with a modulation amplitude of 4 mT by pseudo field modulation.[168]

The conformational heterogeneity of **GQ5** resulted in broad and poorly resolved ^{19}F ENDOR spectra (Figure 32). Previously, **GQ2/4** also showed broad ^{19}F spectral features due to partially unfolded GQ samples (Figure S5). However, unlike these samples, ^{19}F labeling in **GQ5** did not destabilize the GQ structure. Thus, the broad ENDOR features observed for **GQ5** demonstrate the flexibility of the loop region (Figure 32).

These findings highlight the ability of ^{19}F ENDOR at 34 GHz to identify dynamic regions within folded DNA structures. For this very flexible region, no simulation of single ^{19}F configurations is feasible. Instead, a multitude of distances is calculated to estimate the range. Distributions in the inter-spin distance and ^{19}F angular position resulted in a large and anisotropic ENDOR line width. The ranges of the inter-spin distance and ^{19}F angle values for **GQ5** were estimated from the extension of simulated ENDOR traces beyond the experimental traces' lower- and higher-frequency edges (Figure S9). Based on the simulations, for inter-spin distances $d \gtrsim 8.1$ Å, the simulated ENDOR lines clearly shift to lower frequencies compared to the experimental traces (Figure S9A). For distances, $d \lesssim 7.3$ Å, the simulated ENDOR traces extend to frequencies higher than those of the experimental envelopes (Figure S9F). Thus, the average inter-spin distance is estimated to be in the range of 7.4–8 Å, and the average angular position in the range of 50–70 °.

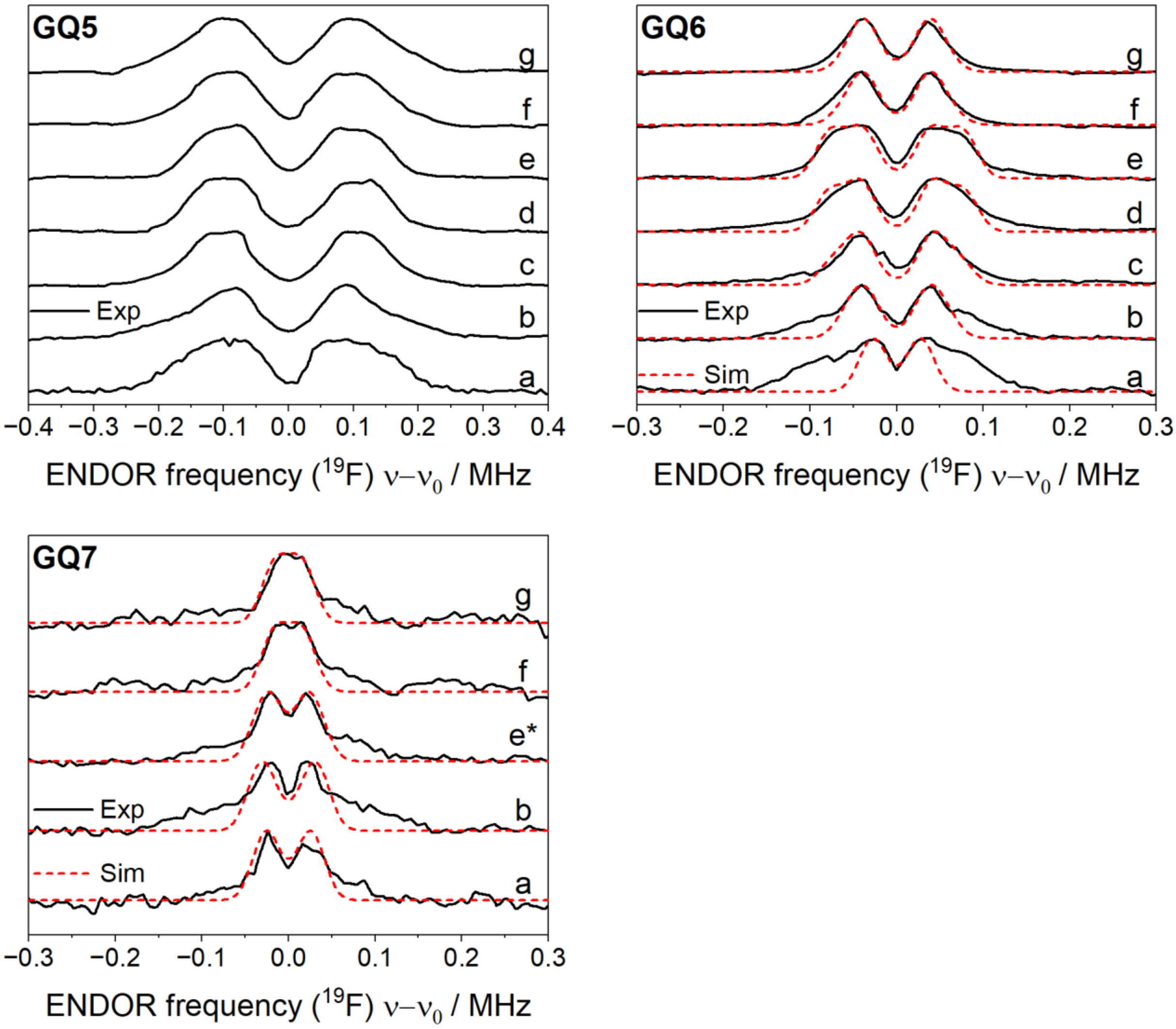

Figure 32: Background-subtracted orientation-selective ^{19}F Mims ENDOR spectra of **GQ5** – **GQ7** at the field positions marked in Figure 19 (black traces, **e***, *g*= 2.112, is shifted slightly towards **d** compared to **e**), with spectral simulations for **GQ6** and **GQ7** (red dashed traces). Each spectrum was normalized to its maximum intensity; the traces were shifted vertically for clarity. The broad spectral features for **GQ6** originate from the denatured GQ fraction.

In the lower tetrad positions, **GQ6** and **GQ7**, the same principles as for **GQ1** – **GQ4** are anticipated to apply. When ^{19}F is incorporated into the guanosine at the syn-configuration, the GQ gets destabilized. For **GQ6,** the ^{19}F ENDOR spectra are broad, similar to the flexible position **GQ5** or the destabilized **GQ2** and **GQ4** samples. As **GQ6** is fixed inside the second tetrad and **GQ7**, the neighboring position, does not show exesive broadening, a similar flexible position as **GQ5** can be ruled out. Therefore, this effect is attributed to its syn-configuration, similar to **GQ2** and **GQ4**. Due to the structure of the GQ, **GQ6** is facing upwards with the shorter expected distance, while **GQ7**, in the more stable anti-configuration, is facing downwards from the Cu^{2+} (Figure 30). In this case, the longer, more stable distance of **GQ7** is of higher interest to determine the resolution limits of this technique at 34 GHz. **GQ6**, with the shorter distance and visible strong line broadening, is less meaningful for the analysis. Nevertheless, a good simulation fit can be achieved with the values in Table 5.

Table 5: The isotropic hf term (A_{iso}), ^{19}F angular position (β), and distance between Cu^{2+} and ^{19}F (d) obtained from the orientation-selective ENDOR simulations for the GQ species **GQ6** and **GQ7**. The experimental uncertainties were estimated as ranges where the RMSD reaches 115% of its minimal value (**Figure S10**).

Sample	$A_{iso,sim}$ / kHz	β_{sim} /deg	d_{sim} / Å
GQ6	0 ± 12	125 ± 8	9.7 ± 0.5
GQ7	2 ± 17	142 ± 19	12.6 ± 1.2

Analysis of the long-distance **GQ7** shows close to the detectable distance limit with 12.6 Å, as in positions **g** and **f**, a signal is detected, but no splitting is visible. Instead, a single broad line is visible due to the overlap of the two peaks. This indicates that longer distances might not be achievable as with no visible splitting, an analysis is impossible.

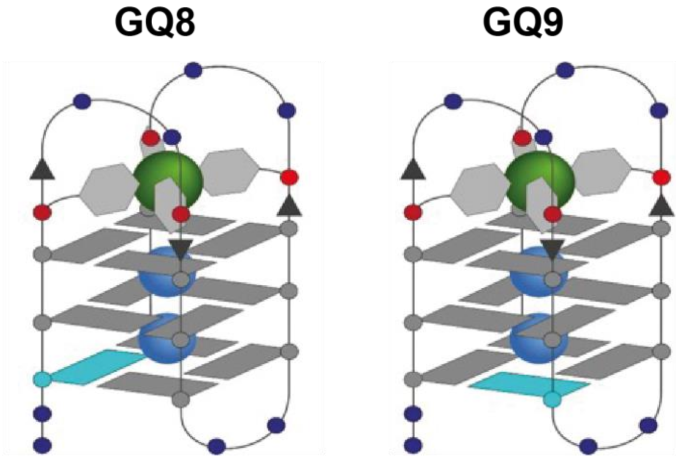

Figure 33: Schematic structure of the folded GQ modified with four pyridine-ligands and three tetrads. One ^{19}F-containing guanosine was incorporated at one of the highlighted G positions (petrol color) in **GQ8**-**GQ9**. Bound Cu^{2+} and K^{+} cations are represented as green and purple spheres, respectively.

Adding another tetrad and labeling it with ^{19}F proved to be too long of a distance (Figure 33). The addition of another tetrad resulted in a topology switch upon Cu^{2+} binding, which could not be observed with EPR.[163] Initial measurements of **GQ8** revealed strong ^{19}F coupling but resulting distances of ~6 Å (Figure 34A). Such a short distance is not feasible in this system as **GQ6** and **GQ7** have longer distances while being closer to the Cu^{2+} side (Table 5). An overhang below the third tetrad could possibly coordinate free Cu^{2+} in the buffer and would explain such short, otherwise impossible distances (Figure 33).

A similar long-distance sample, **GQ9**, was treated with ethylenediaminetetraacetic acid (EDTA) while preparing to complex remaining free or unspecificly bound Cu^{2+} ions. Tests showed that up to three equivalents of EDTA only coordinate free unspecificly bound Cu^{2+} without extracting the Cu^{2+} from the GQ (internal communication). For **GQ9**, no ^{19}F signal was detectable in the Mims ENDOR measurements (Figure 34B). Therefore, the ^{19}F signal of **GQ8** was concluded to originate from additional coordinated Cu^{2+} to the bottom (overhang or loop) of the GQ, next to the ^{19}F labeled guanosines (Figure 33).

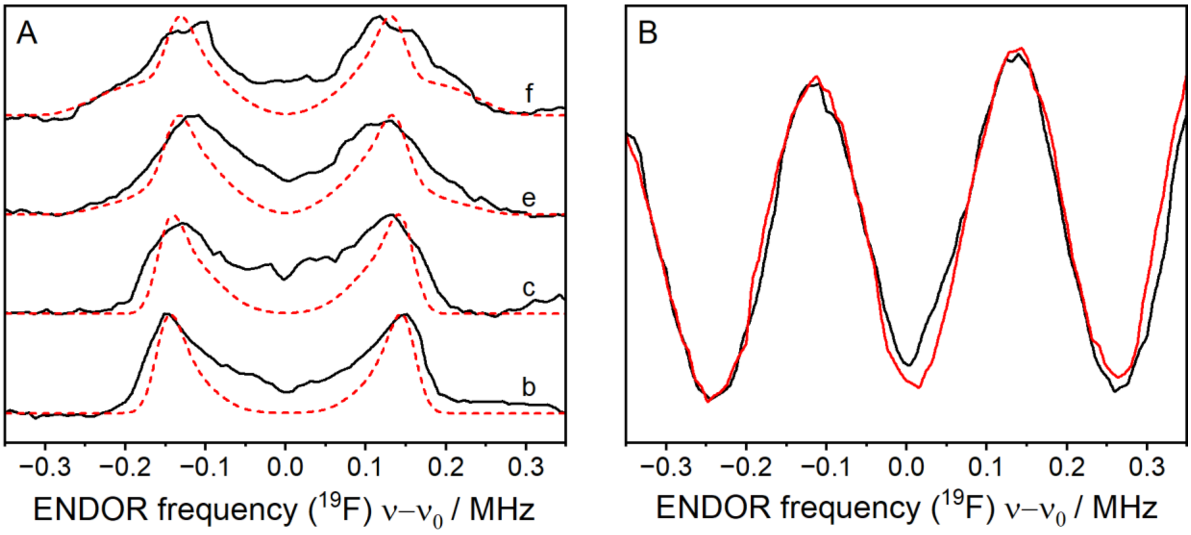

Figure 34: **A**: Background-subtracted orientation-selective ^{19}F Mims ENDOR spectra of **GQ8** at the field positions marked in Figure 19 (black traces), with spectral simulations (red dashed traces). Simulation parameters: g = 2.064 2.268; d = 6.5 Å; β = 100°. Each spectrum was normalized to maximum intensity; the traces were shifted vertically for clarity. **B**: Normalized ^{19}F ENDOR spectra of **GQ9** (black trace) overlaid with a scaled ^{1}H background spectrum (red traces). The τ value is 2 µs at postion f of Figure 19.

Several conclusions can be drawn when comparing the results of the second tetrad samples, **GQ6** and **GQ7**, with those of the first tetrad, **GQ1** through **GQ4**. In both cases, the distance between the upward- and downward-facing ^{19}F atoms is approximately 2 Å. Similarly, a comparable distance can be observed between the tetrads themselves (refer to Table 3 and Table 5).

Figure 35 depicts the standard schematic drawing of a GQ in this thesis and literature;[18,26,27,181] however, it is essential to note that G-quadruplexes are generally wider than tall. The results in this thesis also reflect this, as the upward-facing **GQ6** has a nearly identical, or even shorter, ^{19}F-Cu^{2+} distance in the second tetrad as the downward-facing **GQ4^{C}** in the first tetrad, considering the error margins (9.7 Å vs 10.5 Å, respectively). Comparing the upwards and downwards-facing GQ samples of each tetrad, it is visible that a tetrad's height is approximately 2.5 Å. In contrast, the distance between two tetrads is approximately 1.8 Å.

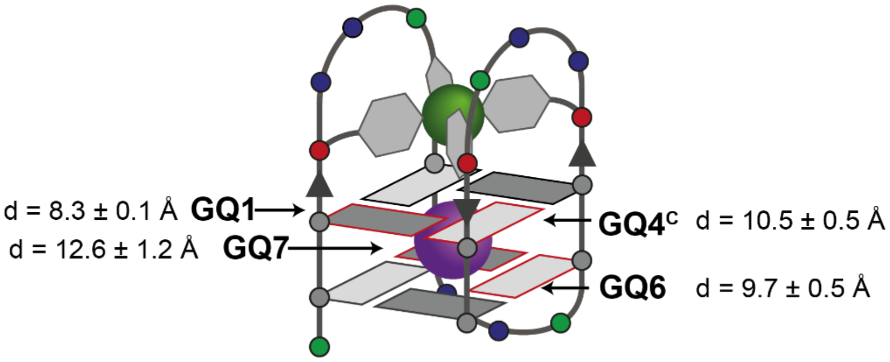

Figure 35: Schematic structure of the folded GQ modified with four pyridine-ligands and three tetrads. One ^{19}F-containing guanosine was incorporated at one highlighted G position (red-lined). Bound Cu^{2+} and K^{+} cations are represented as green and purple spheres, respectively. The measured ^{19}F-Cu^{2+} distances are shown next to the representing GQ name.

Overall, these measurements show the maximum distance detectable in this system using ^{19}F ENDOR is very close to the recorded distance of 12.6 Å for **GQ7**, as longer distances expected in **GQ8** and **GQ9** could not be detected anymore.

4.2. Application of GQ as a Catalyst

An application of metal-incorporated GQs is the use as water-based catalysts, so-called MetalloDNAzyms. The idea developed from the large field of engineered metalo proteins, which catalyze reactions like oxime formation, carbene transfer, imine reduction, cyclopropanation, and ring-closing metathesis.[182–186] While proteins can have a large variety of sequences and methods to bind metal ions, like coordination through amino acids.[159] DNA strands are only made of the four canonical nucleobases, which strongly limit binding possibilities. A solution was the incorporation of chelating ligands into the DNA strand, similar to the pyridine and imidazole ligands used in this thesis.[159] These ligands enabled the development of DNA strands and GQs that catalyze Micheal additions, Diels-Alder reactions, Friedel-Crafts reactions, cyclopropanations, and other transformations.[187–197]

In a recent study about the design of Michael-addition catalysts, multiple different DNA sequences with varying linker positions and linker numbers were screened.[159] It was discovered that three linkers could reliably generate the R conformer, while two ligands resulted in S conformers. This study could not unravel the underlying reason for the conversion and ee-selectivity in general.[159] In this thesis, four sequences were picked and investigated to understand the underlying mechanism. **Cat1** and **Cat2**, with two ligands at slightly different positions (Figure 36), have very similar conversion and ee-selectivity (92% and 90% (S) and 95% and 86% (S), respectively).[159] In contrast, **Cat3**, with three ligands, was found to be the best in terms of enantioselectivity (>99% ee) for the R enantiomer and conversion rate (94%).[159] While **Cat4** was chosen as a “bad” linker position, with low ee-selectivity (84% (R)) compared to **Cat3** (>99% (R)).

The linker position in the sequence differentiates the sequences themselves. For the two linker sequences (**Cat1**/**2**), the linkers are positioned inside the first loop region, with either TLL or LLT, respectively (Figure 36). The difference between the three linker sequences is more significant. Both three linker sequences have one linker in the same position in the first loop and two in the third loop region (Figure 36). Inside this third loop region, the linkers are not just shifted as in **Cat1**/**2** but separated by one T (TLL and LTL, respectively).

htel$_{22}$ Sequence

5'-AGG GTL LGG GTT AGG GTT AGG G-3' → Cat1

5'-AGG GLL TGG GTT AGG GTT AGG G-3' → Cat2

5'-AGG GTL TGG GTT AGG GTL LGG G-3' → Cat3

5'-AGG GTL TGG GTT AGG GLT LGG G-3' → Cat4

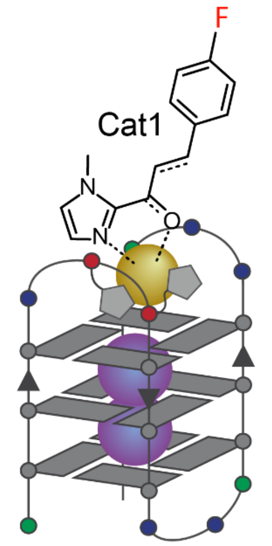

Figure 36: DNA sequences used as MetalloDNAzyms for Micheal-addition reactions from Ref.[159]The sequences harbor imidazole linkers (blue L) at different positions to tune the catalytic activity (**Cat1**—**Cat4**). For ^{19}F ENDOR measurements, the Micheal addition acceptor **MA1** was labeled with ^{19}F at the para position of the benzene ring.[159]

The new imidazole linkers' position in the loop region of the GQ and the reduced number of linkers make the Cu^{2+} environment in the GQs much more flexible than in previous GQs. The remaining open coordination sides of Cu^{2+} are used to coordinate the Michael-addition acceptor **MA1**. For the application of ^{19}F ENDOR, the para side of the benzene ring of **MA1** was labeled with ^{19}F (Figure 36). The same GQ with none labeled **MA1** is used as the background sample.

The different coordination of Cu^{2+} in **Cat1** - **Cat4** leads to variations in the electronic environments, which is particularly evident in the g_z value (Figure 37). These subtle changes are intriguing, as they appear to be critical factors influencing the enantioselectivity and conversion rate of otherwise identical GQ and Michael addition adducts.

Furthermore, the higher mobility of the imidazole linkers causes the features in the low-field region of the ESE spectra to be broader compared to samples with linkers contained within one of the G quartets (e.g., **GQ3**). This broadening effect is addressed in the simulations by employing higher values for the anisotropic residual line width, referred to as H-Strain, in these areas (Figure 32). H-Strain results from unresolved hyperfine couplings or other transition-independent effects.

Overall, Figure 37 highlights the ability to differentiate between the four catalytic samples based on their unique simulation parameters. Although **Cat1** and **Cat4** feature different numbers of linkers positioned in various ways, the electronic configuration of the Cu^{2+} ion appears to be similar in terms of EPR, contrary to initial predictions (see Figure 36). The main distinction lies in the mobility of the Cu^{2+} ion, which is indicated by the parameter H-Strain. **Cat4**, with three linkers, exhibits stronger broadening attributed to its higher mobility, while **Cat1**, which has only two linkers, shows less broadening. These results contradict previous expectations; in theory, a Cu^{2+} coordinated via three linkers in two loops should be more rigid than one with only two linkers.

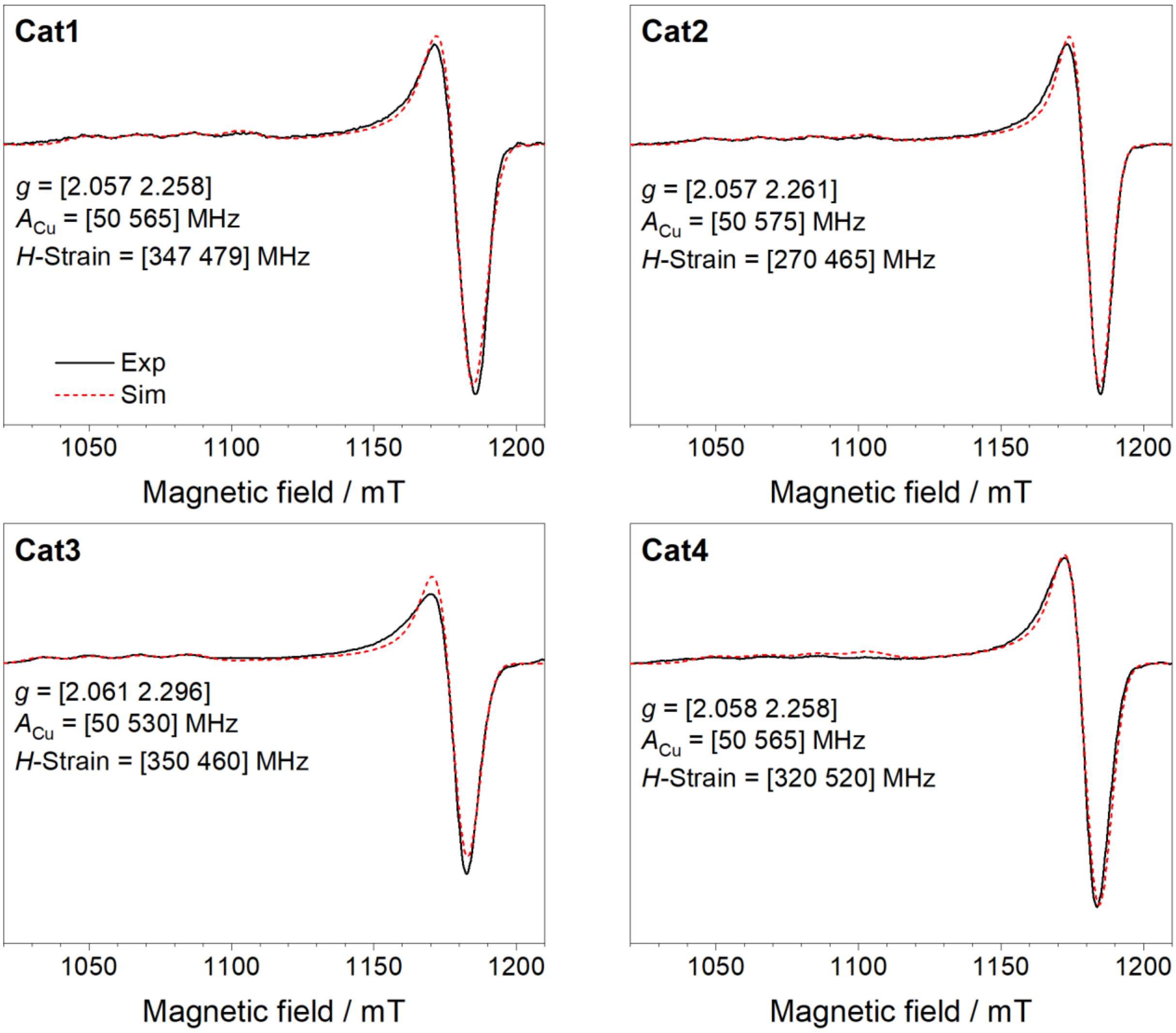

Figure 37: First-derivative ESE spectra of **Cat1** – **Cat4** recorded at 34 GHz (black traces) with simulations (red dashed traces). The simulation parameters are given in the respective graphs as inserts. The first derivative spectra were obtained with a modulation amplitude of 4 mT by pseudo-field modulation.[168]

The ENDOR data in Figure 38 do not show the higher mobility of twice-coordinated Cu^{2+} compared to three-time-coordinated Cu^{2+}. The line broadening is nearly identical for all samples within the SNR (Figure 38), with a similar line shape for all samples in all positions. The differences between the positions and linker numbers are minor and can not be directly explained geometrically, as in **GQ1** – **GQ4**.

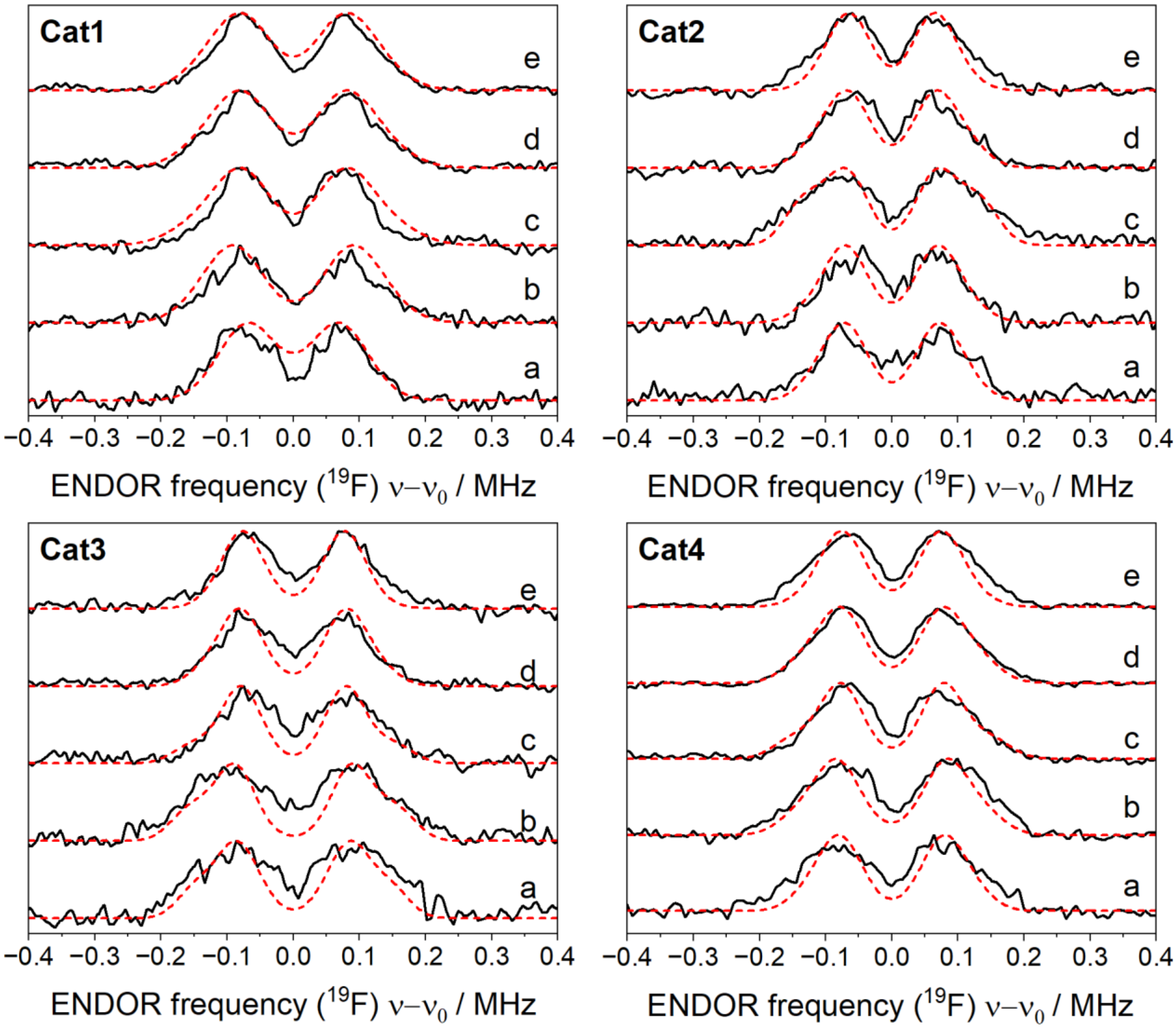

Figure 38: Background-subtracted orientation-selective ^{19}F Mims ENDOR spectra of **Cat1** – **Cat4** at the field positions marked in **Figure S11** (black traces), with spectral simulations (red dashed traces). The simulation parameters are listed in **Table 6**. Each spectrum was normalized to maximum intensity; the traces were shifted vertically for clarity. The broad spectral features for **GQ6** originate from the denatured GQ fraction.

The necessary simulations are not without problems for these catalytic samples (Table 6) either. In the case of axial Cu^{2+}, the simulations result in identical results for angles symmetric around 90° (e.g., 70° and 110°, respectively).

Table 6: The isotropic hf term (A_{iso}), ^{19}F angular position (β), and distance between Cu^{2+} and ^{19}F (d) obtained from the orientation-selective ENDOR simulations for the GQ species **Cat1** – **Cat4**. The experimental uncertainties were estimated as ranges where the RMSD reaches 115% of its minimal value (Figure S12).

Sample	$A_{iso,sim}$ / kHz	β_{sim} /deg	d_{sim} / Å
Cat1	−25 ± 20	57 / 123 ± 6	7.6 ± 0.4
Cat2	-14 ± 18	54 / 126 ± 10	8.1 ± 0.6
Cat3	-25 ± 20	52 /128 ± 5	7.8 ± 0.5
Cat4	-30 ± 16	54 / 126 ± 5	7.7 ± 0.4

For the previous GQ, the angle was, besides **GQ5**, known to be higher than 90° as the Cu^{2+} is located above the GQ in **GQ1** – **GQ7**. Here, the coordination of **MA1** is not known. For **Cat3**, MD simulations showed **MA1** coordinates between the Cu^{2+} ion and the first G quartet (Figure 39), indicating an angle above 90° (Table 6).

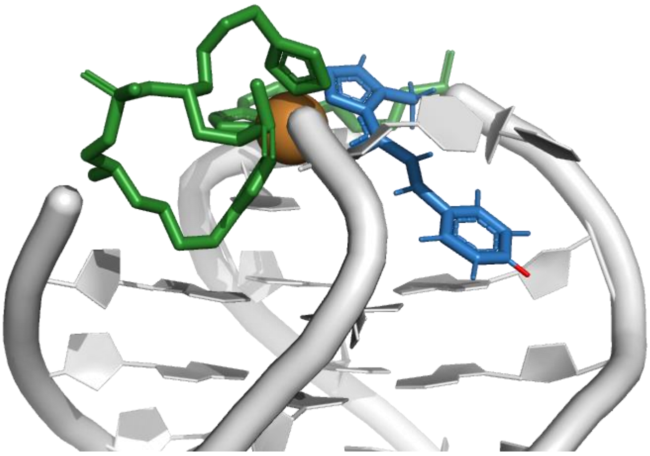

Figure 39: Visualization of the MD results for **Cat3**. The GQ is shown in grey, with the three linkers in green. **MA1** is shown in blue, with the ^{19}F side labeled in red. Cu^{2+} is shown in gold.

No MD data is available for all other samples, and both angles are similarly possible. Further, no reverence of direction is visible in the spectra. The high symmetry between **GQ1**/**GQ3** and **GQ2**/**GQ4** showed a symmetry axis going straight through the GQ, annotated z-axis for the analysis (Figure 22). No such symmetry is visible in the samples, and the z-axis can not be assigned straight through the GQ. Especially under the assumption of high mobility in the linkers coordinating the Cu^{2+}, a location of Cu^{2+} straight on top of the GQ is unlikely. While the position of **MA1** coordination is known for **Cat3**, the unknown Cu^{2+} electronic orientation makes it impossible to assign a fixed angle (between g_z and the connecting vector) for any of these samples.

One solution is the option of double labeling the sample with ^{19}F. Labeling different positions inside the first G quartet would allow to gain one distance and angle set for the **MA1** label and one for the G quartet position if the line broadening allows. By comparing the resulting angles, the g_z orientation of the Cu^{2+} ion can be determined, and a specific angle can be attributed to each label. These samples will be prepared and measured in the future together with additional MD simulations to gain a better understanding of this mechanism. At the current point, all simulation values are within each other's error margin, and no distinction between seemingly good and bad linker positions for catalytic activity can be made.

Additionally, the high flexibility of the linker positions in the loop makes a distinction between double or triple-coordinated Cu^{2+} impossible. A distinction should be resolved through ^{14}N ENDOR measurements. In each sample, the Cu^{2+} ion is coordinated via nitrogen atoms either of imidazole or the **MA1** molecule. As the linkers have different orientations, the ^{14}N ENDOR should allow for differentiation between each ^{14}N atom and, thereby, the linkers and the substrate. The measured ^{14}N Davies ENDOR resulted in mixed results. While Figure S13 clearly distinguishes **Cat1** and **Cat3**, no difference is observed for **Cat3** with and without **MA1**. A clear distinction between two- and three-time coordinated Cu^{2+} can not be made. While the sample can be differentiated, the results of **Cat3** with and without **MA1** raise the question of how exactly **MA1** binds to Cu^{2+}. From the ^{14}N ENDOR results presented here, whether **MA1** binds to the Cu^{2+} via the nitrogen and oxygen atoms is questionable, as shown in Figure 36 and predicted by the MD calculations (Figure 39). **Cat3** has a detectable ^{19}F signal with a distance of 7.8 ± 0.5 Å with seemingly no detectable ^{14}N coupling from **MA1**, which leads to the hypothesis of binding of **MA1** either via the oxygen atom alone or a combination of the oxygen atom with the neighboring C-C double bond (see Figure 36). The ENDOR distance results would support the latter hypothesis as the measured Cu^{2+}-^{19}F distance in the MD structure is 10.6 Å. A distance measured between the oxygen atom and ^{19}F and the bond between the carbon atom and ^{19}F would put the distance in a 6.5 – 8 Å (Figure 40). The actual Cu^{2+} ion position should thereby be somewhere between these two atoms. It is to be noted that these considerations are just estimates made based on the MD structure shown in Figure 40.

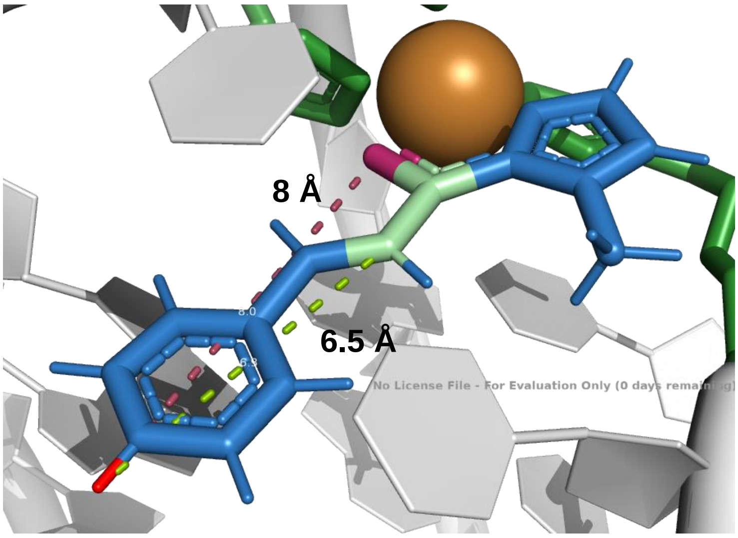

Figure 40: Visualization of the MD results for **Cat3**. The GQ is shown in grey, with the three linkers in green. **MA1** is shown in blue, with the ^{19}F side labeled in red. Cu^{2+} is shown in gold. The oxygen atom of **MA1** is shown in pink, and the C-C double bond is colored in light green. Pymol distance measurements are shown in the respective color with the distances written next to it.

It is somewhat questionable if double ^{19}F labeled samples can resolve these questions, as the line broadening due to the flexibility would remain, and the exact coordination of Cu2+ is still unknown. Preparing these samples at lower temperatures, similar to **GQ2^{C}** and **GQ4^{C}**, could thermodynamically limit the number of configurations the samples can achieve. This could help narrow the line width and differentiate between the binding positions of these samples.

GQ5 demonstrated that flexible regions can be determined in larger molecules. Here, this motion is a significant problem for the analysis. The results show that a direct conclusion on how the linker position influences the enantioselectivity is hard to obtain. Further, the results, especially of ^{14}N ENDOR, suggest that the overall binding of **MA1** to the Cu^{2+} ion in the GQ needs to be questioned and further investigated. Besides double ^{19}F labeled samples, a sample with ^{17}O labeled **MA1** made at 4 °C could help untangle these problems.

In the next step, the efficiency of ^{19}F ENDOR in detecting the binding of a molecule to the DNA directly instead of the Cu^{2+} ion is investigated.

4.3. GQ binder analysis via ^{19}F ENDOR

Besides a molecule directly binding to the Cu^{2+} ion, some molecules bind to DNA strands or GQs. Here, two different binders of DNA GQs themselves, with two different ways of applying ^{19}F ENDOR, are investigated. The first sample has, similar to **MA1**, a single ^{19}F atom in the binder (Figure 41). In contrast, the second sample incorporates the Cu^{2+} into the binder, with a DNA GQ only labeled with a ^{19}F atom (Figure 41).

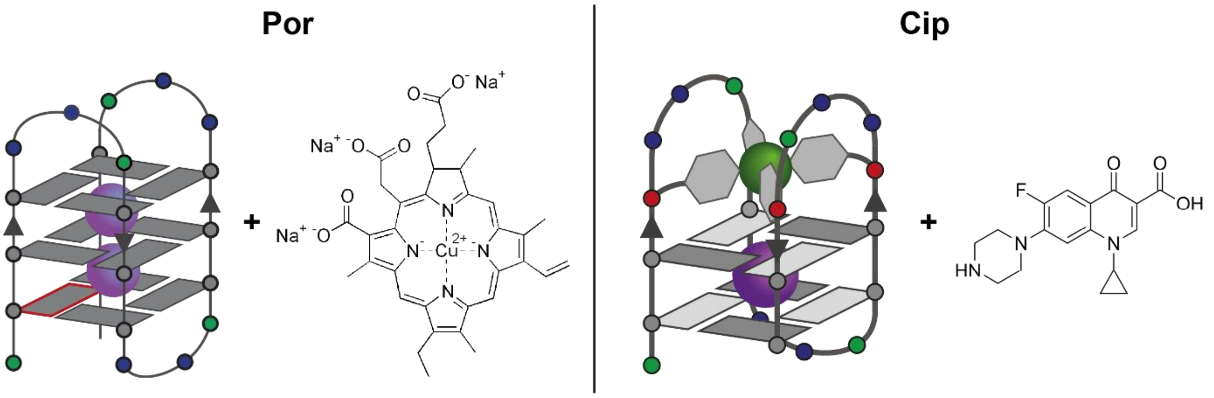

Figure 41: Schematic structure of the GQs with the corresponding binders. One ^{19}F-containing guanosine was incorporated at one highlighted G position (red-lined) for **Por**, the shown DNA sequence is symbolic. The used sequence has an additional tetrad on the top and the loop regions only consist of two thymine. Bound Cu^{2+} and K^{+} cations are represented as green and purple spheres, respectively.

The first tests are performed with **GQ0** mixed with Ciprofloxacin (**Cip**), a widely used antibiotic for treating bacterial infections. Ciprofloxacin advantageously has only a single ^{19}F atom (Figure 41), as before.

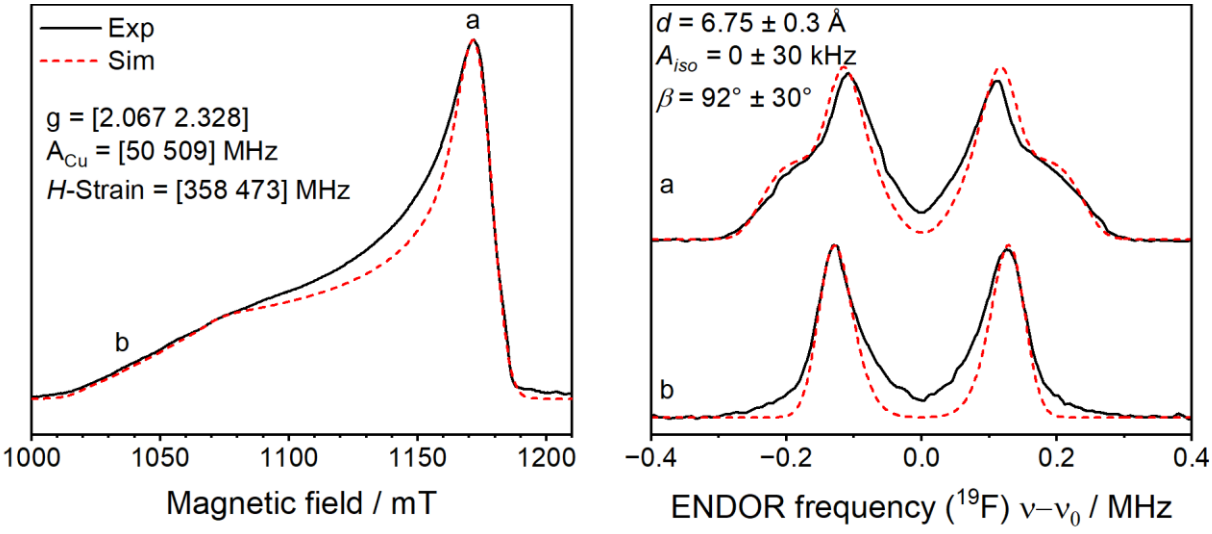

Figure 42: EPR measurements at 15 K of **Cip**. Left: ESE measurement (black) with simulations (red) of **Cip** with simulation parameters listed inside the graph. The sample composition is listed in **Table 7**. Right: ^{19}F ENDOR spectra (black) at positions indicated in the ESE graph with simulation (red). The simulation parameters are shown inside the graph (Line width: 35 kHz).

Cip based on **GQ0** with additional Ciprofloxacin showed very different behaviors than the previous measurements. In the earlier measurements as a background, the Cu^{2+} hf coupling of **GQ0** was resolved in the $g_{\parallel}$ region ($A_{\parallel}$; Figure 18). In Figure 42 (left), after adding Ciprofloxacin, the spectrum got broader, and the hf is no longer resolved, indicating changes to the electronic structure of Cu^{2+} in the GQ. Strong binding of the Ciprofloxacin to the Cu^{2+} ion is the most feasible explanation, as a similar effect was observed for Micheal addition educt binding (Figure 37).

If the Ciprofloxacin is bound directly to the Cu^{2+} ion, a distance of 6 – 8 Å can be expected during ^{19}F ENDOR measurements, similar to previous results of the first tetrad and Micheal addition educt. The measurements in the earlier sections showed that the two principal orientations of the axial g-tensor ($g_{\perp}$: a, $g_{\parallel}$: b; Figure 42) are already enough to resolve most of the hf tensor. Therefore, as a starting point, only these two positions were measured. The spectra showed strong ^{19}F couplings in both orientations with a distance of around 6.75 Å. With two orientations, the distance and angle have a more considerable error margin than these based on more orientations due to a more extensive variety of fitting simulation parameters.

Nevertheless, the change in the electronic structure of Cu^{2+} and the very short Cu-F distance leads to one conclusion. Ciprofloxacin binds directly to the Cu^{2+} ion instead of the DNA GQ. While this result is a new minimal distance for ^{19}F ENDOR (6.75 Å vs. 7.6 Å for **Cat1**), it differs from the intended investigation target. Initially, binding to the GQ itself was targeted to be able to conclude binding modes in Cu^{2+} unmodified systems. The results show that ^{19}F ENDOR, in combination with Cu^{2+} labeling, can resolve complex structural questions with only a few orientations measured. At the same time, measurements at more orientations would decrease the error margins.

The second test sample contains Cu^{2+} harboring Chlorophyllin, a semi-synthetic derivate of chlorophyll, and a DNA sequence forming four G-quartets without the Cu^{2+}-pyridine linker modification (**Por**, Ttel-sequence, Figure 41 left). Here, the first guanine in the sequence is labeled with a single ^{19}F, putting in the first G-quartet (from the bottom) of the GQ (Figure 41).

In Chlorophyllin, the axial symmetry is less pronounced, and the g tensor anisotropy is lower (Figure 43), indicating that incorporating Cu^{2+} into Chlorophyllin has a different electronic environment than that in labeled GQs. Additionally, the hf coupling of Cu is not resolved, and a strong line broadening is observed.

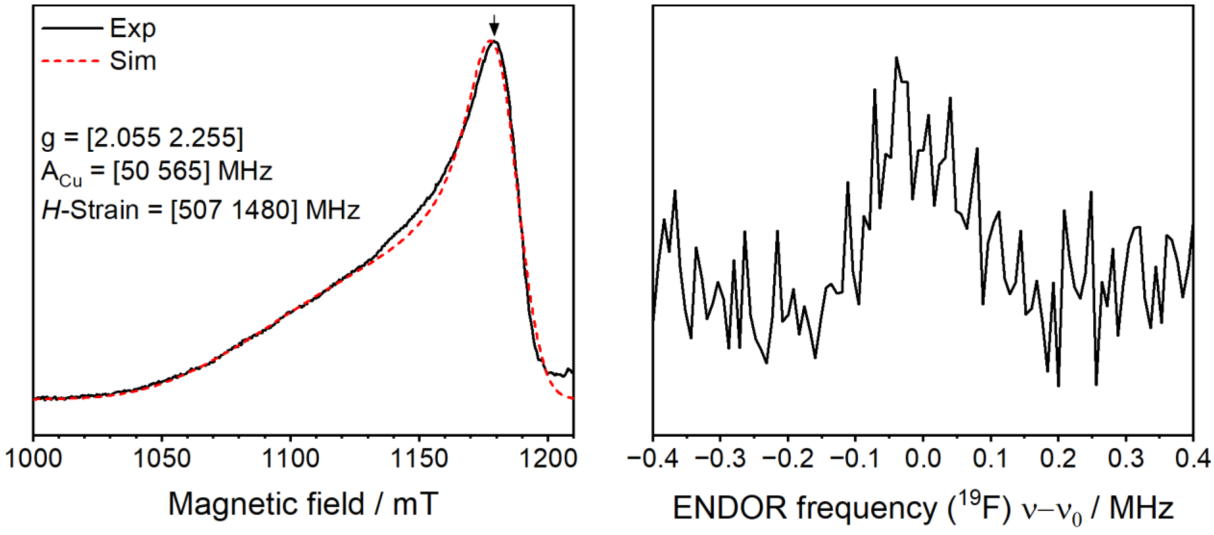

Figure 43: EPR measurements at 15 K of **Por**. Left: ESE measurement (black) with simulations (red) of **Por** with simulation parameters listed inside the graph. The sample composition is listed in **Table 7**. Right: ^{19}F ENDOR spectra (black) at positions indicated in the ESE graph (arrow).

For the ^{19}F ENDOR measurements, the $g_\perp$ orientation with the highest signal intensity was chosen as the best starting point. The resulting ^{19}F spectrum in Figure 43 shows a visible ^{19}F feature between -0.1 MHz and 0.1 MHz. At the same time, the spectrum shows extremely low SNR even after 10 hours of accumulation. As the $g_\perp$ has the highest signal intensity overall, the SNR at other orientations would be lower or require even longer measurement time, probably days.

Due to the very low SNR, further measurements of this sample to characterize the full hf tensor are not feasible. This could be a result of different effects: either the Chlorophyllin binds too far away from the ^{19}F tag, or the concentration of Chlorophyllin bound to the GQ is very low.

Figure 43 indicates the first option to be accurate; a very long Cu-F distance results in low SNR and minimal hf coupling values. Here, a single peak with splitting overlayed by line broadening, indicating binding of Chlorophyllin either to the top of the GQ (loop region) or at least the top half of the GQ as the ^{19}F tag is located in the lowest quartet (Figure 41).

EPR confirmed that Chlorophyllin binds to the GQ, a previously established phenomenon.[198,199] The specific binding mode is still unclear, although the data shown here indicate that it likely occurs at the top of the GQ.

The ^{19}F ENDOR measurement shows that investigating the binding process could be improved with a few modifications, promising new insights into the exact binding process. First, the position of the ^{19}F tag needs to be adjusted, as it is currently located at the bottom of the GQ in the lowest quartet. A more central position in the second quartet is a more reasonable starting position. In the case of a central ^{19}F labeling position in the GQ, Chlorophyllin binding to the sides, top, or bottom of the GQ should result in distances between **GQ1** and **GQ4** as structurally there can not be more than two quartets separating ^{19}F and Cu^{2+}. Further, using multiple different ^{19}F positions would allow the determination of which side of the GQ the Chlorophyllin is bound to.

4.4. Summary and Outlook

This thesis is the first implementation of ENDOR spectroscopy in combination with site-specific ^{19}F labeling for distance determination in a biological macromolecule at 34 GHz.[18] The highly rigid Cu^{2+} spin label designed for DNA G-quadruplexes allows measuring atomic-scale distances in the range of 6 – 13 Å with a high accuracy of up to 0.1 Å, depending on the distance and labeling site. When applying at 34 GHz, the overlap with the underlying proton ENDOR features, an expected drawback, could be successfully subtracted using a reference sample while maintaining a high signal-to-noise ratio of the resulting ^{19}F ENDOR spectra. The ^{19}F ENDOR linewidth is theoretically the main limiting factor in accessing longer distances within GQ structures. The full width at half maximum line width of ~35 kHz for the most narrow feature at $g_{\parallel}$ imposes a limitation of approximately 15 Å. In contrast, **GQ6** showed the practical limit with GQs closer to 13 Å.

Applications for GQ catalytic research and binding investigations have been proven challenging. While all catalytic samples were feasible for measurements, and the general orientation and distance were detectable, the resolution was insufficient to determine the small differences. The central aspect of these resolution problems is the samples themselves. ^{19}F ENDOR distance determination, similar to other dipolar coupling spectroscopic techniques, is highly sensitive to the paramagnetic center position and surroundings. In the case of the catalytic samples, the Cu^{2+} ion is in a very flexible position, which reduces the overall resolution due to a multitude of slightly different conformations. While a clear binding mode could not be obtained, the ^{14}N ENDOR measurements in combination with ^{19}F ENDOR showed that the binding of **MA1** is not the nitrogen atom of **MA1**, as theoretically predicted, but a side closer to the ^{19}F tag. Nevertheless, if mobility could be limited in the sample preparation process, ^{19}F ENDOR was shown to be the proper technique for identifying the correct binding side and mode for intramolecular distances of GQ binders that are not directly bound to the Cu^{2+} ion.

The binder measurements also showed mixed results due to the sample composition. Ciprofloxacin binding resulted in a new minimal resolved distance of 6.75 Å for ^{19}F-Cu^{2+} distance measurements; the intended analysis of binding to the GQ, on the other hand, was not achievable due to binding to the Cu^{2+} ion. The ^{19}F label position for measurements with Chlorophyllin was unsuitable for further analysis of the binding position and mode; nevertheless, it showed promising results for measuring distances between systems that are not directly bound to the Cu^{2+} ion.

For further measurements, the label positions need to be reviewed and adjusted for more precise and reliable measurements. A promising next step for the Chlorophyllin measurements will be using a GQ with ^{19}F tags in the central G quartet to more easily determine the general binding side and distance. This will be followed by specifically labeled samples with ^{19}F sides close to the determined binding side. Alternatively, MD simulations of these complexes could void the first step by predetermining the binding mode and side.

A more rigid Cu^{2+} site would be necessary for analyzing the catalytic GQs. A cooldown of approximately 20 °C during preparation might not be sufficient to limit the degrees of freedom in the linkers. The remaining conformational variants might still be too many to significantly improve the ENDOR resolution. Measurements of double ^{19}F labeled samples together with MD simulation would allow binding orientation analysis.

In general, ^{19}F ENDOR can be used for a wide range of future biomolecular projects at 34 GHz due to well-established ^{19}F incorporation protocols and even commercially available labeled precursors or substances like 2'-fluoro-guanosines in this thesis.

4.5. Material and Methods

All GQ samples in this thesis are part of the collaboration project investigating GQs for different applications between the Kasanmascheff and Clever groups at the TU Dortmund. The samples were prepared by Simon Kotnig in deuterated buffer with deuterated glycerol and delivered in 1.6 mm EPR tubes in liquid nitrogen if not stated differently (Table 7). A detailed sample production procedure and Circular dichroism (CD), NMR, and UV-Vis data are given in Simon Kotnig's PhD thesis and Schumann et al.[18] for samples in the publication. EPR spectroscopy, mass spectrometry, and melting temperature measurements confirmed the incorporation of the metal cations and significant stabilization of the GQ structure due to the metal incorporation. The sample **GQ5** was prepared by Simon Kotnigs, Bachelor student Yana Streltsova, under his supervision. Thorsten Bürger measured **GQ6** within the scope of his Master's thesis.

Table 7: Sample naming and composition of GQ samples prepared by Simon Kotnig.

Sample	Sample name by Simon Kotnig	Concentration / mM	DNA Sequence	Additional information
GQ0	ONSK10	1	5’-AGG LTT ALG GTT AGG LTT ALG G-3‘	Background no fluorine
GQ1	ONSK3		5’-AGG LTT ALG GTT AGG LTT ALG G-3‘	
GQ2	ONSK4		5’-AGG LTT ALG GTT AGG LTT ALG G-3‘	
GQ2^{C}	ONSK4		5’-AGG LTT ALG GTT AGG LTT ALG G-3‘	4°C preparation
GQ3	ONSK7		5’-AGG LTT ALG GTT AGG LTT ALG G-3‘	
GQ4	ONSK8		5’-AGG LTT ALG GTT AGG LTT ALG G-3‘	
GQ4^{C}	ONSK8		5’-AGG LTT ALG GTT AGG LTT ALG G-3‘	4°C preparation
GQ5	ONYS2		5’-AGG LTU ALG GTT AGG LTT ALG G-3‘	
GQ6	ONSK6		5’-AGG LTT ALG GTT AGG LTT ALG G-3‘	Measured by Thorsten Bürger
GQ7	ONSK5		5’-AGG LTT ALG GTT AGG LTT ALG G-3‘	
GQ8	ONSK29		5´-TTG GGL TTL GGG TTG GGL TTL GGG-3´	
GQ9	ONSK34		5´-TTG GGL TTL GGG TTG GGL TTL GGG-3´	

LGQ1	ONSK29	1	5’-TTG GGL TTL GGG TTG GGL TTL GGG-3’	
LGQ2	ONSK30		5’-TTG GGL TTL GGG TTG GGL TTL GGG-3’	
LGQ3	ONSK33		5’-TTG GGL TTL GGG TTG GGL TTL GGG-3’	EDTA treated
LGQ4	ONSK34		5’-TTG GGL TTL GGG TTG GGL TTL GGG-3’	EDTA treated
LGQ0	ONSK35		5’-TTG GGL TTL GGG TTG GGL TTL GGG-3’	Background, no fluorine
Cat1	ONSK49	0.75	5’-AGG GTL LGG GTT AGG GTT AGG G-3’	
Cat1$_B$	ONSK49	0.75		Background, no fluorine
Cat2	ONSK51	0.25	5’-AGG GLL TGG GTT AGG GTT AGG G-3’	
Cat2$_B$	ONSK51	0.25		Background, no fluorine
Cat3	NK05	0.6	5’-AGG GTL TGG GTT AGG GTL LGG G-3’	
Cat3$_B$	NK05	0.6		Background, no fluorine
Cat4	ONSK50	0.25	5’-AGG GTL TGG GTT AGG GLT LGG G-3’	
Cat4$_B$	ONSK50	0.25		Background, no fluorine
Cip	ONSK35	0.25	5’-TTG GGL TTL GGG TTG GGL TTL GGG-3’	Ciprofloxacin added
Cip$_B$	ONSK35	0.25		Background, no fluorine
Por	Ttel_F	0.15	5’-TTG GGG TTG GGG TTG GGG TTG GGG-3’	Cu^{2+} bound to porphyrin
Por$_B$	Ttel	0.15	5’-TTG GGG TTG GGG TTG GGG TTG GGG-3’	Cu^{2+} bound to porphyrin, no fluorine

34 GHz (Q-band) EPR and ENDOR measurements were carried out at 15 K using a Bruker Elexsys E580 spectrometer equipped with a 150 W TWT amplifier (Applied System Engineering, 187Ka), commercial Bruker EN 5107D2 ENDOR resonator, Oxford Instruments CF935 continuous-flow helium cryostat and Oxford Instruments MercuryiTC temperature controller.

Echo-detected EPR spectra were detected using the standard Hahn-echo sequence: $\frac{\pi}{2} - \tau - \pi - \tau -$ echo. The typical microwave (mw) $\frac{\pi}{2}$ pulse lengths was 12 ns, and the τ value was 350 ns.

Mims ENDOR experiments[158] were carried out using a AR 600 W radiofrequency (RF) amplifier (AR 600A225A) with the standard Mims ENDOR sequence: $\frac{\pi}{2} - \tau - \frac{\pi}{2} - T - \frac{\pi}{2} - \tau -$ echo. The time interval T was set to 47 μs and included a 45 μs RF pulse. Shorter RF pulses were achievable but led to the broadening of ^{19}F ENDOR lines. The measurements were performed with 10 shots per point (spp) to speed up data accumulation as described in the literature.[9] The sensitivity loss due to saturation of

^{19}F spins compared to spp = 1 was negligible for the shot repetition time of 3 ms used for all samples. The stochastic RF acquisition was used.[200] The accumulation time was 4–14 hours per trace, depending on the field position, if not stated otherwise in the figures.

^{1}H Davies ENDOR spectra were collected using the same equipment as Mims ENDOR, following the standard Davies[157] sequence: $\pi_{\mathrm{select}} - T - \frac{\pi}{2} - \tau - \pi - \tau -$ echo. The time interval *T* was set to 19 µs and included a 17 µs RF pulse. The π_{select} inversion pulse was set to 200 ns.

EPR analysis is made with the EasySpin plugin for MatLab.[174] ESE spectra are simulated using the pepper function, while ENDOR measurements are simulated using the saffron function.

5. High-pressure tuning of the midpoint potential of Fdx1

High-pressure setups are rare for EPR systems. While other spectroscopic methods, like NMR and Fourier transform infrared spectroscopy, have established setups that showed the potential of high pressure to access otherwise low- or unoccupied energy states essential for some biological processes.[115,121] Establishing a high-pressure setup for EPR spectroscopy requires some changes to these setups, as very low-temperature measurement conditions are often used. Additionally, a reliable model system is needed for the system to be tested.

As such, the Fdx1 (ferredoxin 1) protein in the green microalga *Chlamydomonas reinhardtii*, a model organism for investigating oxygenic photosynthesis within chloroplasts, was chosen.[201,202] It is very well studied and can be expressed and produced relatively easily. Fdx1 incorporates a [2Fe2S] cluster as a central point in the electron pathway during photosynthesis. Its well-characterized midpoint potential of -410 mV makes it an ideal electron acceptor for photosystem I ($E_m =$ -550 mV).[203,204] Thereby, Fdx1 can pass on the electrons received from photosystem I into different pathways. Prominently, two pathways are the transfer of electrons to the NADP$^+$ reductase (FNR) for NADPH production under photosynthetic conditions and the transfer to the [FeFe]-hydrogenase HydA1 for H_2 production under anaerobic conditions.[204–207]

Studies are being conducted to improve the interaction between Fdx1 and HydA1 to enhance the effectiveness of electron transfer.[208,209] The success of this process depends on various factors, such as the distance between the electron donor and acceptor, protein-protein interactions, and differences in midpoint potentials.[210]

This thesis focuses on the influence of pressure on the midpoint potential. The midpoint potential is the redox potential at a given temperature and pH value at the center of a redox titration curve where the reductant and oxidant are equal.

Midpoint potentials can vary drastically between systems depending on multiple influences.[211] First, the metal center in these metal-proteins plays a crucial role in the midpoint potential. Copper, for example, sits more on the higher end of the potential range, while iron is often a low midpoint potential center.[212] Predominantly influenced by the valent states, iron in different iron-sulfur cluster configurations exhibits drastically different midpoint potentials, as [4Fe4S] clusters transition from a 2+ to 3+ oxidation state while [2Fe2S] transition from 1+ to 2+.[211] The number of metal centers is also an important determining factor, even if these are not spacially close by, as electrostatic interactions and aromatic groups showed a mediator effect.[213] A second influencing factor is the ligands in the primary coordination sphere. The ligands influence the potential in different ways. Geometry and electronic properties are important as some metals can prefer specific geometries in different oxidation states or either soft or hard ligands. In the latter case, harder ligands stabilize higher oxidation states, leading to a decreased midpoint potential.[214] The ligands' electron donating or withdrawing ability also influenced FeS cluster potentials.[211] An important factor for this thesis is the shown influence of slight structural changes of the cluster, like bond angle changes of Fe-S-C_α-C_β.[215–217] A third major group of midpoint potential influencing interactions is found in the second coordination sphere.[211] Hydrophobic environments increase the potential of the metal center as higher redox states are disfavored. Hydrogen bonds can further alter the midpoint potential. Their influence depends on where and how they form. Besides limiting ligand movement by locking them in place, they can alter the properties of the first coordination sphere by establishing a connection to primary ligands, reducing potential. For their full effect, the bonds need to be correctly orientated.[211]

This part of the thesis investigates pressure effects on Fdx1s midpoint potential by facilitating the newly designed and built high-pressure EPR setup. High pressure of up to 4 kbar could cause changes to the ligand position of the first and second coordination spheres through compression of the protein. Additionally, the pressure might lead to water penetration into void spaces inside the protein or the active side of the protein, changing the hydrophobic environment and, thereby, the midpoint potential. All of these possible effects and their results to the midpoint potential can be investigated with EPR under high pressure and could lead to new developments for the design of hydrogen production parthways.

5.1. Sample preparation and methods

The Fdx1 protein was expressed and purified by the Happe group at the Ruhr University Bochum as described in the publication of Heghmanns et al..[218] The protein was provided in aliquots, and the concentration was checked through UV-VIS measurements at 420 nm with a Thermo Fisher Scientific NanoDrop 1000 before use in the potentiometries. Redox potentiometry was performed following the procedure described by Heghmanns et al. with the same equipment described in the publication method section.[218] The temperature-independent buffer with a pH of 7.5 was changed after the first batch from a 60 mM / 40 mM mixture described by Heghmanns et al.[218] to a 30 mM / 70 mM mixture of HEPES and Na_2HPO_4, as described by Le Breton et al..[219] The change was made as the temperature-independent nature of the first mixture is not fully given at pH 7.5.

Table 8: Redox titration sample list. Two titrations were performed by titrating NaDT to the protein solution. The first titration batch was measured with EPR at atmospheric pressure before throwing, applying pressure, and refreezing the samples. For the second batch, the buffer was changed from a mixture of 60 mM HEPES with 40 mM Na_2HPO_4 to a mixture of 30 mM and 70 mM, respectively.

Batch	Sample number	Redox potential / mV	Concentration / µM	Pressure
1	1	-453	199.43	1 bar
	2	-468	198.49	1 bar
	3	-501	197.79	1 bar
	4	-528	197	1 bar & 4 kbar
	5	-560	195.18	1 bar & 4 kbar
	6	-599	194.11	1 bar & 4 kbar
	7	-621	193.45	1 bar & 4 kbar
	8	-637	189.26	1 bar & 4 kbar
2	1	-487	197.18	4 kbar
	2	-504	196.26	4 kbar
	3	-527	194.90	4 kbar
	4	-550	194.14	4 kbar
	5	-562	193.70	4 kbar
	6	-575	192.14	Broken
	7	-591	190.25	Broken
	8	-603	187.87	4 kbar
	9	-620	184.59	4 kbar
	10	-628	171.16	Broken

34 GHz (Q-band) EPR ESE measurements were carried out at 15 K using a Bruker Elexsys E580 spectrometer equipped with a 150 W TWT amplifier (Applied System

Engineering, 187Ka), commercial Bruker ER 5106QT-2 resonator, Oxford Instruments CF935 continuous-flow helium cryostat and Oxford Instruments MercuryiTC temperature controller. The resonator was critically coupled for reproducibility, and measurement parameters were optimized for each sample (Attenuation and Video Gain) and listed in Table 9.

Table 9: Acquisition parameters for 34 GHz ESE experiments performed on Fdx1 samples at atmospheric pressure and 4 kbar.

Parameters	
***T* / K**	15
***π* / ns**	20
***τ* / ns**	650
Shot reputation time / µs	500
Shots per point	100
Attenuation / dB	8 - 9
Video Gain / dB	24 – 42
Field / mT	1237 ± 135
scans	2

5.2. Design and performance of High-Pressure equipment

Different EPR high-pressure setups have found applications in the past, depending on the research interest. The main interest for this thesis and the research group lies in biological macromolecules with either intrinsic or artificial paramagnetic centers. As these systems have very short-lived radical states or incorporate metal ions with relaxation times too short to be measured at room temperature, a setup to measure EPR under pressure at cryogenic temperatures was designed.

For this purpose, an approach similar to that of Prof. Hubbell's group in Figure 8 was termed ideal.[133] The decision was made to make the system easier to operate with fewer error points than the system built by the Hubbell group. The main principle of pressurizing the sample at room temperature, followed by a freezing process under pressure, is retained. In general, the system contains three main parts: the pressure chamber in which the sample is inserted, pressurized, and frozen; the pressure intensifier; and a dewar with an ethanol dry ice cooling bath (Figure 44).

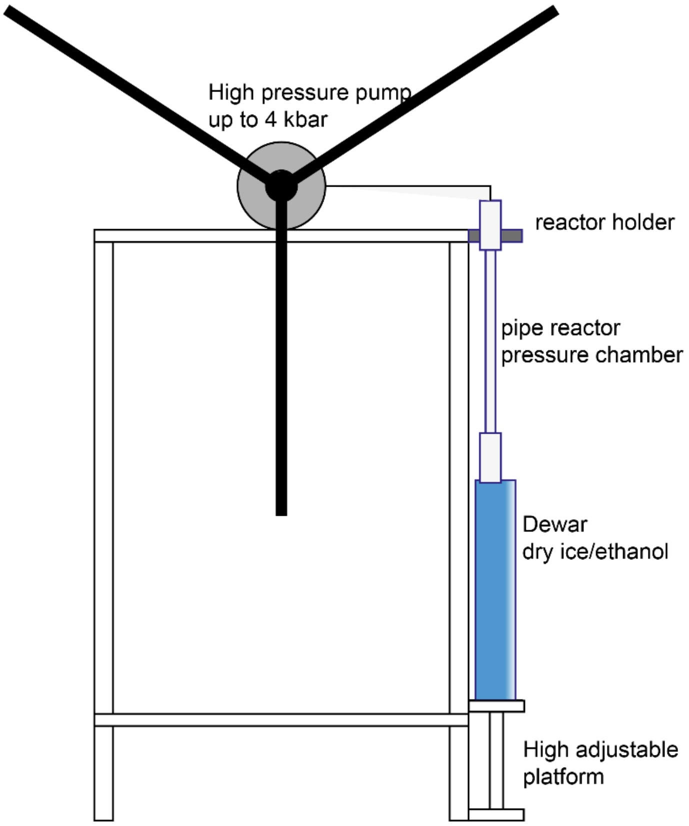

Figure 44: Schematic drawing of the high-pressure setup constructed. A 4-kbar spindle pump is connected to a microreactor by standard high-pressure tubing. A dewar vessel with a dry ice/ethanol cooling bath is used to freeze the sample. The dewar can be high adjuted by a lifting platform.

For the pressure chamber, different aspects need to be addressed. First of all, the size of the chamber needed to be determined. EPR spectrometers, depending on the resonator, need sample tubes of different sizes. In the case of the Kasanmascheff group, sample tubes between 2.8 an 1.6 mm outer diameter (OD) are used. These tubes need to fit into the pressure chamber with enough space for the pressure medium to flow around the tube and a metal collar for retrieving the tubes from the pressure chamber. Otherwise, the increased pressure would push the tube to the bottom of the chamber, in the worst case, crushing it. The pressure medium needed to be considered as well. Similar to the Hubbell group, ethanol was used as the pressuring medium. To avoid corrosive damage, a pressure chamber made of type 316 stainless steel was chosen for its specific high corrosive resistance.

Additionally, stainless steel has the advantage of being non-magnetic and not interfering with our sample recovery system (*vide infra*). Besides the inner diameter, the length of the chamber needed to be considered for the freezing process. The sample must be fully frozen before the pressure is relaxed, which is best achieved by fully submerging it into the cooling bath. The opening mechanism should not be submerged into the cooling bath to minimize possible problems due to freezing or temperature compression of the metal when opening. The EPR tubes are 15 mm long, to avoid problems, a pressure chamber of at least double the length should be chosen to account for possible errors in the sample position inside the pressure chamber, as well as keeping the pressure tubing and opening mechanism outside the dewar with the cooling bath. With consideration of material, length, and inner diameter, the MS-5 microreactor from High Pressure Equipment was chosen. An inner length of 305 mm as well as an inner diameter of 4.8 mm allow the use of both 2.8 mm OD and 1.6 mm OD EPR tubes (Figure 45). At the same time, this choice limited the applications to pressures of 4.14 kbar due to material limits and the used pressure connections. The used pressure connections are standard ¼ inch HF4 metal-to-metal connections.

A manual spindle pump from PTG (Pressure Technology Gesselschaft) was chosen as a pressure intensifier for up to 4.14 kbar pressures. All parts in contact with ethanol were modified to stainless steel to protect the system from corrosion. The application of a manual pressure intensifier allowed for easier handling and construction (Figure 44).

Submerging the whole microreactor required a large dewar vessel. To simultaneously accommodate the microreactor and dry ice, the inner height needed to be larger than the reactor length. A small diameter was chosen to avoid unnecessary heat loss. For the dewar, a KGW isotherm 7C is used with an inner diameter of 67 mm and an inner height of 350 mm, meeting both requirements.

Finally, the sample tube must withstand high pressure, and it is important to avoid mixing the sample solution with the ethanol of the pressure media. Samples containing high amounts of water need to be mixed with 25 v/v% of glycerol to avoid water expansion during freezing. Tests with lower amounts (5%, 10%, 20%) of glycerol all ended in the bursting of the sample once the pressure was lifted on the surrounding media. Another option, besides adding 25 v/v% glycerol, is the use of thick-walled EPR tubes, which can withstand the pressure of freezing water.

Standard EPR tubes used in the Kasanmascheff group have walls of either 0.25 mm for the 1.6 mm OD tubes or 0.5 mm for the 2.8 mm OD tubes. The 1.6 mm OD tubes were shown to be too fragile even with 25 v/v% of glycerol. An increase to the same 0.5 mm wall thickness as the 2.8 mm OD tubes for the 1.6 mm OD allowed pressurization. However, the remaining sample space is very small (inner diameter 0.4 mm), making sample loading difficult. A workaround is using a BAC ENDOR resonator with 2.7 mm tubes, allowing for the same ENDOR capabilities as the standard ENDOR resonator the 1.6 mm OD tubes are used for (introduced in Chapter 0).

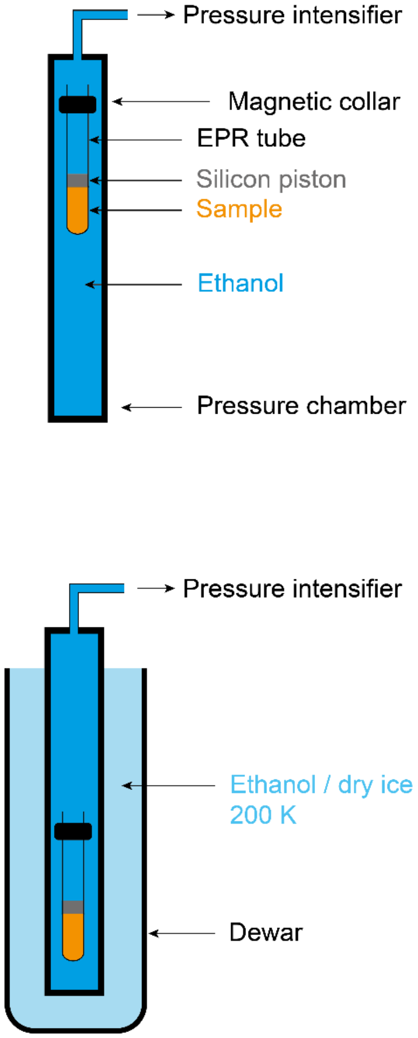

Figure 45: Schematic drawing of the sample inside the pressure chamber with a magnetic collar for sample positioning and a silicon piston to seal the sample.

Additionally, the sealing procedure was only successful in one of ten tests, leading to the postponement of the implementation of 1.6 mm OD. The tubes are sealed by inserting Sylgard 184 silicone elastomer into the sample tubes. The elastomer can be poured into form before curing; the initial idea of curing it inside empty EPR tubes to gain perfect plugs was discarded as the viscosity was too high to get them into the tubes. Instead, the elastomer is cured in 3 mm thick plates, and the EPR tube is stuck through the resulting plates, cutting circular plugs out of it. These plugs are inserted into the sample tubes and pushed down onto the solution, sealing the tube and acting as a piston upon pressurization (Figure 45). All the air below the silicone must be removed, and the piston should remain slightly flexible. The flexibility is needed to avoid cracking and possible leaks during pressurization and freezing.

A small magnetic metal collar made by the chemistry department's scientific workshop is attached to the top of the EPR tubes with sellotape. Fixation with sellotape was shown to be the most suitable approach. Additional ideas included fixation with silicone adhesive or hot glue, which requires much more preparation time, and cutting off the collar with a glass cutter after pressurization. The sellotape quickly loses adhesive strength in ethanol, easing the removal afterward while holding long enough to perform the pressurization and freezing. Additionally, the metal collars can be reused with this approach. The attached magnetic metal collar allows the sample to be moved by strong magnets from outside the pressure chamber. A pair of magnets is positioned on each side of the chamber and slide up and down, pushing the sample inside.

Test with water/glycerol filled EPR tubes confirmed the applicability of the general process. Samples can be at room temperature or on ice (~4 °C) when the silicone elastomer is inserted into the tube and pushed down with a metal rod onto the solution. To guarantee the removal of all air bubbles between the silicon piston and the solution, the piston was pushed slightly into the solution, and the supernatant on top of the piston was removed with a syringe. After attaching the metal collar, the tube is filled with ethanol before being inserted into the pressure chamber. The chamber is screwed to the remaining setup and closed with a torque wrench to guarantee a solid connection of the metal-metal connector. The sample can then be pressurized with up to 4 kbar before lifting the dewar with the cooling bath up and around the pressure chamber to freeze the sample.

To ensure all parts are thoroughly cooled down and the sample is frozen, the cooling bath remains in place for 5-10 min before releasing the pressure. The cooling bath gets lowered roughly 5 cm to allow easy opening of the pressure chamber. Afterward, the pressure chamber is kept in the dewar with the cooling bath and, for easier handling, put on a nearby table. A small dewar with liquid nitrogen is prepared. The sample is brought to the top of the pressure chamber with the help of the magnets and quickly transferred to the liquid nitrogen. Before fully submerging in liquid nitrogen, the metal collar and the ethanol must be removed above the silicon piston and around the tube. The tube is best dried with a paper towel to avoid ethanol freezing to the outside, and the ethanol inside is extracted with a syringe. The best way was to clean the tube first and stick the bottom part with the sample into liquid nitrogen before removing the collar and the ethanol inside.

While the setup is simple and the procedure is easy to perform, a couple of minor issues were determined during testing and practical use during the Fdx1 project in this thesis as well as Dr. Shari Meichsners project (PhD Thesis of Dr. Shari Meichsner). A second person is needed for error-free sample retrieval from the pressure chamber, as holding the magnets and transferring the sample is best performed by two people simultaneously. The use of only one person led to problems with sample retrieval, such as breaking the sample due to the magnets being in the wrong position. Additionally, using a manual spindle pump is disadvantageous during the freezing process. Ethanol volume decreases during the cooling process, lowering the pressure. An error of up to 80 bar can not be ruled out, as turning the spindle pump upon pressure decrease takes some time. An automatic system like a computer-controlled pressure generator would minimize the time necessary to adjust the pressure upon ethanol temperature compression, keeping the pressure constant.[135] Additionally, modifying the retrieval mechanism can help ease the use and enable reliant performance with only one user.

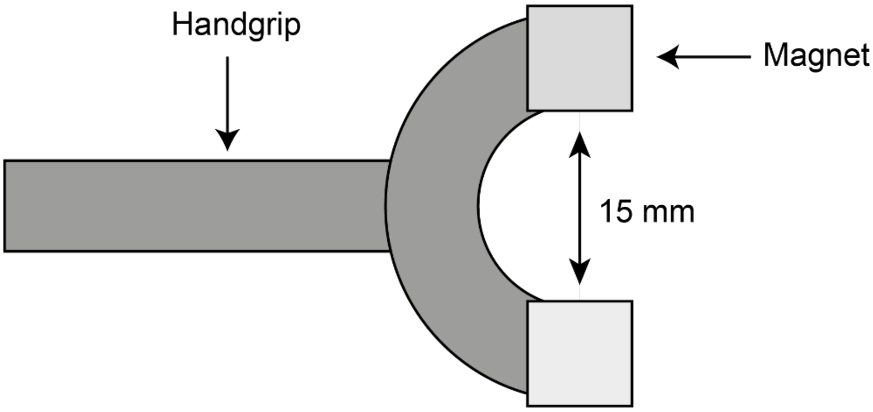

Figure 46: Possible design for a magnet holder. The magnets are attached to a wrench-like handpiece. The distance between the magnets needs to be 15 mm, as the pressure chamber OD is 14.7 mm, and a larger distance would decrease the magnetic strength.

One relatively easy modification is to incorporate the magnets into a fixed tool to hold them in place (Figure 46). Currently, the magnets are hand-held, and extreme care needs to be taken not to bruise your hands. The main problem is the round sides of the pressure chanber, allowing the magnets to slip easily, either hitting the other magnet or, in the worst case, squeezing the handler's fingers if they do not react quickly enough. Simultaneously, the magnets get very cold due to the contact with the pressure chamber. This could lead to freeze burns as the magnets are too small to be handled with gloves. While during the test and first applications, this system works, changes need to be made concerning user safety and practicality.

5.3. Results and Discussion

After the initial test of the high-pressure equipment with water samples, the possible influence of pressure on the midpoint potential of Fdx1 was investigated. Fdx1 is well studied under atmospheric conditions, and EPR and redox titration well characterized the midpoint potential of -410 mV.[203,218,220] EPR measurements of the first redox potentiometry were performed before pressurization to verify the results. If the potentiometry and analysis are performed correctly, a value close to the determined literature value is expected. To achieve reproducibility, the QT2 resonator is critically coupled for all EPR ESE experiments to ensure comparability between the signal amplitudes.

All EPR spectra show characteristic rhombic $S = \frac{1}{2}$ line shapes, while with decreasing redox potential, the signal intensity declines as the protein gets oxidized (Figure 47). All spectra show background contributions from an organic radical arising either from the added NaDT or a reaction of NaDT with one of the redox mediators, marked in Figure 47 by an asterisk. The spectrum at the potential of -0.391 V also shows signal contributions from the resonator background, predominantly manganese.

At potentials above -0.391 V, the resonator background dominates the spectra, and no [2Fe-2S] signal is distinguishable. These background contributions make analyzing the midpoint potential from the raw data difficult. Pseudomodulation of the raw data enables better simulation fitting to the overall line shape. As the simulation is set up only to include the [2Fe-2S] cluster contributions of the spectrum (Figure 48), they are normalized to the g_3 area (~1285 mT) as no background contributions are visible there.

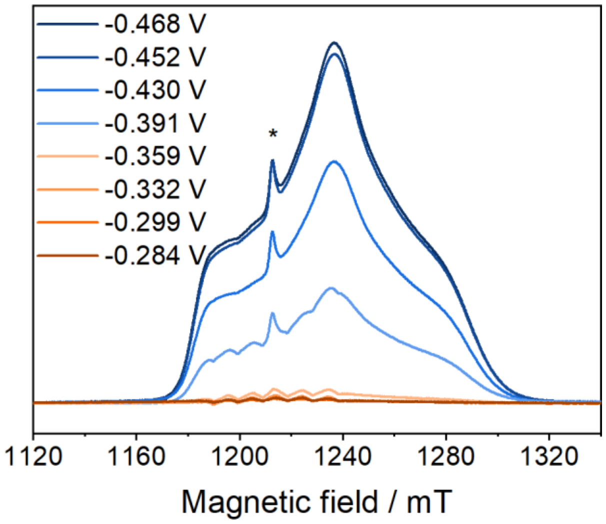

Figure 47: ESE EPR spectra of samples taken from a reductive titration with NaDT at the indicated potentials at pH 7.5 at atmospheric pressure. The asterisk marks a signal arising from an organic radical (NaDT or redox mediators).

The simulation uses the g-values [2.0552 1.9636 1.884], which match the literature values for [2Fe-2S] cluster EPR simulations (Figure 48).[218] Further analysis, double integration and a Nernst-fit, are performed on the simulation rather than the raw data, which minimizes background contributions.

Titration of NaDT into the sample solution slowly dilutes the sample, slightly lowering the overall protein concentration. To avoid influences on signal intensity, the intensity values gained by double integration of the simulations are corrected to reflect the original 200 µM protein concentration (Table 8). The resulting intensities are plotted against their respective potentials and fitted with a Nernst-Fit (Figure 49).

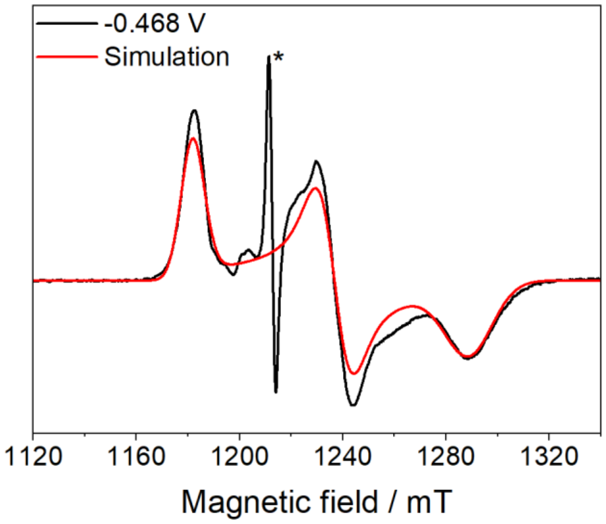

Figure 48: Pseudomodulated ESE spectrum at the potential of -0.468 V at atmospheric pressure (black) with the easyspin simulation superimposed (red). The simulation is normalized to the g_3 region (1288 mT), a line width of 9 MHz, and a g-Strain of [0.0095 0.0157 0.028] MHz together with the g-values [2.0552 1.9636 1.884]. The asterisk marks a signal arising from an organic radical (NaDT or redox mediators).

The atmospheric pressure potentiometry in Figure 49 gave a midpoint potential of -0.410 ± 0.005 V with high confidence (R^2 = 0.97), precisely the literature value. The precise reproduction of the literature value also showed that the added 25% of glycerol in these samples does not affect the midpoint potential.

This result ensures that the potentiometry and sample preparation are working correctly. As a second step, the samples were thrawn and pressurized with the equipment described above. The pressurized and refrozen samples were remeasured and analyzed again. Additionally, a second potentiometry was performed to generate a duplicate. The second potentiometry samples were not measured under atmospheric conditions as the procedure was already proven to work. Instead, the samples were pressurized directly after the potentiometry, frozen, and measured.

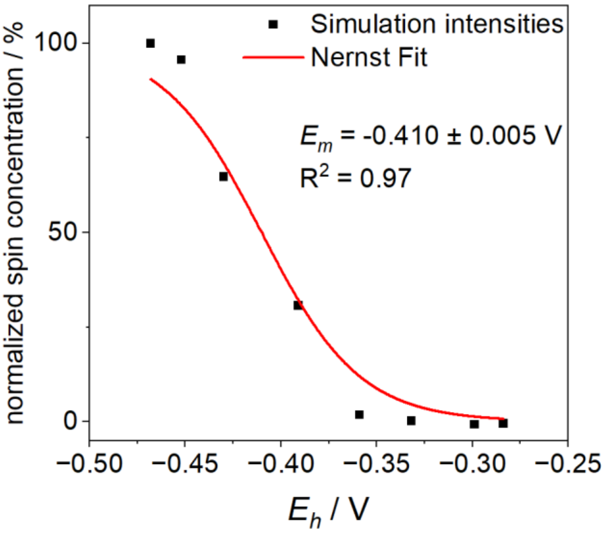

Figure 49: Nernst Fit to determine the midpoint potential of Fdx1 at atmospheric pressures. The intensities of the double-integrated simulations are plotted against their respective half-cell potentials (E_h, black) and fitted with a Nernst fit for one transferred electron (red). The resulting midpoint potential and error and the confidence of determination (R^2) are in the figure.

Pressurization was more problematic than anticipated in the first tests with water. Six of the eighteen samples of the two potentiometers broke during the process. Therefore, both potentiometers are combined for a better Nernst fit, as the start or endpoints are missing (Table 8). Both potentiometry batches show the same overall line shape under 4 kbar pressure (Figure 50A) and match the line shape and simulation of the ESE pseudo-modulated data from the atmospheric pressure measurements. The direct comparison of the two pressurized samples revealed a slight difference between 1250 mT and 1290 mT (Figure 50B). As the line shape of the Fdx1 is unperturbed, the difference most certainly results from additional unknown background contamination (Figure 50B). The extra background features could result from the pressurization procedure itself. A misplaced silicon piston might have resulted in ethanol leaking into the sample solution, leading to a possible reaction with the Fdx1. Further, suppose the silicon was not fully curred before the use in the second potentiometry. Liquid silicon might get pressed into the sample, either reacting with parts of the buffer or Fdx1 or resulting in the background signal itself. As the setup was still in the trial phase, such causes can not be ruled out. Additional tests with the silicon piston without Fdx1 and EPR measurements of uncured silicon elastomer could give insight for future projects. Pressure effects on the protein can be ruled out, as these effects are only visible in one of the two 4-kbar batches. Due to the manual pressure application, an inaccuracy of up to 80 bar is possible, but this should not significantly affect the 4-kbar pressure area.

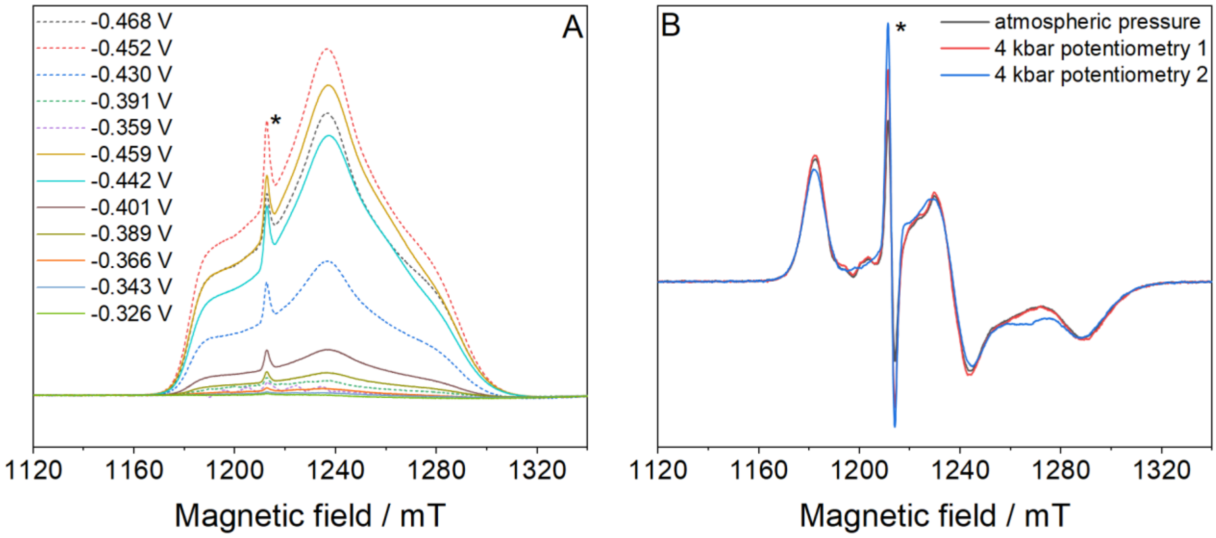

Figure 50: **A**: ESE EPR spectra of samples taken from a reductive titration with NaDT at the indicated potentials at pH 7.5 and 4 kbar. The asterisk marks a signal arising from an organic radical (NaDT or redox mediators). Two potentiometries are combined; the dashed lines belong to potentiometry 1, and the solid lines are samples from potentiometry 2. **B**: Pseudo-modulated ESE spectrum at the potential of -0.468 V of potentiometry 1 at atmospheric pressure (black) and the 4 kbar (red) as well as 4 kbar of potentiometry 2 (blue). The spectra are normalized to g_3. The asterisk marks a signal arising from an organic radical (NaDT or redox mediators).

The analysis is performed according to the first atmospheric pressure analysis on the simulated spectra, minimizing the effect of the additional background signal on the analysis. The two different potentiometry, while having slightly different background signals (Figure 50B), align when plotted together (Figure 51). The Nernst fit revealed a midpoint potential of -0.425 ± 0.007 V, shifting it by around -15 mV compared to the atmospheric pressure measurements. A shift of 15 mV is only 3 mV out of the error range of the two Nernst fits, with an R^2 value of the 4 kbar fit only being 0.88.

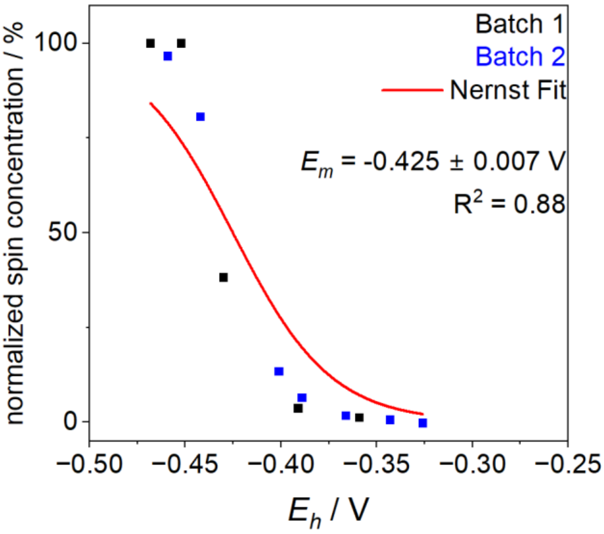

Figure 51: Nernst Fit to determine the midpoint potential of Fdx1 at 4 kbar. The intensities of the double-integrated simulations are plotted against their respective half-cell potentials (E_h, black from potentiometry 1 and blue from potentiometry 2) and fitted with a Nernst fit for one transferred electron (red). The resulting midpoint potential and error and the confidence of determination (R^2) are given inside the figure.

The low confidence value of the fit indicates a larger error than the fit itself. One reason is the set number of transferred electrons in the Nernst equation. Only one electron can be transferred to reduce a [2Fe-2S] cluster. The transfer of more electrons would result in either the cluster not being EPR active anymore or the formation of an organic radical in the surrounding coordination spheres. Both are not observed in the ESE spectra.

A second approach for midpoint potential determination, a semilog plot, is performed to assess if the Nernst Fit gave a wrong result. The linear fit of the semilog plot provides the midpoint potential as the y-axis intercept (Figure 52B). Here, the linear fit gave the same midpoint potential of -0.424 ± 0.007 V as the Nernst fit. The gradient of the slope m can be used to determine the transferred electrons *n* with the Faraday constant *F*:

$$m = 2.3026\frac{RT}{Fn}. \tag{5.1}$$

It can be simplified to $n = 0.0592\frac{mV}{m}$, resulting in 1.8 transferred electrons. As mentioned before, the number of transferred electrons for Fdx1 can not exceed one. Thereby, the number of transferred electrons indicates that the Nernst fit and ESE spectra give a false result.

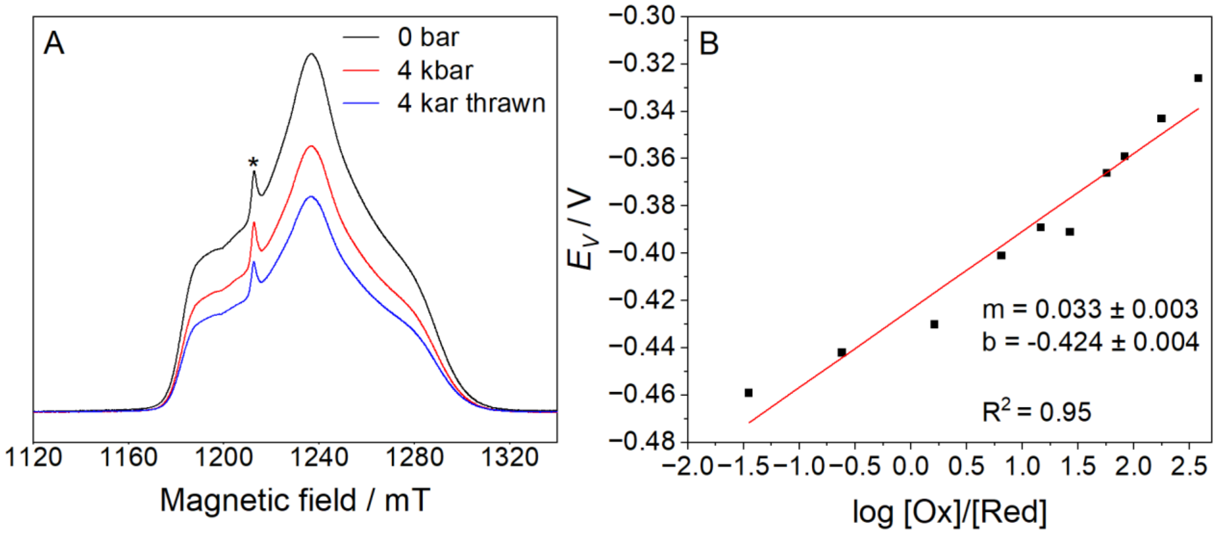

Figure 52: **A**: ESE EPR spectra of the -0.468 V potential taken from a reductive titration with NaDT at pH 7.5. The same sample was measured before and after the pressurization to 4 kbar (black and red, respectively). Additionally the sample was thrawn after pressurization and refrozen at atmospheric pressure (blue). The asterisk marks a signal arising from an organic radical (NaDT or redox mediators). **B**: Semilog plot of the two 4 kbar potentiometry. Linear fit of the potentiometry points (red) with gradient (m) and y-axis intercept (b) are given inside the figure.

Figure 52A shows that during the pressurization of the sample, parts of the paramagnetic species vanish. A change in ESE line shape was anticipated through water penetration or changes in the first or second coordination sphere. As a change in line shape can not be observed in both 4 kbar ESE measurement sets, besides the background change (Figure 50B), the electronic structure of the [2Fe-2S] cluster is not influenced by pressure. At the same time, the diminishing of the ESE intensity indicates that some proteins got oxidated during pressurization and following thrawing. If the change in intensity was a pure reversible pressure effect, the intensity should return to the original level after thrawing. This does not happen, and the intensity drops even further, indicating irreversible oxidation, most probably due to denaturation or other destructive processes (Figure 52A).

This results in an overall problem for the sample analysis. Oxidation of some [2Fe-2S] clusters changes the sample's potential. The potential is not determined again after the pressurization, which leads to the assignment of wrong potentials to intensity values. These changes can not be included in the analysis, as remeasuring the potential in frozen form after pressurization is not currently possible. Overall, this results in an incorrect midpoint potential determination.

5.4. Summary and Outlook

The initial brief to build and establish a high-pressure EPR setup to investigate high-energy protein configurations was achieved. The setup showed to be working with a couple of minor flaws, which should be removed over time. Overall, applying high pressure at room temperature and freezing the sample under pressure to trap it inside the high-pressure configuration works with this basic, less controlled setup, compared to using a more automatic setup reported by the Hubbell group. Here, the critical point remains to be the retrieval of the sample out of the cooled pressure chamber. The discussed magnet holder system for easier sample retrieval might already fix the issue. Nonetheless, it would help with solo use and safer handling of the cold pressure chamber. Overall, the high-pressure setup now allows for reliable sample pressurization for all types of low-temperature EPR measurements in the range of 0 – 4 kbar.

Using this approach for tuning the midpoint potential of Fdx1 with high pressure was shown to be difficult. The general potentiometry reproduced the literature value perfectly while the high-pressure application worked, and the effects were visible; the analysis revealed some significant flaws. Firstly, a better retrieval system for the EPR sample would, in this case, have helped to avoid the loss of so many data points (six broken tubes during pressurization or retrieval). Additionally, a difference in line shape due to different pressure effects was anticipated, while the results showed a reduction of overall signal intensity with no line shape influences. The resulting conclusion of oxidation of some [2Fe-2S] clusters and, thereby, the change in potential inside these samples was overseen during project planning. As the potential can not be determined after pressurization in this setup, the graphic application and analysis use misleading potentials for the samples.

As an effect of pressure on the samples is observed, Fdx1 is still a promising protein to investigate under pressure. A pressure influence on the midpoint potential can also not be ruled out; the pressure setup would need adjustment. A setup that pressurized the sample inside the resonator while the potential can be determined would be ideal but technically nearly impossible to construct as electrodes must be fitted into a 1.8 mm inner diameter EPR tube. Additionally, the whole setup would need to allow for cooling, as [Fe-S] clusters are too fast relaxing to measure at room temperature. Midpoint potential determination via other methods like UV/Vis is more approachable[221,222] as high-pressure equipment is already in use and only needs minor modifications, if any.[223,224]

6. General purpose 34 GHz TE_{011} resonator

In EPR spectroscopy, one of the essential parts of the EPR spectrometer is the microwave resonator. The resonator holds the sample during the experiment, concentrating the microwaves onto the sample to enhance the signal sensitivity.[225] Additionally, the resonator type determines the sensitivity and time resolution.[225] Over the years, many different resonators have been designed by working groups with special purposes,[226–229] and a wide variety is commercially available from Bruker or Bridge12. Different applications have optimal working parameters in different resonator cavities.[225] For example, 9.4 GHz CW EPR resonators are mainly based on rectangular TE_{102} cavities. They have a high quality factor (parameter describing resonance behavior), a reasonable filling factor (how much of the resonator is filled with sample), and low sensitivity to dielectric losses in samples. The large sample opening of these resonators allows them to be easily used with cold finger dewars for low-temperature measurements.[225] The low microwave bandwidth and the frequent lag of MW frequency tuning mechanisms make these resonators unsuitable for pulse EPR and higher frequencies.

9.4 GHz EPR sources, mostly used for CW EPR, are often tunable on quite large frequency scales, while 34 GHz and higher frequencies only have a narrow frequency source. Cylindrical TE_{011} cavity resonators are used for these applications. Compared to TE_{102} cavities, these types are frequency tunable by moving one of the resonator plungers (Figure 53a (3)/(5)) and are easier to manufacture than scaled down to 34 GHz TE_{102} cavities.[225] Alternatively, depending on the measurement method, other specialized resonators can be used. In the Kasanmascheff lab, two commercially available Bruker resonators are mainly used. The ER5106-QT2 resonator for double electron-electron resonance spectroscopy (DEER / PELDOR) has a TE_{012} cylindrical cavity. In contrast, the ER5107D2 resonator is a dielectric resonator.

Here, the main focus lies on a 34 GHz pulse EPR TE_{011} resonator (BAC) for ESE, ENDOR, and DEER, developed by Edward Reijerse et al.[225] in the early 1990s and recently modified by the group of Prof. Nick Cox at the Australian National University to allow bandwidth tunability for general-purpose measurements (Figure 53). The resonator features a cylindrical TE_{011} cavity with a 2.8 mm sample opening and four 0.8 mm silver posts acting as ENDOR coils in pseudo-Helmholz geometry, making the resonator robust and immune against mechanical vibrations.[225] Compared to the dielectric ER5107D2 Bruker ENDOR resonator (D2) with its 1.6 mm sample opening, it can fit larger samples also used in our 9.5 GHz MD5 resonator as well as the specialized ER5106-QT2 34 GHz resonator. Additionally, the movable top plunger of the resonator allows frequency tuning in a range of ±2 GHz (Figure 53a (3)).

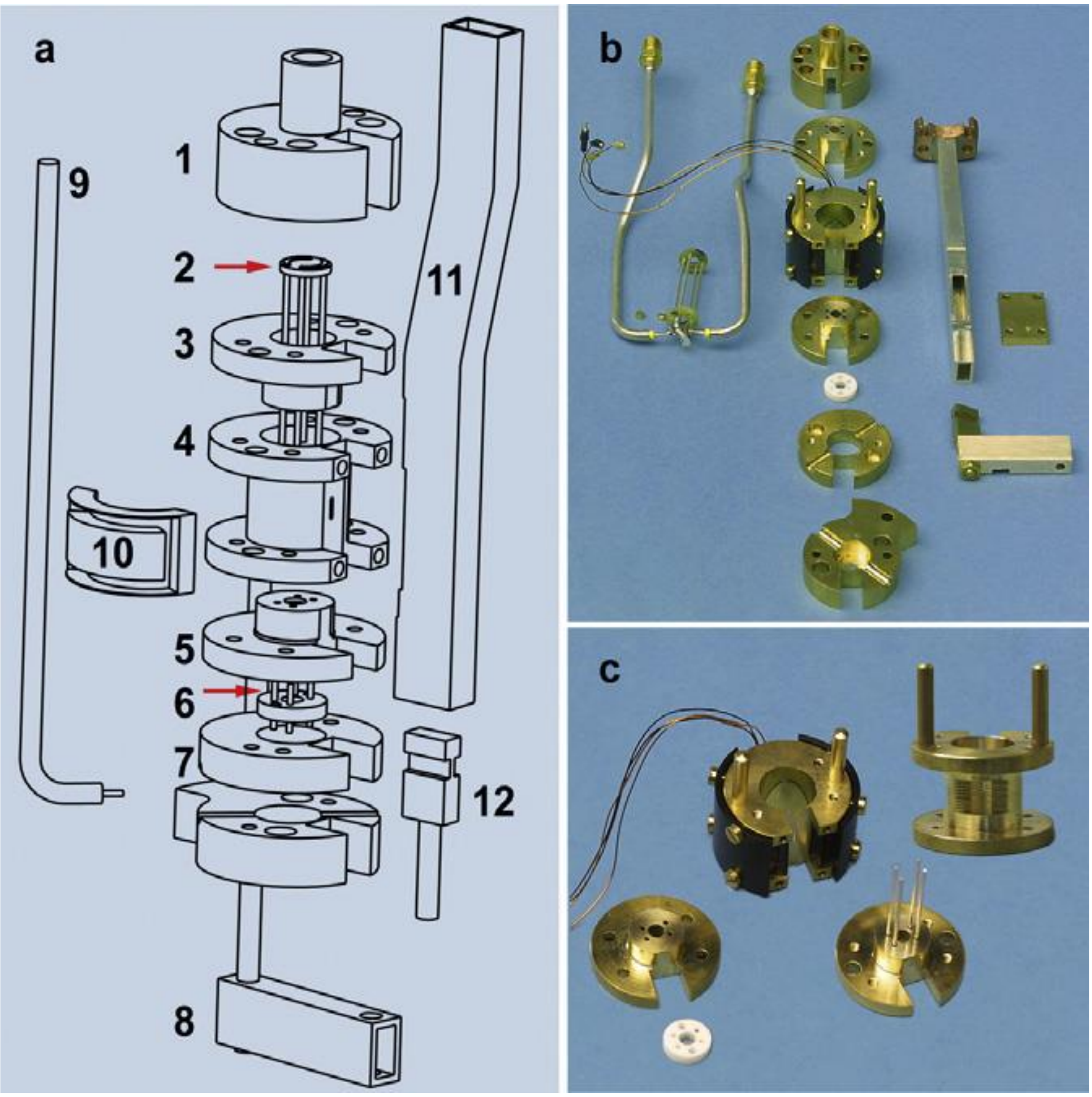

Figure 53: (**a**) Exploded view of the Q-band TE$_{011}$ ENDOR resonator probe head; (1) Upper cover; (2) ENDOR posts; (3) upper (movable) plunger; (4) resonator body with iris on the right (flattened) side; (5) lower (fixed) plunger; (6) RF contact plate; (7) coax clamps; (8) drive bar for sliding short; (9) RF coax line; (10) modulation coil body; (11) coupling waveguide; (12) sliding short. (**b**) Photo of the disassembled resonator showing the parts in panel (**a**). The input and output coax lines are connected to the ENDOR coil, and the modulation coils are mounted to the resonator body. (**c**) Photo of the resonator body with modulation coil attached (using the black caps). The upper and lower plungers also detail the silver posts making up the RF coil and the MACOR contact plate (white). In addition, a ‘‘naked’’ resonator body with slits (12 cuts of 0.3 mm, 0.5 mm apart, giving a 3 mm wide 60% optical access) is shown. Figure taken from Ref. [225] under the RightsLink license number 5942931333288.

Figure 53 shows a schematic drawing of the resonator body and pictures of the individual parts. Table 10 lists the most important technical parameters.

The original version featured a 3 mm sample opening, which Prof. Nick Cox reduced for us to 2.8 mm. Reijerse et al. 's publication provides a detailed resonator explanation.[225] Therefore, this thesis does not go into more detail, as no additional changes to the resonator were made. The original design was intended for CW and ENDOR measurements and thus has limited bandwidth. The work by Judd et al. modified the resonator coupling mechanism with dielectric plates,[230] which allows overcoupling to achieve bandwidths up to 100 MHz, overcoming the original design's limited bandwidth. Further, plans to use sapphire crystal to achieve bandwidths of up to 1 GHz in the overcoupled mode are currently being tested by Martyna Judd (personal communication). This would allow the BAC resonator to be an actual all-purpose resonator with a low bandwidth critical coupled mode for CW EPR, pulse EPR, and pulse ENDOR and a very high bandwidth overcoupled mode for DEER measurements. The current version discussed here and used by the working group of Prof. Kasanmascheff lacks this feature and has a fixed bandwidth of 20 MHz, which can not be tuned.

Table 10: Technical parameters of the TE_{011} resonator version produced by Prof. Nick Cox.[225]

MW frequency	32 – 36 GHz	RF frequency	1 – 400 MHz
Cavity diameter	11 mm	ENDOR geometry	2.7 x 4.6 mm
Modulation coil	30 turns	Sample height	9 mm
B_{mod} (100 kHz)	1 mT	Sample tube diameter	2.7 mm

6.1. TE_{011} cavity resonator function tests

A good working and reliable sample is needed to test the resonator's function. The original paper used Standard Bruker samples, such as BDPA and DPPH, for room temperature performance tests.[225] A performance gain compared to the D2 with our research samples was much more interesting in this case, as BDPA always gives good to excellent results if correctly measured. Here, BDPA is only used for basic room temperature checks of general function and RF pulse nutation experiments.

For a direct comparison of the Bruker D2 resonator with the BAC resonator, RNR class Ia Y_{122}• was chosen. The RNR class Ia Y_{122}• is well-studied and is a significant research topic in our group by multiple PhD students.[4] Therefore, four samples were prepared: 200 µM protein concentration with 5 % glycerol and 10 µM with 5 % glycerol in 2.7 mm and 1.6 mm tubes for the BAC and D2 resonator, respectively.

For BDPA, a 1.6 mm 1% BDPA in polystyrene sample is used. To enable measurements in the BAC resonator, the sample tube was inserted into a 2.7 mm BAC resonator tube (inner diameter 1.8 mm) to have a sufficient filling factor. Without the 2.7 mm outer tube, the EPR tuning dip lay above 36 GHz, outside of the reach of the spectrometer MW source and BAC tuning capabilities.

A direct comparison of the ESE data of both resonators revealed a slight shift in g-value position for the BAC resonator (Figure 54A). As such an effect was not observed with the later RNR samples (Figure 55), the best explanation is the difference in tuning and the necessity of inserting it into another tube. As for tuning, the frequency tuning capabilities of the resonator were brought to their limit, possibly introducing frequency inhomogeneity and leading to a shift in peak position.

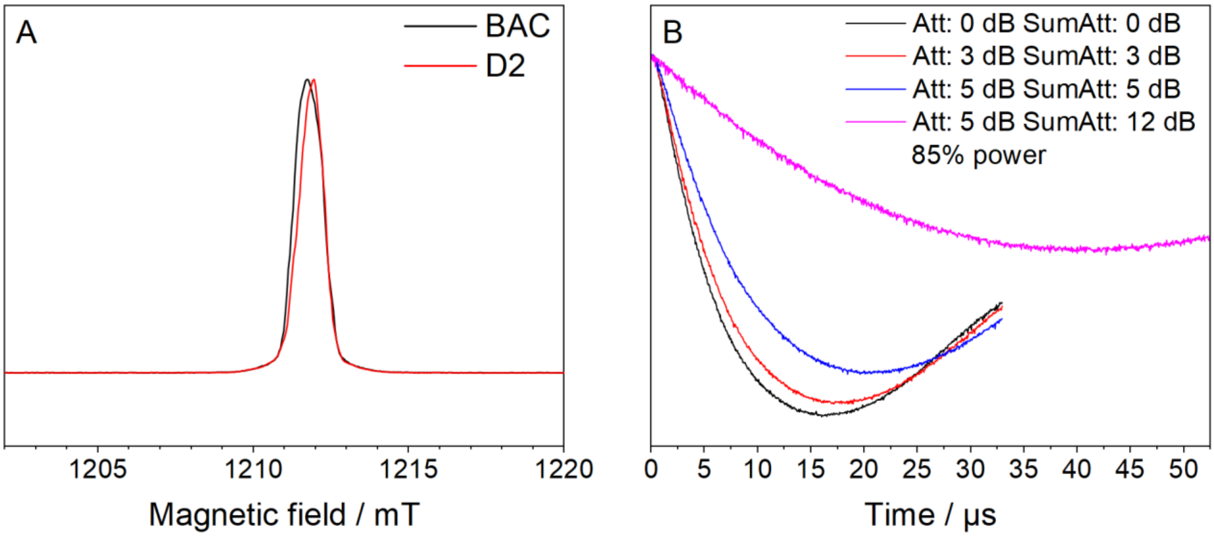

Figure 54: BDPA room temperature test measurements in BAC and D2 resonator. A: Pulse field sweep measurements of 1% BDPA in polystyrene in BAC (black) and D2 (red). The spectra are frequency and intensity normalized. B: RF nutation experiments at 51.6 MHz (^{1}H matrix line, 100% RF amplifier power) following the Mims ENDOR sequence at different power settings for the RF source indicated in the figure (Att: Attenuation; SumAtt: Sum Attenuation). For the pink trace, the power of the RF amplifier was limited to 85%, which is equal to the power used for D2 ENDOR experiments. Additionally, the trace was extended to allow the observation of longer pulse lengths.

Besides the slight shift, both resonators showed the identical expected line shape. The frequency and coupling tuning of the BAC resonator worked perfectly. A small problem arose from the manufacturing procedure, as the ordered 2.8 mm sample opening was too precise. Our 2.8 mm tubes for use in the MD5 and QT2 resonators have a 0.1 mm error margin, which could result in stuck or broken samples upon insertion into the resonator. Therefore, new tubes with a slightly smaller 2.7 mm OD were ordered and used from here.

For the RF pulse length nutation experiments, the field was held fixed at the maximum intensity, and the RF frequency was set to the frequency maximum of the ^{1}H ENDOR matrix line (measurements not shown). For the D2 resonator, Dr. Yury Kutin performed the RF nutation in 2018 during the implementation of the resonator in our lab. The power settings optimal for a ^{1}H ENDOR in the D2: pulse length: 17 µs, RF channel attenuation: 5 dB with 12 dB Sum Attenuation at a power level of 85 % set on the RF amplifier (730 mV peak-to-peak power). Higher powers resulting in shorter pulse lengths are achievable but have been shown to melt the RF coils of the D2 resonator. As previous measurements were done with a 2500 W amplifier in the BAC resonator,[225] the RF amplifier was set to a power level of 100% (600 W) as no destruction of the coils was anticipated. Figure 54B shows the RF nutation curves at different power settings for the BAC resonator. A minimum pulse length of 14.5 µs was achieved at full power for a ^{1}H spin transition. The same 17 µs as the D2 resonator are optimal when the attenuation is set to 3 dB for both attenuators. At the same power settings optimal for the D2, the BAC resonator can only achieve an RF pulse length of roughly 40 µs (pink trace, Figure 54B). This indicates a much lower RF transition efficiency than the D2 resonator due to possibly a smaller area of homogenous RF field or a less homogenous RF field. Both factors would explain a higher power need for the same pulse length.

For lab applications, this lower RF power efficiency is not crucial as the used RF amplifier has the power reserves to achieve the same pulse length as D2. Additionally, longer RF pulse lengths are often desired as the ENDOR resolution increases for longer pulse lengths (as shown in 4.1). Very short RF pulse lengths, like the 7 µs with a 2500 W amplifier by Edward Reijerse et al.,[225] are only helpful for couplings above 10 MHz.

The strength of the BAC resonator is the large sample opening, which allows for higher spin amounts. Using high-concentration samples with standard field sweep settings (high number of scans or high number of shots per point) showed no apparent difference between BAC and D2 (Figure 55A). Both resonators have excellent performance for high concentrations; the advantage of BAC only comes into focus at low concentrations or very short measurements.

Figure 55B incorporates the same RNR Y_{122}• sample but with only 10 µM measured with 1 shot per point for one scan. It shows much lower SNR for D2 (18.5) than BAC (64.5). The recorded 3.47 times improvement in SNR between the BAC and the D2 resonator for the RNR samples matches the improvement of 3.5 times reported in the literature.[225]

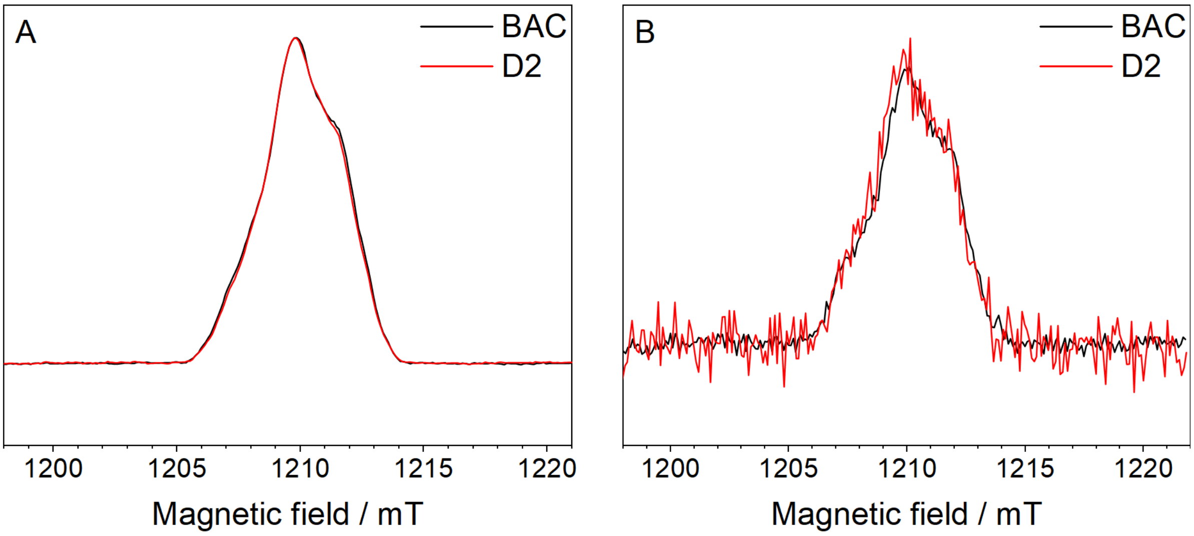

Figure 55: Pulse field sweep measurements in D2 (red) and BAC (black) resonator of RNR Y_{122}•. A: 1 scan at 100 shots per point measurements of RNR Y_{122}• (200 µM) at 10 K in D2 (1.6 mm OD tube) and BAC (2.7 mm OD tube) resonator. B: 1 scan at 1 shot per point measurements of RNR Y_{122}• (10 µM) at 10 K in D2 and BAC resonator.

While the desired result was achieved, a spectrometer artifact was discovered during the test measurements. A continuous oscillation was visible in the non-signal areas (background), with a strong three-peak repetitive up and down in the baseline (Figure S14). Currently, the origin of the oscillation is unknown. Similar oscillations were visible during the research stay at the ANU. They were discovered to originate from the interference of other electronic devices and vibrations in the system (termed earth loop). A solution was to dampen the cryo connections to the Helium tank and the introduction of 50 Hz low-pass filters into the primary power source. As our Helium tank is connected to the cryo system by flexible silicone tubing, the influence of mechanical vibrations can be excluded. The introduction of electronic noise through other electronic devices should not be excluded. Since the remodeling of the EPR lab at the TU Dortmund, two EPR spectrometers are connected to the same central power line of the building. As the connection is hard-wired, no easy solution is possible at this point. Introducing a low-pass electronic filter would require some modifications to the power line. As the oscillations can not be removed currently, the SNR values of BAC and D2 must be seen critically. Nevertheless, the oscillation looks nearly identical in both resonators and seems systematic (Figure S14), resulting in a relative SNR value for the two resonators. An absolute SNR value for comparison is not interesting in many cases as it is highly system-dependent. Therefore, the oscillation can be neglected for the SNR comparison.

Besides the RF pulse length, the performance regarding SNR should also be investigated for ENDOR measurements. Like pulse-field sweep experiments, the higher sample amount and spin concentration in the resonator's active window should increase the ENDOR's SNR. The Davies ENDOR measurements were performed at the g_y position ($g = 2.008$, 1212 mT in Figure 55A) of the spectrum for good comparability to the work of Dr. Shari Meichsner (PhD thesis chapter 3.3.3) and ease of recording (Figure 56). Both resonators show identical line shapes with no artifacts and are similar to measurements done by Dr. Shari Meichsner. For the best SNR comparison, only ten scans were performed to ensure sufficient signal visibility. Lower scan numbers had the problem, especially under five scans for D2, that the ^{1}H signal was not clearly identifiable in the spectrum. In this case, the gained SNR result depends on the amount of scans done.

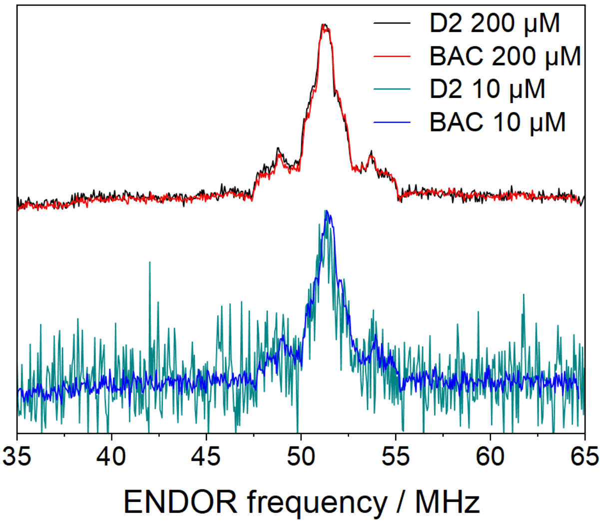

Figure 56: Davies ENDOR measurements of RNR Y_{122}• with different resonators and concentrations indicated inside the figure. All measurements are done at 10 K with a 200 ns inversion pulse, 17 µs Rf pulse, 20 ns π pulse, and a 450 ns τ for 10 scans.

For ten scans, the BAC resonator has roughly 1.4 times better SNR for 200 µM samples. For low concentrations, the increase in SNR is even more significant; for 10 µM samples, it increases by 4.9 times.

Here, the low sample concentration is more meaningful. As to get the exact measurement parameters of the D2 resonator, the BAC resonator needed to be strongly undercoupled for the 200 µM samples, limiting power output drastically, as otherwise strong ring-down effects were visible. Currently, the BAC resonator can only be critically coupled or undercoupled as the Iris is set to a fixed bandwidth of 20 MHz, and the coupling mechanism is not meant for overcoupled measurements. Modifications to the coupling mechanism mentioned in Judd et al. would be necessary to enable overcoupling and larger bandwidth.[230]

During the low-temperature test, it was evident that the BAC resonator lacked adequate insulation. At moderate humidity levels of around 45%, significant condensation developed at the probe head, affecting both the electronic sockets for the temperature sensor and the RF connections. After just four days of use at low temperatures, the connectors for the tuning mechanism began to rust.

After consulting with Anton Savitsky, one of the authors involved in further developing the BAC resonator design, it became clear that the waveguide installed between the resonator and the probe head was made from the wrong material.[230] The solid, thick-walled copper waveguide, which has high thermal conductivity, facilitates heat transfer toward the probe head. In contrast, all other components connecting the resonator and probe head are made from a special resin—similar to what Bruker uses for its resonators—with very low thermal conductivity.

The waveguide needs to be replaced with insulated stainless steel to achieve the desired insulation effect.

6.2. Conclusion and Outlook

The TE_{011} cavity resonator demonstrated significant advantages in terms of SNR and the analysis of low-concentration samples compared to the D2 resonator. Although the RF efficiency is considerably lower, the high-power RF amplifier at TU Dortmund adequately offsets this inefficiency. Moreover, the larger sample volume provides advantages for analyzing very low-concentration samples. At the same time, it allows the same EPR tubes to be utilized in other resonators. This feature minimizes the amount of sample required for experiments conducted at multiple frequencies and with various methods, as only one EPR tube needs to be filled. Additionally, it reduces the risk of errors that may occur due to different sample preparations. Finally, for the permanent use of the BAC resonator at low temperatures, the waveguide in the probe head will need to be replaced with a stainless steel version.

Appendix

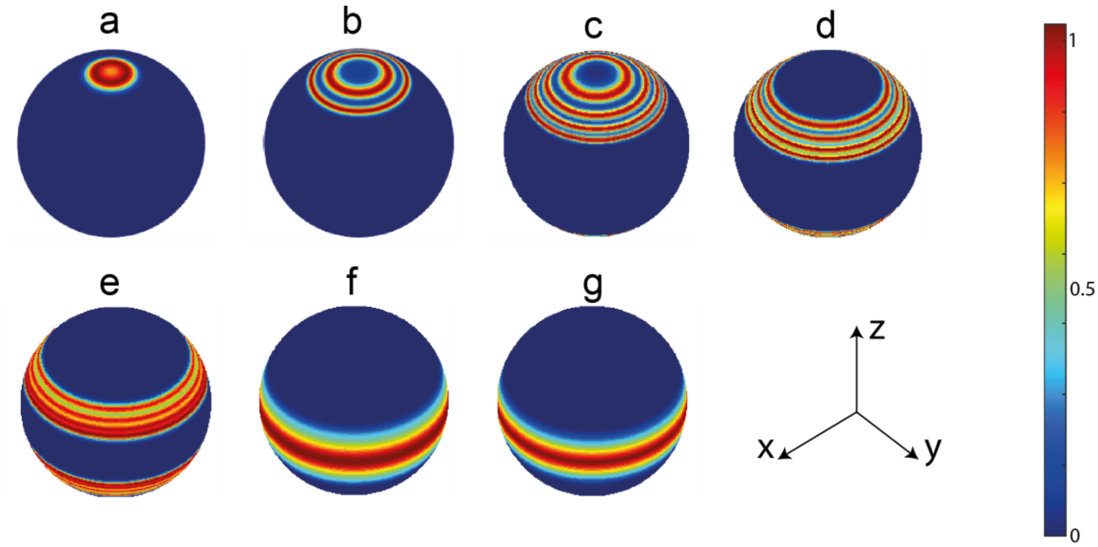

Figure S1: g-tensor orientations excited at the field positions where ^{19}F Mims ENDOR spectra were collected. The spheres were generated using the orisel function of the EasySpin toolbox. The simulation parameters are based on the **GQ3** Mims parameters from Table 1. Since the perpendicular component of the Cu^{2+} hf tensor is not resolved in EPR, a somewhat arbitrary value of 50 MHz was used for the illustration. Due to a strong ^{19}F ENDOR contribution from the free/non-specifically bound Cu(II) at position **a** for **GQ2^{C}/GQ4^{C}**, the ENDOR spectra for these species shown in this work were collected ~4 mT higher than the precise position **a**.

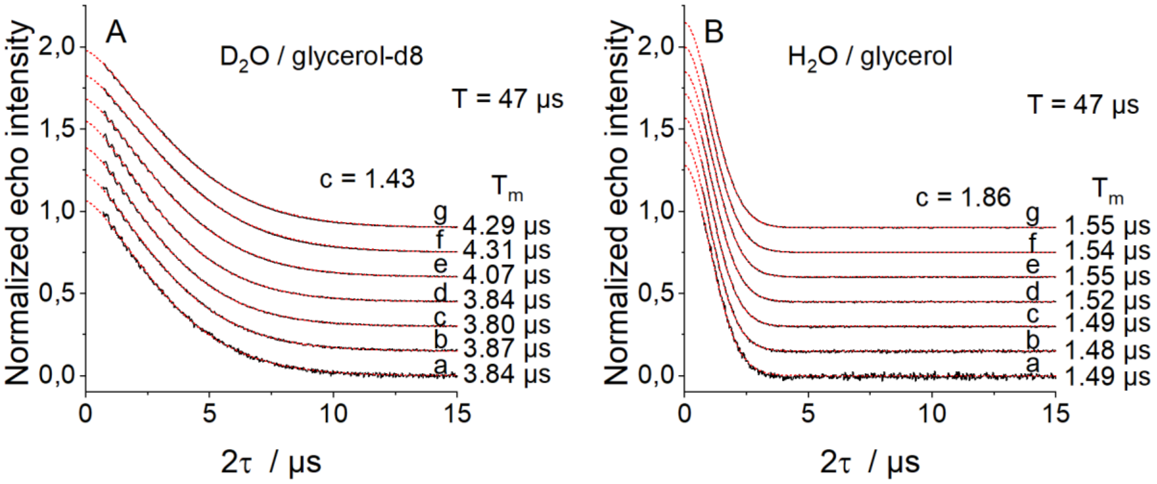

Figure S2: T_m measurements using the simulated echo sequence (T = 47 µs) of **GQ3** (black) at all field positions indicated in **Figure 19** fitted with a stretched exponential decay function (Eq. 2.19, red, c is indicated in the figure) the resulting T_m times are listed behind the graphs. **A**: Measurements were done in deuterated solvent. **B**: Measurements were done in none deuterated solvent. Deuteration of the solvent leads to a roughly three-time increasein T_m.

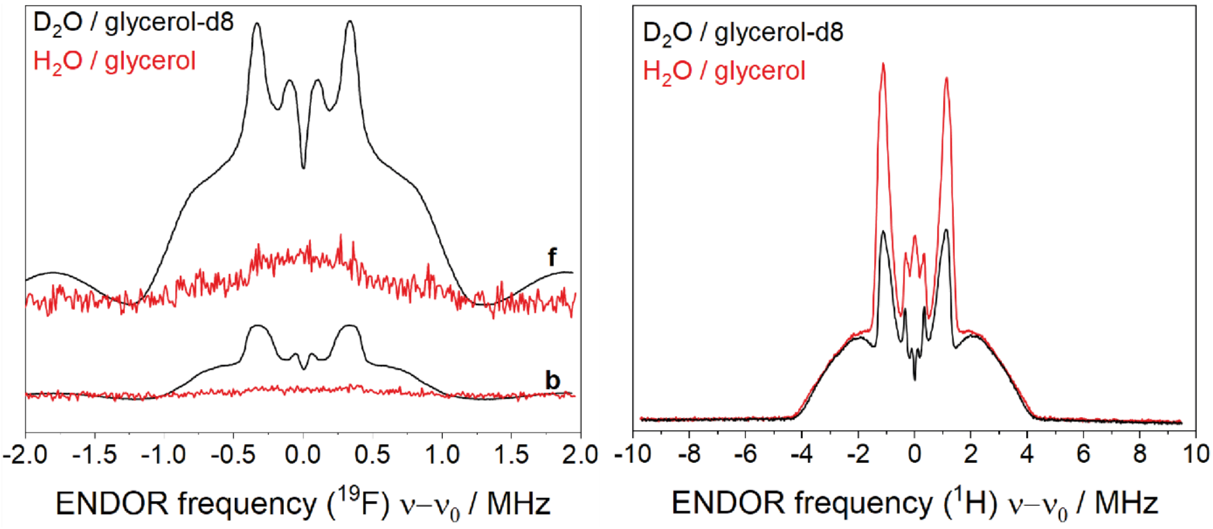

Figure S3: ENDOR spectra of **GQ3** in deuterated solvent (D_2O / glycerol-d8, black) and none deuterated solvent (H_2O / glycerol, red). **Left**: Mims ENDOR of **GQ3** at the positions indicated in **Figure 19** and optimized parameters (RF pulse: 45 µs, τ: **Table 2**). **Right**: Davies ENDOR of **GQ3** at position **f**. Parameters: 200 ns inversion pulse, τ: 450 ns, and RF pulse length: 17 µs.

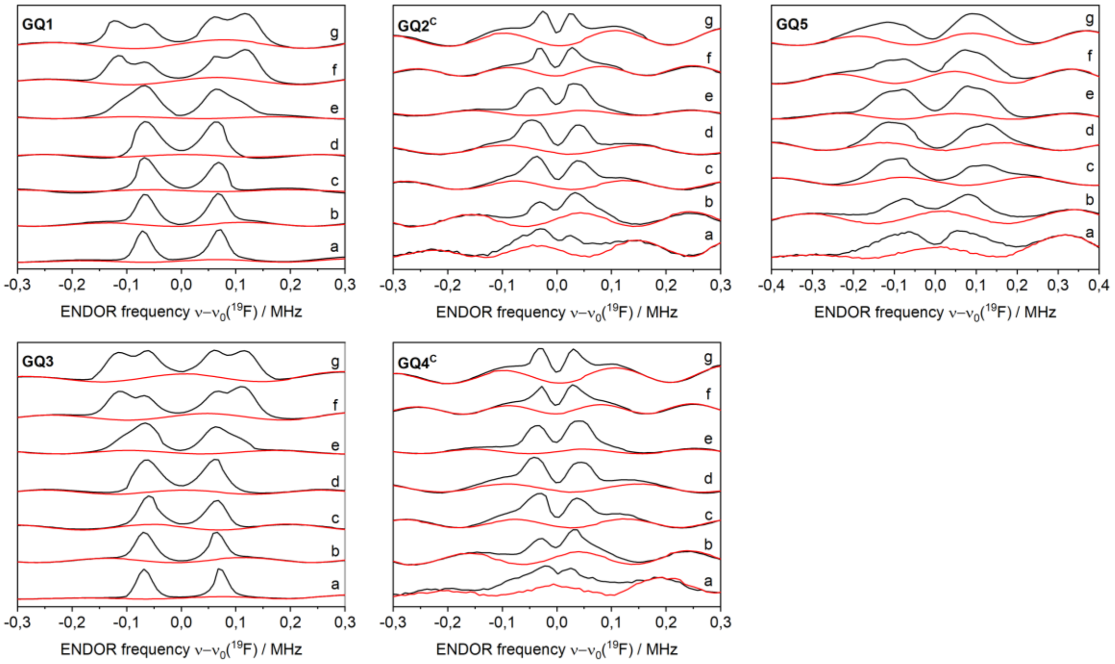

Figure S4: Normalized ^{19}F ENDOR spectra of **GQ1**–**GQ5** (black traces), overlaid with scaled ^{1}H background spectra of **GQ0** (red traces). The τ values for every position and sample are given in **Table 2**. The traces are shifted vertically for clarity.

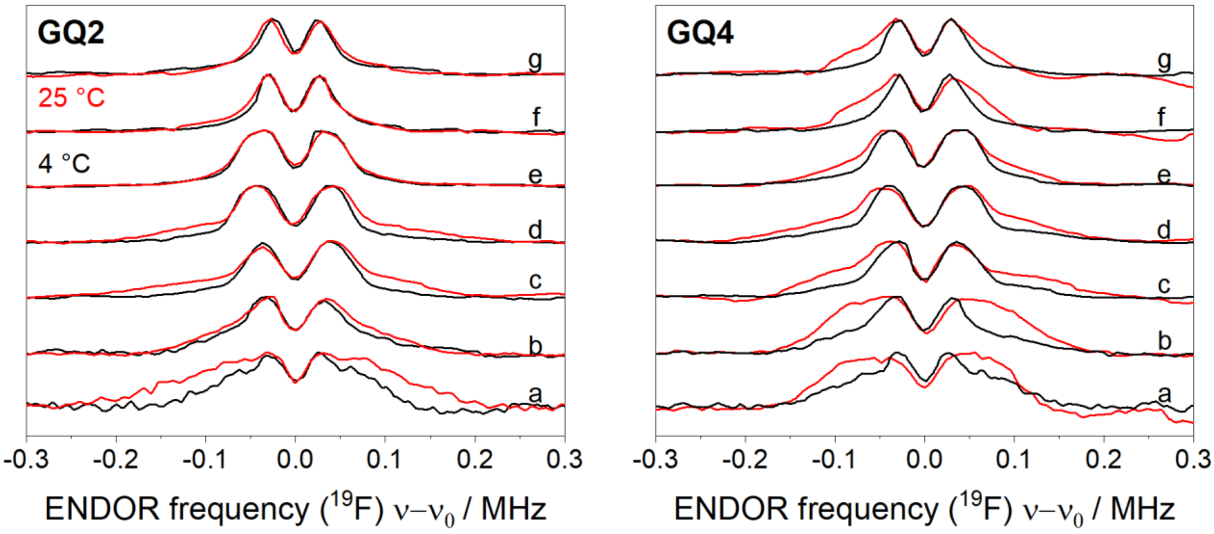

Figure S5: Background-subtracted ^{19}F ENDOR spectra of **GQ2** (left) and **GQ4** (right) at two different temperatures of production, 4 °C (black) and 25 °C (red). The accumulation time was between 4 and 12 hours, depending on the field position. τ value for each position and sample can be found in **Table 2**. The traces are shifted vertically for clarification.

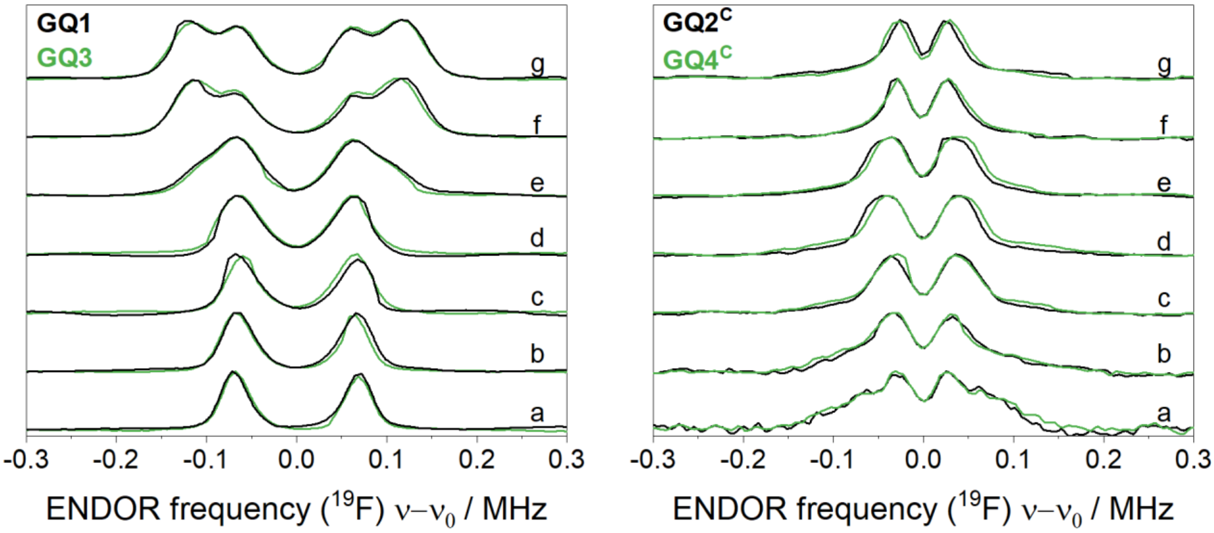

Figure S6: Comparison of background-corrected ^{19}F ENDOR spectra of **GQ1** (black) and **GQ3** (green) on the left and **GQ2^{C}** (black) and **GQ4^{C}** (green) on the right. The τ values for each sample and field position can be found in Table 2**.**

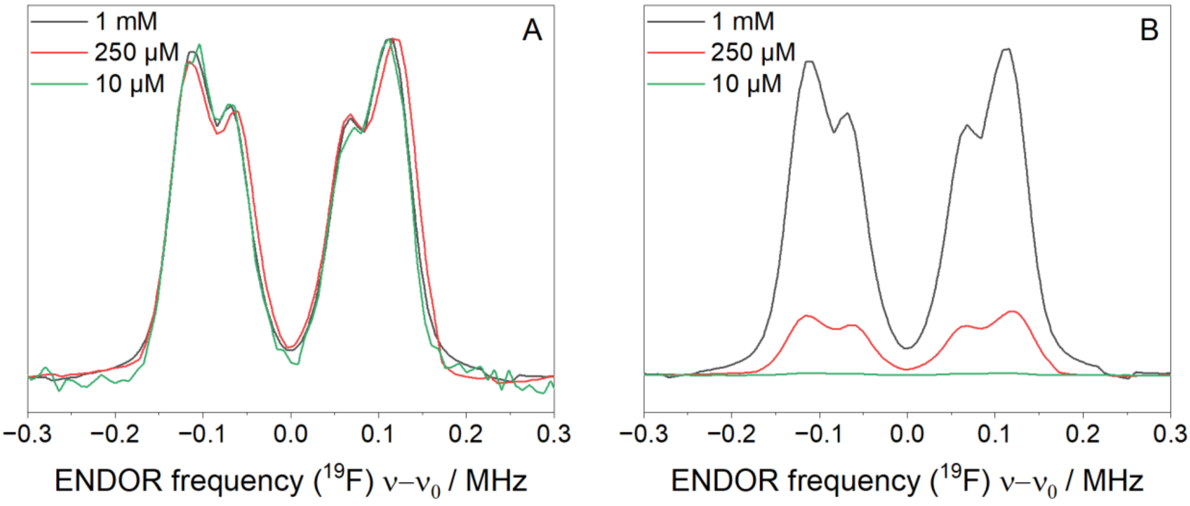

Figure S7: Concentration tests of **GQ3** ^{19}F ENDOR at position **f** to determine the minimal concentration for ^{19}F measurements. All spectra are background subtracted and recorded with the identical optimization; the accumulation of scans is 5500 for 1 mM and 250 µM, and 6160 for 10 µM. **A**: Normalized spectra to a maximum of 1 for direct comparison. **B**: Spectra without normalization, all are optimized identically.

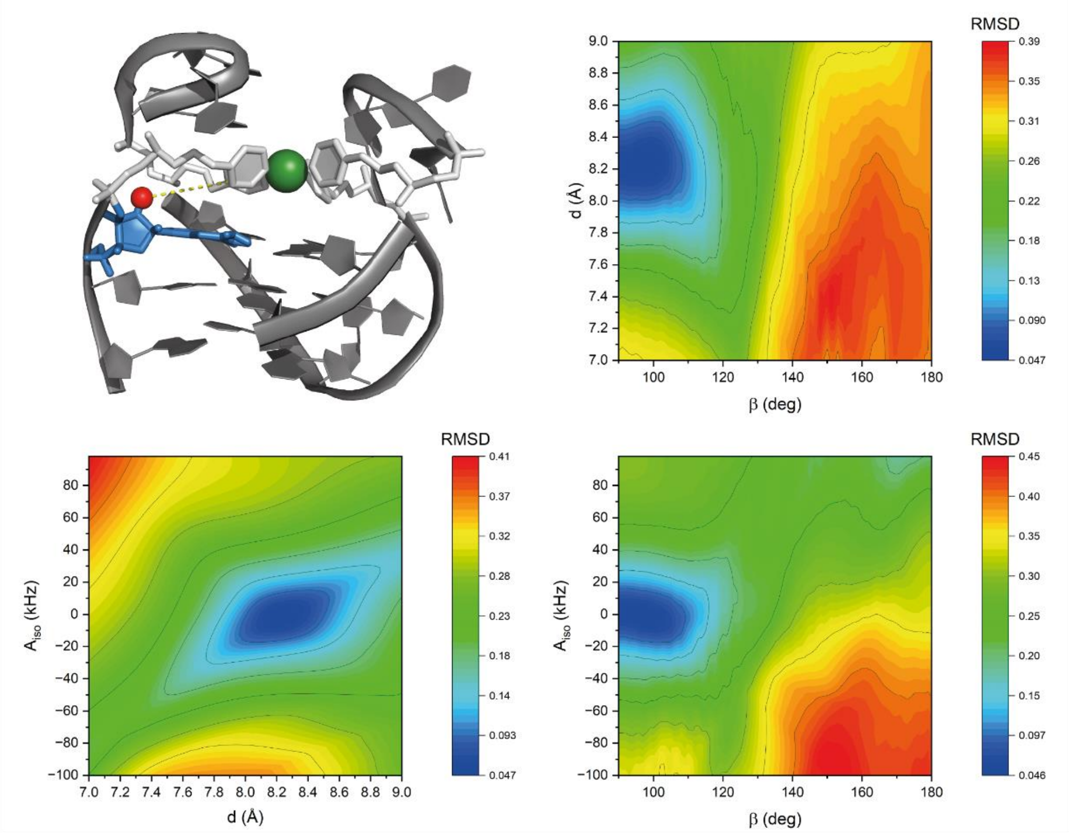
RMSD
9.0
8.8
8.6
8.4
8.2
8.0
7.8
7.6
7.4
7.2
7.0
d (Å)
100
120
140
160
180
β (deg)
0.39
0.35
0.31
0.26
0.22
0.18
0.13
0.090
0.047
RMSD
80
60
40
20
0
−20
−40
−60
−80
−100
A_iso (kHz)
7.0
7.2
7.4
7.6
7.8
8.0
8.2
8.4
8.6
8.8
9.0
d (Å)
0.41
0.37
0.32
0.28
0.23
0.18
0.14
0.093
0.047
RMSD
A_iso (kHz)
β (deg)
0.45
0.40
0.35
0.30
0.25
0.20
0.15
0.097
0.046

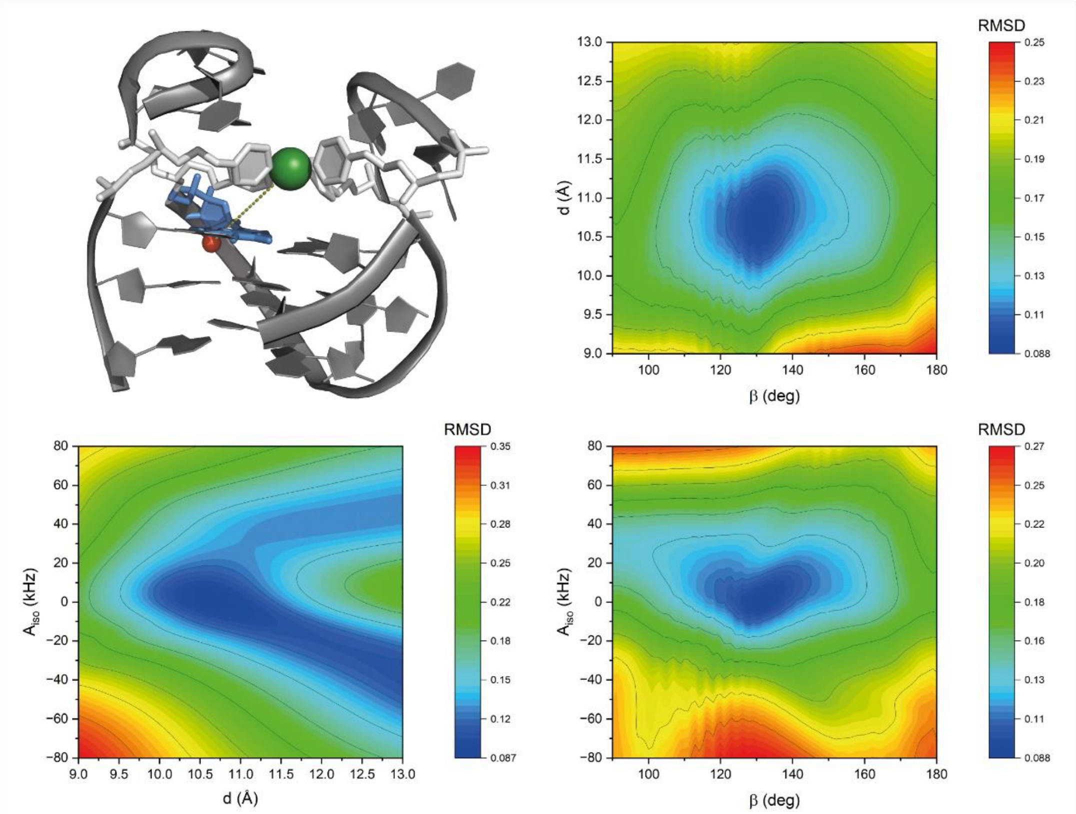
RMSD
13.0
12.5
12.0
11.5
11.0
10.5
10.0
9.5
9.0
d (Å)
100
120
140
160
180
β (deg)
0.25
0.23
0.21
0.19
0.17
0.15
0.13
0.11
0.088
RMSD
80
60
40
20
0
−20
−40
−60
−80
A_iso (kHz)
9.0
9.5
10.0
10.5
11.0
11.5
12.0
12.5
13.0
d (Å)
0.35
0.31
0.28
0.25
0.22
0.18
0.15
0.12
0.087
RMSD
A_iso (kHz)
β (deg)
0.27
0.25
0.22
0.20
0.18
0.16
0.13
0.11
0.088

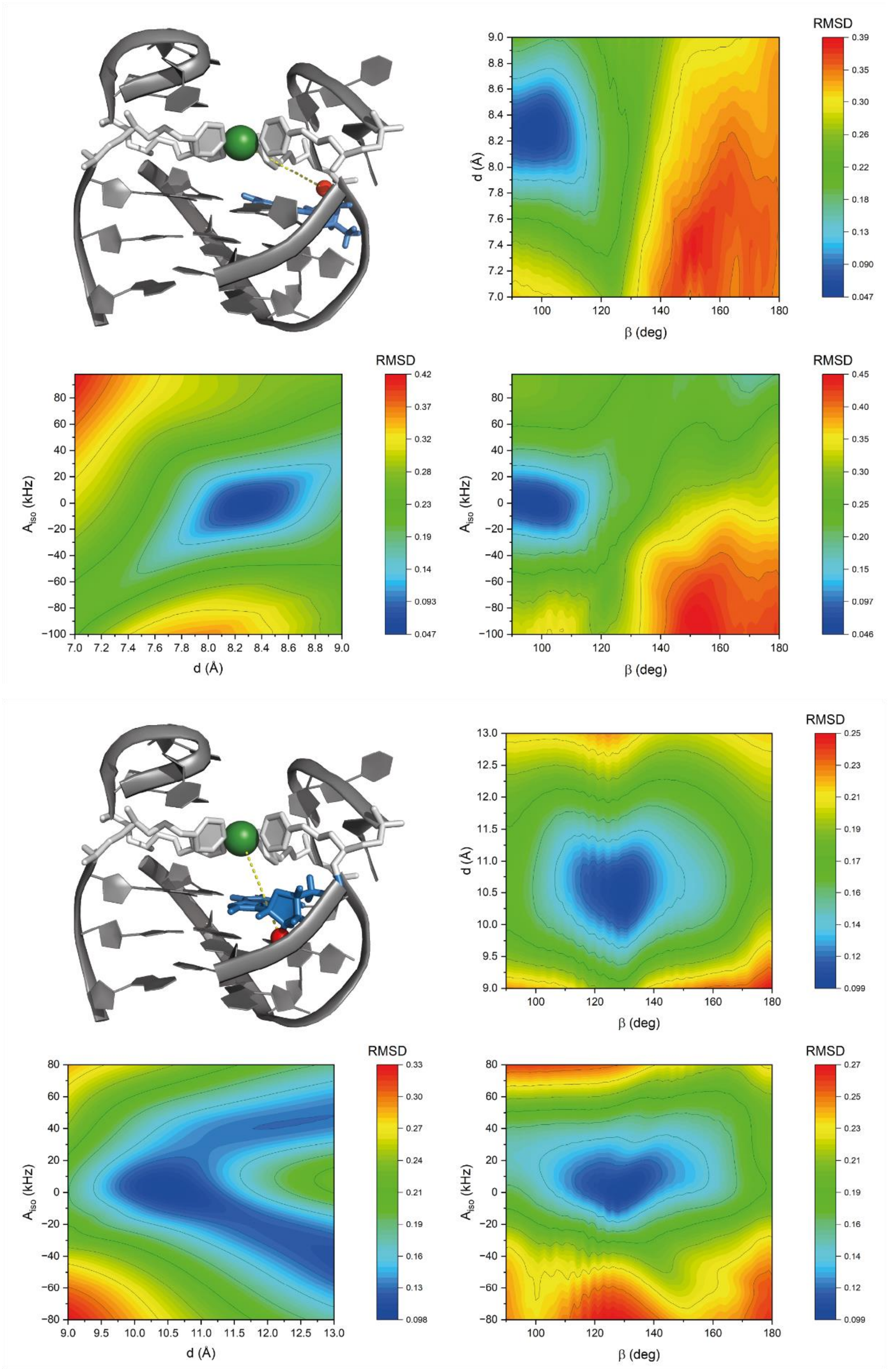

Figure S8: RMSD heatmap plots for **GQ1** – **GQ4** (top to bottom) for the ^{19}F angular position (*b*), inter-spin Cu^{2+}–^{19}F distance (*d*), and the isotropic hf term (A_{iso}), used to fit the orientation-selective ENDOR data (**Figure 22**) with the resulting 3D structure and connecting vector (yellow dashed) between Cu^{2+} (green sphere) and ^{19}F (red sphere) in the top left corner. Each heatmap is plotted for a pair of fitting parameters, with the third parameter set to its optimized value.

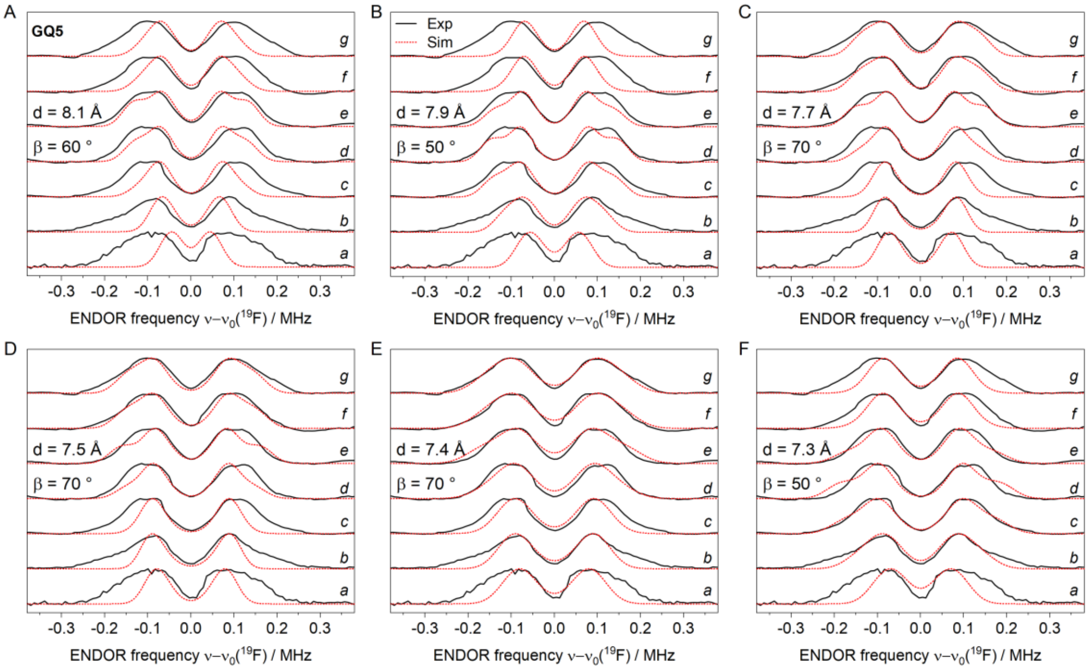

Figure S9: Normalized orientation-selective ^{19}F Mims ENDOR spectra of **GQ5** (black traces) overlaid with spectral simulations (red dotted traces) for six sets of inter-spin distance and angular position values (A_{iso} = 0 was assumed in all cases; the ENDOR broadening was 60 kHz in A–D, 80 kHz in E and 70 kHz in F, other parameters indicated in the figure).

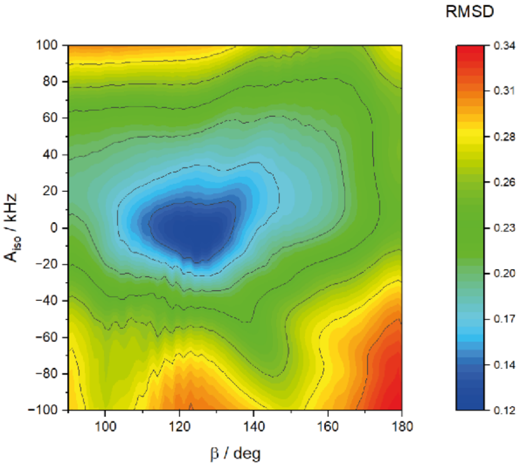
RMSD
0.34
0.31
0.28
0.26
0.23
0.20
0.17
0.14
0.12
A_{iso} / kHz
100
80
60
40
20
0
−20
−40
−60
−80
−100
100
120
140
160
180
β / deg

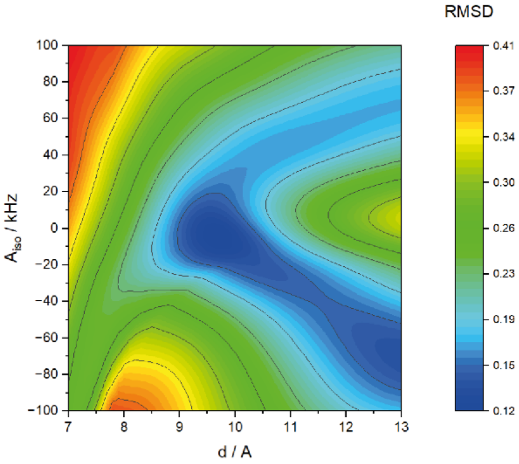
RMSD
0.41
0.37
0.34
0.30
0.26
0.23
0.19
0.15
0.12
A_{iso} / kHz
100
80
60
40
20
0
−20
−40
−60
−80
−100
7
8
9
10
11
12
13
d / A

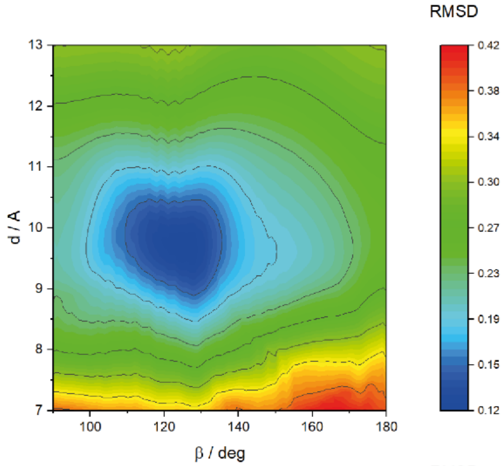
RMSD
0.42
0.38
0.34
0.30
0.27
0.23
0.19
0.15
0.12
d / A
13
12
11
10
9
8
7
100
120
140
160
180
β / deg

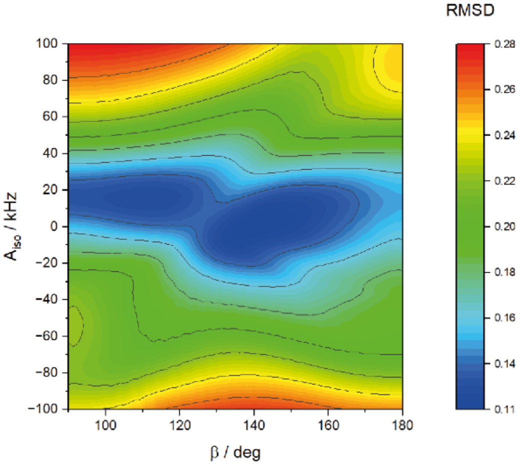
RMSD
0.28
0.26
0.24
0.22
0.20
0.18
0.16
0.14
0.11
A_{iso} / kHz
100
80
60
40
20
0
−20
−40
−60
−80
−100
100
120
140
160
180
β / deg

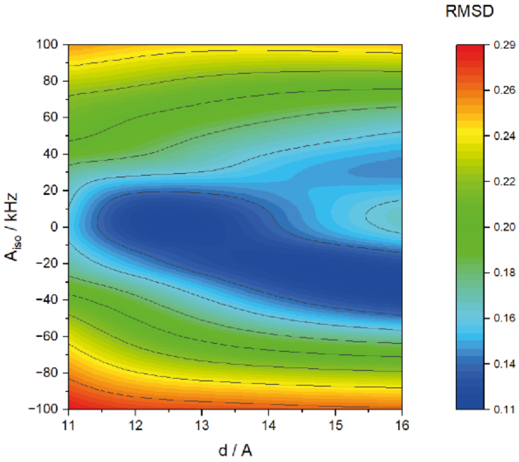
RMSD
0.29
0.26
0.24
0.22
0.20
0.18
0.16
0.14
0.11
A_{iso} / kHz
100
80
60
40
20
0
−20
−40
−60
−80
−100
11
12
13
14
15
16
d / A

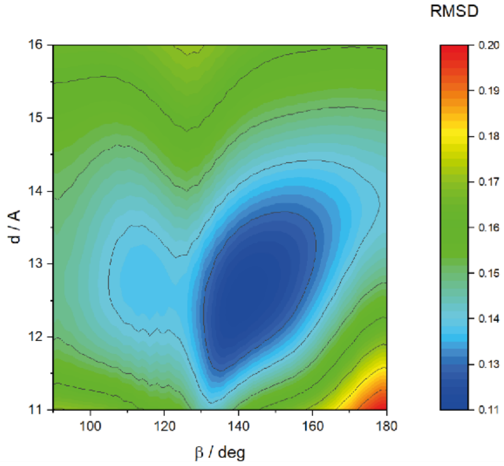
RMSD
0.20
0.19
0.18
0.17
0.16
0.15
0.14
0.13
0.11
d / A
16
15
14
13
12
11
100
120
140
160
180
β / deg

Figure S10: RMSD heatmap plots for **GQ6** and **GQ7** (top to bottom) for the ^{19}F angular position (β), inter-spin Cu^{2+}–^{19}F distance (d), and the isotropic hf term (A_{iso}), used to fit the orientation-selective ENDOR data (**Figure 32**). Each heatmap is plotted for a pair of fitting parameters, with the third parameter set to its optimized value.

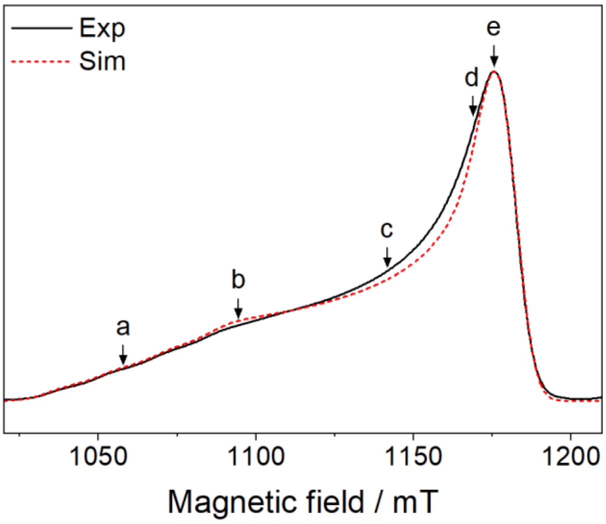

Figure S11: A representative echo-detected EPR spectrum for **Cat3** recorded at 34 GHz (black solid trace) with the corresponding simulation (red dashed trace). Simulation parameters are listed in the graph in **Figure 37**. Field positions where ENDOR spectra of **Cat1** – **Cat4** were measured are marked a to g.

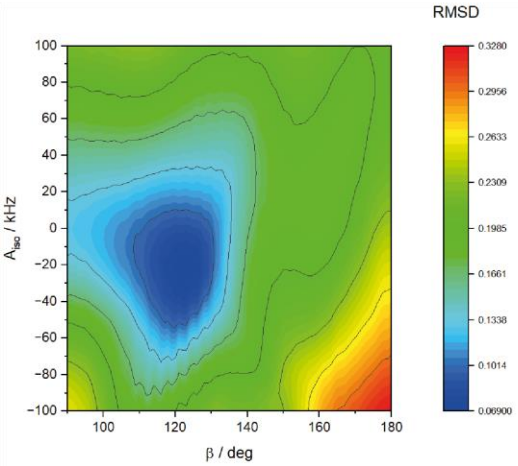
RMSD
A_iso / kHz
100
80
60
40
20
0
-20
-40
-60
-80
-100
100
120
140
160
180
β / deg
0.3280
0.2956
0.2633
0.2309
0.1985
0.1661
0.1338
0.1014
0.06900

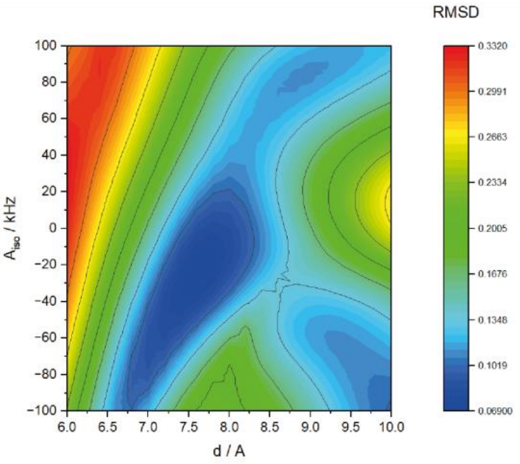
RMSD
A_iso / kHz
100
80
60
40
20
0
-20
-40
-60
-80
-100
6.0
6.5
7.0
7.5
8.0
8.5
9.0
9.5
10.0
d / A
0.3320
0.2991
0.2663
0.2334
0.2005
0.1676
0.1348
0.1019
0.06900

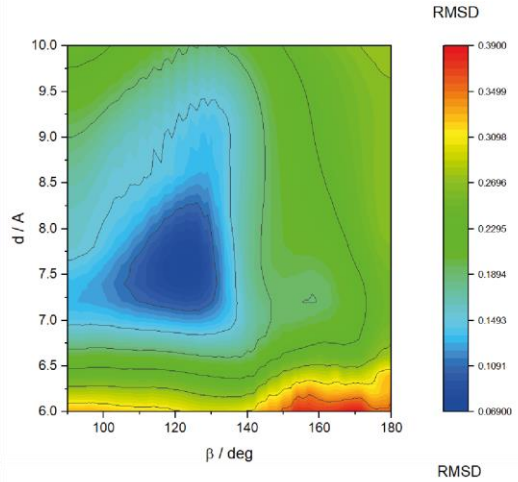
RMSD
d / A
10.0
9.5
9.0
8.5
8.0
7.5
7.0
6.5
6.0
100
120
140
160
180
β / deg
0.3900
0.3499
0.3098
0.2696
0.2295
0.1894
0.1493
0.1091
0.06900

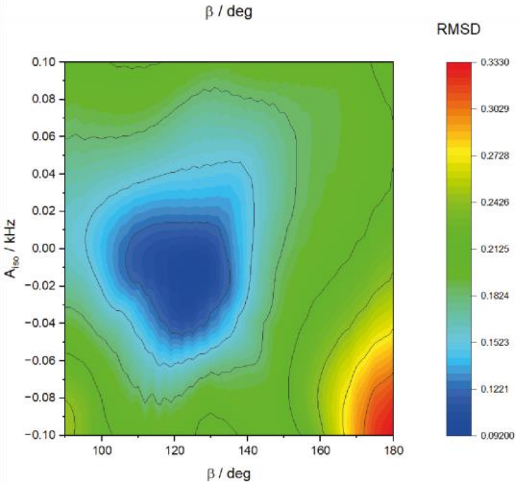
RMSD
A_iso / kHz
0.10
0.08
0.06
0.04
0.02
0.00
-0.02
-0.04
-0.06
-0.08
-0.10
100
120
140
160
180
β / deg
0.3330
0.3029
0.2728
0.2426
0.2125
0.1824
0.1523
0.1221
0.09200

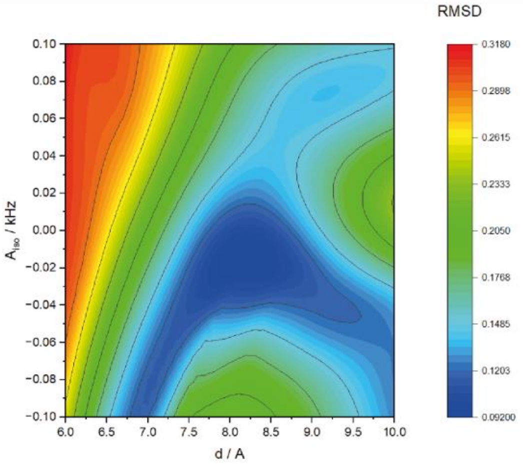
RMSD
A_iso / kHz
0.10
0.08
0.06
0.04
0.02
0.00
-0.02
-0.04
-0.06
-0.08
-0.10
6.0
6.5
7.0
7.5
8.0
8.5
9.0
9.5
10.0
d / A
0.3180
0.2898
0.2615
0.2333
0.2050
0.1768
0.1485
0.1203
0.09200

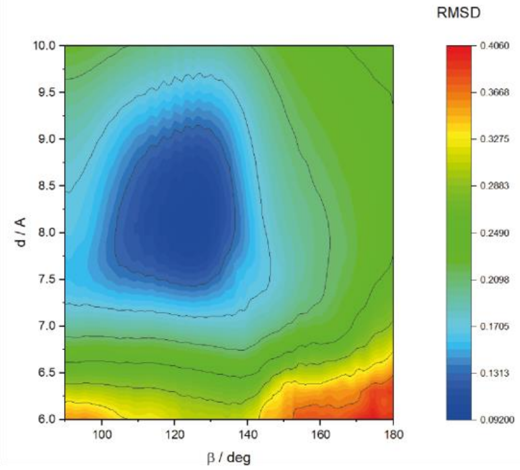
RMSD
d / A
10.0
9.5
9.0
8.5
8.0
7.5
7.0
6.5
6.0
100
120
140
160
180
β / deg
0.4060
0.3668
0.3275
0.2883
0.2490
0.2098
0.1705
0.1313
0.09200

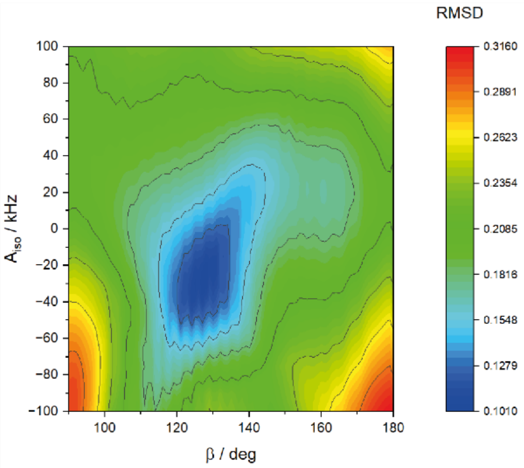
RMSD
0.3160
0.2891
0.2623
0.2354
0.2085
0.1816
0.1548
0.1279
0.1010
A_{iso} / kHz
100
80
60
40
20
0
−20
−40
−60
−80
−100
100
120
140
160
180
β / deg

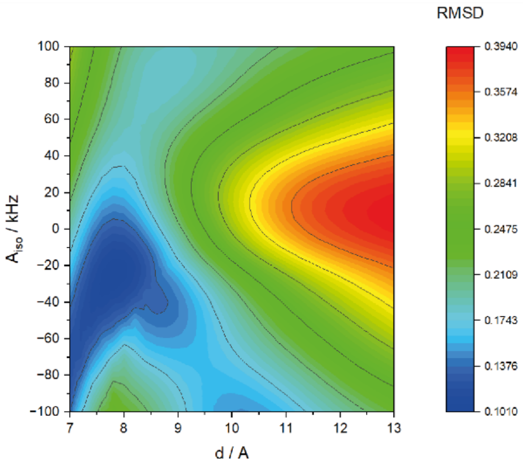
RMSD
0.3940
0.3574
0.3208
0.2841
0.2475
0.2109
0.1743
0.1376
0.1010
A_{iso} / kHz
100
80
60
40
20
0
−20
−40
−60
−80
−100
7
8
9
10
11
12
13
d / A

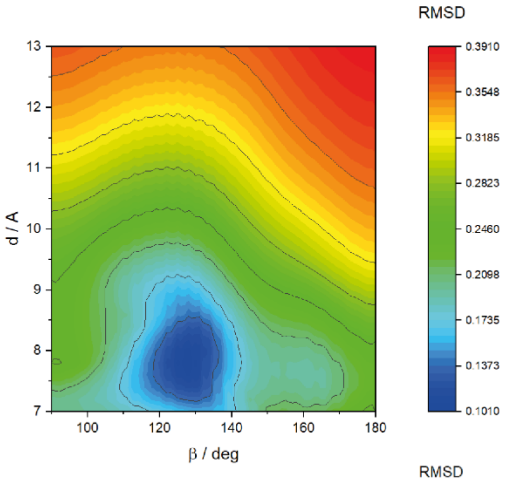
RMSD
0.3910
0.3548
0.3185
0.2823
0.2460
0.2098
0.1735
0.1373
0.1010
d / A
13
12
11
10
9
8
7
100
120
140
160
180
β / deg

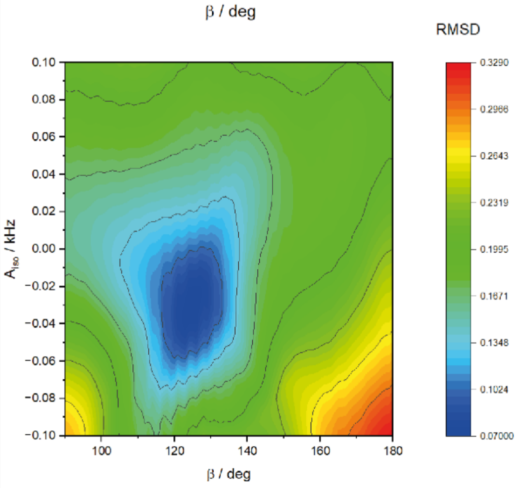
RMSD
0.3290
0.2966
0.2643
0.2319
0.1995
0.1671
0.1348
0.1024
0.07000
A_{iso} / kHz
0.10
0.08
0.06
0.04
0.02
0.00
−0.02
−0.04
−0.06
−0.08
−0.10
100
120
140
160
180
β / deg

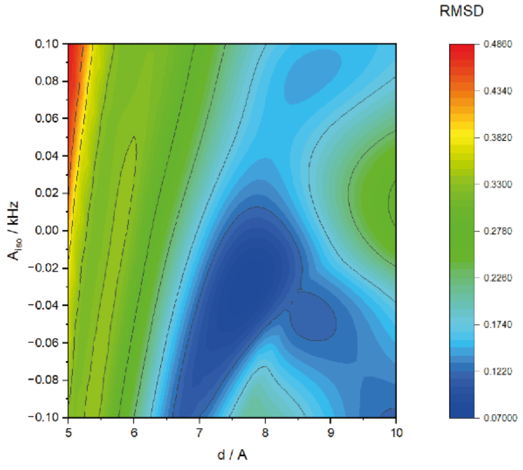
RMSD
0.4860
0.4340
0.3820
0.3300
0.2780
0.2260
0.1740
0.1220
0.07000
A_{iso} / kHz
0.10
0.08
0.06
0.04
0.02
0.00
−0.02
−0.04
−0.06
−0.08
−0.10
5
6
7
8
9
10
d / A

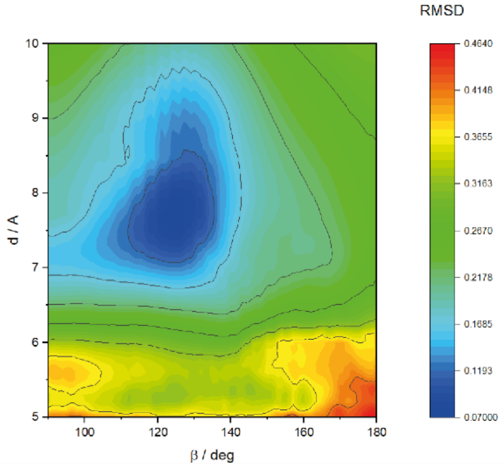
RMSD
0.4640
0.4148
0.3655
0.3163
0.2670
0.2178
0.1685
0.1193
0.07000
d / A
10
9
8
7
6
5
100
120
140
160
180
β / deg

Figure S12: RMSD heatmap plots for **Cat1** – **Cat4** (top to bottom) for the ^{19}F angular position (β), inter-spin Cu^{2+}–^{19}F distance (d), and the isotropic hf term (A_{iso}), used to fit the orientation-selective ENDOR data (**Figure 38**). Each heatmap is plotted for a pair of fitting parameters, with the third parameter set to its optimized value.

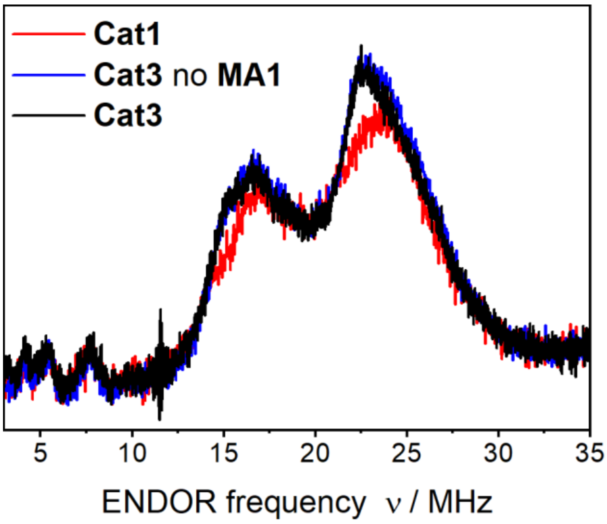

Figure S13: Comparison of ^{14}N Davies ENDOR spectra of **Cat1** (red) and **Cat3** with and without Michael addition reactant **MA1** (blue and black, respectively). The τ value for all three measurements is 450 ns with an optimized RF pulse length of 24 µs, T = 15 K.

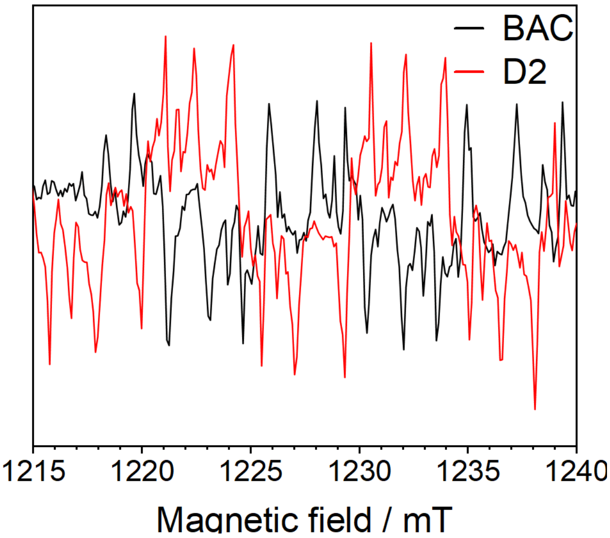

Figure S14: Oscillation in the background area of TE$_{011}$ (BAC, black) and D2 (red) of RNR measurements. The difference in direction results from opposite-phase tuning.

References

[1] I. Bertini, C. Luchinat, G. Parigi, R. Pierattelli, *ChemBioChem* **2005**, *6*, 1536–1549.

[2] M. Ubbink, J. A. R. Worrall, G. W. Canters, E. J. J. Groenen, M. Huber, *Annu. Rev. Biophys. Biomol. Struct.* **2002**, *31*, 393–422.

[3] J. Stubbe, D. G. Nocera, *J. Am. Chem. Soc.* **2021**, *143*, 13463–13472.

[4] S. L. Meichsner, Y. Kutin, M. Kasanmascheff, *Angew. Chem. Int. Ed.* **2021**, *60*, 19155–19161.

[5] W. Lubitz, F. Lendzian, R. Bittl, *Acc. Chem. Res.* **2002**, *35*, 313–320.

[6] S. Khorobrykh, V. Havurinne, H. Mattila, E. Tyystjärvi, *Plants* **2020**, *9*.

[7] G. T. Babcock, M. Wikström, *Nature* **1992**, *356*, 301–309.

[8] T. Presley, P. Kuppusamy, J. L. Zweier, G. Ilangovan, *Biophys. J.* **2006**, *91*, 4623–4631.

[9] A. Meyer, S. Dechert, S. Dey, C. Höbartner, M. Bennati, *Angew. Chem., Int. Ed.* **2020**, *132*, 381–387.

[10] H. Yu, *Proc. Natl. Acad. Sci.* **1999**, *96*, 332–334.

[11] G. Jeschke, *Annu. Rev. Phys. Chem.* **2012**, *63*, 419–446.

[12] G. Jeschke, in *EMagRes*, John Wiley & Sons, Ltd, Chichester, UK, **2016**.

[13] C. Riplinger, J. P. Y. Kao, G. M. Rosen, V. Kathirvelu, G. R. Eaton, S. S. Eaton, A. Kutateladze, F. Neese, *J. Am. Chem. Soc.* **2009**, *131*, 10092–10106.

[14] G. W. Reginsson, O. Schiemann, *Biochem. Soc. Trans.* **2011**, *39*, 128–139.

[15] M. Judd, E. H. Abdelkader, M. Qi, J. R. Harmer, T. Huber, A. Godt, A. Savitsky, G. Otting, N. Cox, *Phys Chem Chem Phys* **2022**, *24*, 25214–25226.

[16] A. Meyer, A. Kehl, C. Cui, F. A. K. Reichardt, F. Hecker, L.-M. Funk, M. K. Ghosh, K.-T. Pan, H. Urlaub, K. Tittmann, J. Stubbe, M. Bennati, *J. Am. Chem. Soc.* **2022**, *144*, 11270–11282.

[17] A. Kehl, M. Hiller, F. Hecker, I. Tkach, S. Dechert, M. Bennati, A. Meyer, *J. Magn. Reson.* **2021**, *333*, 107091.

[18] S. L. Schumann, S. Kotnig, Y. Kutin, M. Drosou, L. M. Stratmann, Y. Streltsova, A. Schnegg, D. A. Pantazis, G. H. Clever, M. Kasanmascheff, *Chem. - Eur. J.* **2023**, *29*.

[19] N. B. Asanbaeva, A. A. Sukhanov, A. A. Diveikina, O. Y. Rogozhnikova, D. V. Trukhin, V. M. Tormyshev, A. S. Chubarov, A. G. Maryasov, A. M. Genaev, A. V. Shernyukov, G. E. Salnikov, A. A. Lomzov, D. V. Pyshnyi, E. G. Bagryanskaya, *Phys. Chem. Chem. Phys.* **2022**, *24*, 5982–6001.

[20] G. B. Wells, M. W. Makinen, *J. Am. Chem. Soc.* **1988**, *110*, 6343–6352.

[21] P.-P. Zänker, G. Jeschke, D. Goldfarb, *J. Chem. Phys.* **2005**, *122*, 024515.

[22] A. Giannoulis, Y. Ben-Ishay, D. Goldfarb, in *Rare-Earth Element Biochemistry: Characterization and Applications of Lanthanide-Binding Biomolecules* (Ed.: ["Joseph A. Cotruvo"]), Academic Press, **2021**, pp. 235–290.

[23] S. A. Shelke, S. Th. Sigurdsson, *Eur. J. Org. Chem.* **2012**, *2012*, 2291–2301.

[24] A. J. Fielding, M. G. Concilio, G. Heaven, M. A. Hollas, *Molecules* **2014**, *19*, 16998–17025.

[25] D. M. Engelhard, J. Nowack, G. H. Clever, *Angew. Chem., Int. Ed.* **2017**, *56*, 11640–11644.

[26] D. M. Engelhard, A. Meyer, A. Berndhäuser, O. Schiemann, G. H. Clever, *Chem. Commun. (Cambridge, U. K.)* **2018**, *54*, 7455–7458.

[27] L. M. Stratmann, Y. Kutin, M. Kasanmascheff, G. H. Clever, *Angew. Chem., Int. Ed.* **2021**, *60*, 4939–4947.

[28] J. McCoy, W. L. Hubbell, *Proc. Natl. Acad. Sci.* **2011**, *108*, 1331–1336.

[29] M. T. Lerch, Z. Yang, C. Altenbach, W. L. Hubbell, in *Methods in Enzymology* (Eds.: ["Peter Z Qin", "Kurt Warncke"]), Academic Press, **2015**, pp. 29–57.

[30] K. M. Schultz, C. S. Klug, *Appl. Magn. Reson.* **2017**, *48*, 1341–1353.

[31] R. Winter, J. Jonas, *High Pressure Chemistry, Biochemistry and Materials Science*, Springer Dordrecht, **1993**.

[32] F.-G. Klärner, F. Wurche, *J. prakt. Chem.* **2000**, *342*, 609–636.

[33] H. Tiltscher, H. Hofmann, *Chem. Eng. Sci.* **1987**, *42*, 959–977.

[34] E. Morild, *Adv. Protein Chem.* **1981**, *34*, 93–166.

[35] G. Weber, H. G. Drickamer, *Q. Rev. Biophys.* **1983**, *16*, 89–112.

[36] V. Serment-Moreno, K. Deng, X. Wu, J. Welti-Chanes, G. Velazquez, J. A. Torres, *Handbook of Food Chemistry*, Berlin, **2015**.

[37] J. M. Berg, J. L. Tymoczko, G. J. G. jr., L. Stryer, *Stryer Biochemie*, Heidelberg, **2018**.

[38] J. D. Watson, F. H. C. Crick, *Nature* **1953**, *171*, 737–738.

[39] M. H. F. Wilkins, A. R. Stokes, H. R. Wilson, *Nature* **1953**, *171*, 738–740.

[40] R. Wadkins, *Curr. Med. Chem.* **2000**, *7*, 1–15.

[41] J. L. Kadrmas, A. J. Ravin, N. B. Leontis, *Nucleic Acids Res.* **1995**, *23*, 2212–2222.

[42] C. Altona, J. A. Pikkemaat, F. J. Overmars, *Curr. Opin. Struct. Biol.* **1996**, *6*, 305–316.

[43] S. Chou, K. Chin, A. H. -J. Wang, *Nucleic Acids Res.* **2003**, *31*, 2461–2474.

[44] K. Hoogsteen, *Acta Crystallogr.* **1963**, *16*, 907–916.

[45] S. Takahashi, N. Sugimoto, *Acc. Chem. Res.* **2021**, *54*, 2110–2120.

[46] J. T. Davis, *Angew. Chem. Int. Ed.* **2004**, *43*, 668–698.

[47] T. M. Bryan, P. Baumann, *Mol. Biotechnol.* **2011**, *49*, 198–208.

[48] L. Oganesian, T. M. Bryan, *BioEssays* **2007**, *29*, 155–165.

[49] D. Bhattacharyya, G. M. Arachchilage, S. Basu, *Front. Chem.* **2016**, *4*, 38.

[50] S. Zhang, Y. Wu, W. Zhang, *ChemMedChem* **2014**, *9*, 899–911.

[51] S. Burge, G. N. Parkinson, P. Hazel, A. K. Todd, S. Neidle, *Nucleic Acids Res.* **2006**, *34*, 5402–5415.

[52] A. N. Lane, J. B. Chaires, R. D. Gray, J. O. Trent, *Nucleic Acids Res.* **2008**, *36*, 5482–5515.

[53] J. L. Huppert, *FEBS J.* **2010**, *277*, 3452–3458.

[54] D. Rhodes, H. J. Lipps, *Nucleic Acids Res.* **2015**, *43*, 8627–8637.

[55] G. N. Parkinson, M. P. H. Lee, S. Neidle, *Nature* **2002**, *417*, 876–880.

[56] K. W. Lim, S. Amrane, S. Bouaziz, W. Xu, Y. Mu, D. J. Patel, K. N. Luu, A. T. Phan, *J. Am. Chem. Soc.* **2009**, *131*, 4301–4309.

[57] K. N. Luu, A. T. Phan, V. Kuryavyi, L. Lacroix, D. J. Patel, *J. Am. Chem. Soc.* **2006**, *128*, 9963–9970.

[58] B. Heddi, A. T. Phan, *J. Am. Chem. Soc.* **2011**, *133*, 9824–9833.

[59] Y. Wang, D. J. Patel, *Biochemistry* **1992**, *31*, 8112–8119.

[60] A. Ambrus, D. Chen, J. Dai, T. Bialis, R. A. Jones, D. Yang, *Nucleic Acids Res.* **2006**, *34*, 2723–2735.

[61] Y. Wang, D. J. Patel, *Structure* **1993**, *1*, 263–282.

[62] D. Sen, W. Gilbert, *Biochemistry* **1992**, *31*, 65–70.

[63] Y. Krishnan-Ghosh, D. Liu, S. Balasubramanian, *J. Am. Chem. Soc.* **2004**, *126*, 11009–11016.

[64] Y. Kato, T. Ohyama, H. Mita, Y. Yamamoto, *Journal of the American Chemical Society* **2005**, *127*, 9980–9981.

[65] T. C. Marsh, E. Henderson, *Biochemistry* **1994**, *33*, 10718–10724.

[66] K. Bose, C. J. Lech, B. Heddi, A. T. Phan, *Nat. Commun.* **2018**, *9*, 1959.

[67] V. Kuryavyi, A. T. Phan, D. J. Patel, *Nucleic Acids Res.* **2010**, *38*, 6757–6773.

[68] V. T. Mukundan, N. Q. Do, A. T. Phan, *Nucleic Acids Res.* **2011**, *39*, 8984–8991.

[69] M. Adrian, D. J. Ang, C. J. Lech, B. Heddi, A. Nicolas, A. T. Phan, *J. Am. Chem. Soc.* **2014**, *136*, 6297–6305.

[70] S. Kolesnikova, E. A. Curtis, *Molecules* **2019**, *24*, 3074.

[71] F.-Y. Teng, Z.-Z. Jiang, M. Guo, X.-Z. Tan, F. Chen, X.-G. Xi, Y. Xu, *Cell. Mol. Life Sci.* **2021**, *78*, 6557–6583.

[72] E. Henderson, C. C. Hardin, S. K. Walk, I. Tinoco, E. H. Blackburn, *Cell* **1987**, *51*, 899–908.

[73] D. Sen, W. Gilbert, *Nature* **1988**, *334*, 364–366.

[74] W. I. Sundquist, A. Klug, *Nature* **1989**, *342*, 825–829.

[75] S. Neidle, *Nat. Rev. Chem.* **2017**, *1*, 0041.

[76] R. Hänsel-Hertsch, M. D. Antonio, S. Balasubramanian, *Nat. Rev. Mol. Cell Biol.* **2017**, *18*, 279–284.

[77] G. Biffi, D. Tannahill, J. McCafferty, S. Balasubramanian, *Nat. Chem.* **2013**, *5*, 182–186.

[78] T. Tian, Y.-Q. Chen, S.-R. Wang, X. Zhou, *Chem* **2018**, *4*, 1314–1344.

[79] M. A. Blasco, *Nat. Rev. Genet.* **2005**, *6*, 611–622.

[80] M. L. Bochman, K. Paeschke, V. A. Zakian, *Nat. Rev. Genet.* **2012**, *13*, 770–780.

[81] S. Haider, G. N. Parkinson, S. Neidle, *Biophys. J.* **2008**, *95*, 296–311.

[82] H.-Q. Yu, D. Miyoshi, N. Sugimoto, *J. Am. Chem. Soc.* **2006**, *128*, 15461–15468.

[83] L. Petraccone, J. O. Trent, J. B. Chaires, *J. Am. Chem. Soc.* **2008**, *130*, 16530–16532.

[84] D. Renčiuk, I. Kejnovská, P. Školáková, K. Bednářová, J. Motlová, M. Vorlíčková, *Nucleic Acids Res.* **2009**, *37*, 6625–6634.

[85] S. Neidle, *FEBS Journal* **2010**, *277*, 1118–1125.

[86] N. S. Ilyinsky, A. M. Varizhuk, A. D. Beniaminov, M. A. Puzanov, A. K. Shchyolkina, D. N. Kaluzhny, *Mol. Biol.* **2014**, *48*, 778–794.

[87] L. A. Yatsunyk, O. Piétrement, D. Albrecht, P. L. T. Tran, D. Renčiuk, H. Sugiyama, J.-M. Arbona, J.-P. Aimé, J.-L. Mergny, *ACS Nano* **2013**, *7*, 5701–5710.

[88] X. Liu, J. Zhang, M. Fadeev, Z. Li, V. Wulf, H. Tian, I. Willner, *Chem. Sci.* **2019**, *10*, 1008–1016.

[89] J.-L. Mergny, D. Sen, *Chem. Rev.* **2019**, *119*, 6290–6325.

[90] C. Mao, W. Sun, Z. Shen, N. C. Seeman, *Nature* **1999**, *397*, 144–146.

[91] C. Mao, W. Sun, N. C. Seeman, *Nature* **1997**, *386*, 137–138.

[92] P. W. K. Rothemund, *Nature* **2006**, *440*, 297–302.

[93] E. S. Andersen, M. Dong, M. M. Nielsen, K. Jahn, R. Subramani, W. Mamdouh, M. M. Golas, B. Sander, H. Stark, C. L. P. Oliveira, J. S. Pedersen, V. Birkedal, F. Besenbacher, K. V. Gothelf, J. Kjems, *Nature* **2009**, *459*, 73–76.

[94] C. K. McLaughlin, G. D. Hamblin, H. F. Sleiman, *Chem. Soc. Rev.* **2011**, *40*, 5647–5656.

[95] N. C. Seeman, H. F. Sleiman, *Nat. Rev. Mater.* **2017**, *3*, 17068.

[96] P. F. McMillan, *Chem. Soc. Rev.* **2006**, *35*, 855–857.

[97] N. Erkan, G. Üretener, H. Alpas, *Innov. Food Sci. Emerg. Technol.* **2010**, *11*, 259–264.

[98] K. Yamamoto, *Biosci., Biotechnol., Biochem.* **2017**, *81*, 1–8.

[99] A. J. Baldwin, L. E. Kay, *Nat. Chem. Biol.* **2009**, *5*, 808–814.

[100] B. F. Volkman, D. Lipson, D. E. Wemmer, D. Kern, *Science* **2001**, *291*, 2429–2433.

[101] P. Li, I. R. S. Martins, G. K. Amarasinghe, M. K. Rosen, *Nat. Struct. Mol. Biol.* **2008**, *15*, 613–618.

[102] H. Frauenfelder, F. Parak, R. D. Young, *Annu. Rev. Biophys. Biophys. Chem.* **1988**, *17*, 451–479.

[103] J.-M. Knop, S. Mukherjee, M. W. Jaworek, S. Kriegler, M. Manisegaran, Z. Fetahaj, L. Ostermeier, R. Oliva, S. Gault, C. S. Cockell, R. Winter, *Chem. Rev.* **2023**, *123*, 73–104.

[104] K. Henzler-Wildman, D. Kern, *Nature* **2007**, *450*, 964–972.

[105] D. M. Korzhnev, I. Bezsonova, S. Lee, T. V. Chalikian, L. E. Kay, *J. Mol. Biol.* **2009**, *386*, 391–405.

[106] R. P. Venkitakrishnan, E. Zaborowski, D. McElheny, S. J. Benkovic, H. J. Dyson, P. E. Wright, *Biochemistry* **2004**, *43*, 16046–16055.

[107] D. M. Korzhnev, T. L. Religa, W. Banachewicz, A. R. Fersht, L. E. Kay, *Science* **2010**, *329*, 1312–1316.

[108] R. Kitahara, A. K. Simorellis, K. Hata, A. Maeno, S. Yokoyama, S. Koide, K. Akasaka, *Biophys. J.* **2012**, *102*, 916–926.

[109] P. Neudecker, P. Robustelli, A. Cavalli, P. Walsh, P. Lundström, A. Zarrine-Afsar, S. Sharpe, M. Vendruscolo, L. E. Kay, *Science* **2012**, *336*, 362–366.

[110] G. Bouvignies, P. Vallurupalli, D. F. Hansen, B. E. Correia, O. Lange, A. Bah, R. M. Vernon, F. W. Dahlquist, D. Baker, L. E. Kay, *Nature* **2011**, *477*, 111–114.

[111] A. Manglik, T. H. Kim, M. Masureel, C. Altenbach, Z. Yang, D. Hilger, M. T. Lerch, T. S. Kobilka, F. S. Thian, W. L. Hubbell, R. S. Prosser, B. K. Kobilka, *Cell* **2015**, *161*, 1101–1111.

[112] T. Q. Luong, S. Kapoor, R. Winter, *ChemPhysChem* **2015**, *16*, 3555–3571.

[113] B. Barstow, N. Ando, C. U. Kim, S. M. Gruner, *Proc. Natl. Acad. Sci.* **2008**, *105*, 13362–13366.

[114] J. L. Silva, A. C. Oliveira, T. C. R. G. Vieira, G. A. P. de Oliveira, M. C. Suarez, D. Foguel, *Chem. Rev.* **2014**, *114*, 7239–7267.

[115] K. Akasaka, *Chem. Rev.* **2006**, *106*, 1814–1835.

[116] R. Kitahara, S. Yokoyama, K. Akasaka, *J. Mol. Biol.* **2005**, *347*, 277–285.

[117] K. Kuwata, H. Li, H. Yamada, C. A. Batt, Y. Goto, K. Akasaka, *J. Mol. Biol.* **2001**, *305*, 1073–1083.

[118] R. Fourme, E. Girard, K. Akasaka, *Curr. Opin. Struct. Biol.* **2012**, *22*, 636–642.

[119] F. Meersman, I. Daniel, D. H. Bartlett, R. Winter, R. Hazael, P. F. McMillan, *Rev. Miner. Geochem.* **2013**, *75*, 607–648.

[120] J. L. Silva, G. Weber, *Annu. Rev. Phys. Chem.* **1993**, *44*, 89–113.

[121] V. V. Mozhaev, K. Heremans, J. Frank, P. Masson, C. Balny, *Proteins* **1996**, *24*, 81–91.

[122] H. -D. Lüdemann, *Makromol. Chem. Macromol. Symp.* **1988**, *17*, 29–38.

[123] R. Winter, D. Lopes, S. Grudzielanek, K. Vogtt, *J. Non-Equilib. Thermodyn.* **2007**, *32*, 41–97.

[124] J. Roche, C. A. Royer, *J. R. Soc. Interface* **2018**, *15*, 20180244.

[125] O. I. Gromov, M. O. Kostenko, A. V. Petrunin, A. A. Popova, O. O. Parenago, N. V. Minaev, E. N. Golubeva, M. Ya. Melnikov, *Polymers* **2021**, *13*, 3059.

[126] S. Sinha, R. Srinivasan, *Rev. Sci. Instrum.* **1983**, *54*, 1492–1496.

[127] S. K. Hoffmann, M. Krupski, W. Hilczer, *Appl. Magn. Reson.* **1993**, *5*, 407–424.

[128] A. MacRae, Z. Armstrong, M. Lenertz, Q. Li, A. Forge, M. Wang, L. Feng, W. Sun, Z. Yang, *Appl. Magn. Reson.* **2024**, *55*, 45–59.

[129] S. E. Bromberg, I. Y. Chan, *Rev. Sci. Instrum.* **1992**, *63*, 3670–3673.

[130] E. Zhecheva, R. Stoyanova, E. Shinova, *J. Mater. Sci.* **2007**, *42*, 3343–3348.

[131] Y. O. Kamatari, R. Kitahara, H. Yamada, S. Yokoyama, K. Akasaka, *Methods* **2004**, *34*, 133–143.

[132] D. R. Davydov, Z. Yang, N. Davydova, J. R. Halpert, W. L. Hubbell, *Biophys. J.* **2016**, *110*, 1485–1498.

[133] M. T. Lerch, Z. Yang, E. K. Brooks, W. L. Hubbell, *Proc. Natl. Acad. Sci.* **2014**, *111*, E1201–E1210.

[134] M. T. Lerch, J. Horwitz, J. McCoy, W. L. Hubbell, *Proc. Natl. Acad. Sci.* **2013**, *110*, E4714–E4722.

[135] M. T. Lerch, C. J. López, Z. Yang, M. J. Kreitman, J. Horwitz, W. L. Hubbell, *Proc. Natl. Acad. Sci.* **2015**, *112*, E2437–E2446.

[136] R. van Eldik, J. Jonas, Eds. , *High Pressure Chemistry and Biochemistry*, Springer Dordrecht, **1987**.

[137] M. Gross, R. Jaenicke, *Eur. J. Biochem.* **1994**, *221*, 617–630.

[138] K. Heremans, *Annu. Rev. Biophys. Bioeng.* **1982**, *11*, 1–21.

[139] R. V. Eldik, T. Asano, W. J. L. Noble, *Chem. Rev.* **1989**, *89*, 549–688.

[140] E. Zavoisky, *J. Phys. Ussr.* **1945**, *9*, 211–245.

[141] P. R. Levstein, C. A. Steren, A. M. Gennaro, R. Calvo, *Chem. Phys.* **1988**, *120*, 449–459.

[142] G. Mitrikas, Y. Deligiannakis, C. C. Trapalis, N. Boukos, G. Kordas, *J. Sol-Gel Sci. Technol.* **1998**, *13*, 503–508.

[143] J. McCracken, *J. Am. Chem. Soc.* **2009**, *131*, 13181–13181.

[144] A. Schweiger, G. Jeschke, *Principles of Pulse Electron Paramagnetic Resonance*, Oxford University Press On Demand, **2001**.

[145] J. P. Klare, H.-J. Steinhoff, *Photosynth. Res.* **2009**, *102*, 377–390.

[146] D. Marsh, *Mol. Biol. Biochem. Biophys.* **1981**, *31*, 51–142.

[147] M. Heinz, N. Erlenbach, L. S. Stelzl, G. Thierolf, N. R. Kamble, S. T. H. Sigurdsson, T. F. Prisner, G. Hummer, *Nucleic Acids Res.* **2019**, *48*, 924–933.

[148] J. S. Hyde, D. D. Thomas, *Ann. N. York Acad. Sci.* **1973**, *222*, 680–692.

[149] D. Goldfarb, S. Stoll, *EPR Spectroscopy: Fundamentals and Methods*, John Wiley & Sons, **2018**.

[150] F. J. Belinfante, *Physica* **1939**, *6*, 887–898.

[151] A. Kehl, M. Hiller, F. Hecker, I. Tkach, S. Dechert, M. Bennati, A. Meyer, *J. Magn. Reson.* **2021**, *333*, 107091.

[152] T. Prisner, M. Rohrer, F. MacMillan, *Annu. Rev. Phys. Chem.* **2001**, *52*, 279–313.

[153] D. Goldfarb, *J. Magn. Reson.* **2019**, *306*, 102–108.

[154] E. L. Hahn, *Phys. Rev.* **1950**, *80*, 580–594.

[155] K. M. Salikhov, S. A. Dzuba, A. M. Raitsimring, *J. Magn. Reson.* **1981**, *42*, 255–276.

[156] J. Casto, A. Mandato, S. Saxena, *J. Phys. Chem. Lett.* **2021**, *12*, 4681–4685.

[157] E. R. Davies, *Phys. Lett.* **1974**, *47*, 1–2.

[158] W. B. Mims, *Proc. R. Soc. Lond. A Math. Phys. Sci.* **1965**, *283*, 452–457.

[159] P. M. Punt, M. D. Langenberg, O. Altan, G. H. Clever, *J. Am. Chem. Soc.* **2021**, *143*, 3555–3561.

[160] D. M. Engelhard, R. Pievo, G. H. Clever, *Angew. Chem., Int. Ed.* **2013**, *52*, 12843–12847.

[161] D. M. Engelhard, L. M. Stratmann, G. H. Clever, *Chem. - Eur. J.* **2018**, *24*, 2117–2125.

[162] P. M. Punt, G. H. Clever, *Chem. Sci.* **2019**, *10*, 2513–2518.

[163] D. M. Engelhard, J. Nowack, G. H. Clever, *Angew. Chem., Int. Ed.* **2017**, *56*, 11640–11644.

[164] P. M. Punt, G. H. Clever, *Chem. - Eur. J.* **2019**, *25*, 13987–13993.

[165] Z. Li, C. J. Lech, A. T. Phan, *Nucleic Acids Res.* **2014**, *42*, 4068–4079.

[166] J. Dickerhoff, L. Haase, W. Langel, K. Weisz, *ACS Chem. Biol.* **2017**, *12*, 1308–1315.

[167] N. Martín-Pintado, M. Yahyaee-Anzahaee, G. F. Deleavey, G. Portella, M. Orozco, M. J. Damha, C. González, *J. Am. Chem. Soc.* **2013**, *135*, 5344–5347.

[168] J. S. Hyde, M. Pasenkiewicz-Gierula, A. Jesmanowicz, W. E. Antholine, *Appl. Magn. Reson.* **1990**, *1*, 483.

[169] B. Kozlevcar, P. Šegedin, *Croatica Chemica Acta* **2008**, *81*, 369–379.

[170] A. Folli, N. Ritterskamp, E. Richards, J. A. Platts, D. M. Murphy, *J. Catal.* **2021**, *394*, 220–227.

[171] D. M. Engelhard, A. Meyer, A. Berndhäuser, O. Schiemann, G. H. Clever, *Chem. Commun.* **2018**, *54*, 7455–7458.

[172] G. G. Hurst, T. A. Henderson, R. W. Kreilick, *J. Am. Chem. Soc.* **1985**, *107*, 7294–7299.

[173] T. A. Henderson, G. C. Hurst, R. W. Kreilick, *J. Am. Chem. Soc.* **1985**, *107*, 7299–7303.

[174] S. Stoll, A. Schweiger, *J. Magn. Reson.* **2006**, *178*.

[175] M. Drosou, C. A. Mitsopoulou, M. Orio, D. A. Pantazis, *Magnetochemistry* **2022**, *8*.

[176] M. van Gastel, G. W. Canters, H. Krupka, A. Messerschmidt, E. C. de Waal, G. C. M. Warmerdam, E. J. J. Groenen, *J. Am. Chem. Soc.* **2000**, *122*, 2322–2328.

[177] F. D. Breitgoff, K. Keller, M. Qi, D. Klose, M. Yulikov, A. Godt, G. Jeschke, *J. Magn. Reson.* **2019**, *308*, 106560.

[178] G. R. Eaton, S. S. Eaton, in *Multifrequency Electron Paramagnetic Resonance*, **2011**, pp. 719–753.

[179] C. E. Jackson, C.-Y. Lin, J. van Tol, J. M. Zadrozny, *Chem. Phys. Lett.* **2020**, *739*, 137034.

[180] A. Collauto, H. A. DeBerg, R. Kaufmann, W. N. Zagotta, S. Stoll, D. Goldfarb, *Phys. Chem. Chem. Phys.* **2017**, *19*, 15324–15334.

[181] D. M. Engelhard, R. Pievo, G. H. Clever, *Angew. Chem., Int. Ed.* **2013**, *52*, 12843–12847.

[182] J. Zhao, D. G. Bachmann, M. Lenz, D. G. Gillingham, T. R. Ward, *Catal. Sci. Technol.* **2018**, *8*, 2294–2298.

[183] P. Srivastava, H. Yang, K. Ellis-Guardiola, J. C. Lewis, *Nat. Commun.* **2015**, *6*, 7789.

[184] I. Drienovská, C. Mayer, C. Dulson, G. Roelfes, *Nat. Chem.* **2018**, *10*, 946–952.

[185] M. Hestericová, T. Heinisch, L. Alonso-Cotchico, J. Maréchal, P. Vidossich, T. R. Ward, *Angew. Chem. Int. Ed.* **2018**, *57*, 1863–1868.

[186] M. Jeschek, R. Reuter, T. Heinisch, C. Trindler, J. Klehr, S. Panke, T. R. Ward, *Nature* **2016**, *537*, 661–665.

[187] J. J. Marek, R. P. Singh, A. Heuer, U. Hennecke, *Chem. A Eur. J.* **2017**, *23*, 6004–6008.

[188] A. J. Boersma, B. L. Feringa, G. Roelfes, *Angew. Chem. Int. Ed.* **2009**, *48*, 3346–3348.

[189] G. Roelfes, B. L. Feringa, *Angew. Chem. Int. Ed.* **2005**, *44*, 3230–3232.

[190] S. Park, H. Matsui, K. Fukumoto, J. H. Yum, H. Sugiyama, *RSC Adv.* **2020**, *10*, 9717–9722.

[191] J. Mansot, J. Lauberteaux, A. Lebrun, M. Mauduit, J. Vasseur, R. M. de Figueiredo, S. Arseniyadis, J. Campagne, M. Smietana, *Chem. A Eur. J.* **2020**, *26*, 3519–3523.

[192] S. Roe, D. J. Ritson, T. Garner, M. Searle, J. E. Moses, *Chem. Commun.* **2010**, *46*, 4309–4311.

[193] C. Wang, G. Jia, J. Zhou, Y. Li, Y. Liu, S. Lu, C. Li, *Angew. Chem. Int. Ed.* **2012**, *51*, 9352–9355.

[194] J. Hao, W. Miao, Y. Cheng, S. Lu, G. Jia, C. Li, *ACS Catal.* **2020**, *10*, 6561–6567.

[195] C. Wang, Y. Li, G. Jia, Y. Liu, S. Lu, C. Li, *Chem. Commun.* **2012**, *48*, 6232–6234.

[196] C. Wang, G. Jia, Y. Li, S. Zhang, C. Li, *Chem. Commun.* **2013**, *49*, 11161–11163.

[197] J. H. Yum, S. Park, H. Sugiyama, *Org. Biomol. Chem.* **2019**, *17*, 9547–9561.

[198] J. F. Neault, H. A. Tajmir-Riahi, *Biophys. J.* **1999**, *76*, 2177–2182.

[199] N. V. Anantha, M. Azam, R. D. Sheardy, *Biochemistry* **1998**, *37*, 2709–2714.

[200] W. Bruggemann, J. R. Niklas, *J. Magn. Reson.* **1994**, *108*, 25–29.

[201] J.-D. Rochaix, M. Goldschmidt-Clermont, S. Merchant, Eds. , *The Molecular Biology of Chloroplasts and Mitochondria in Chlamydomonas*, **1998**.

[202] J.-D. Rochaix, *FEBS Lett.* **2002**, *529*, 34–38.

[203] F. Galván, A. J. Márquez, E. Fernández, *Z. für Naturforsch. C* **1985**, *40*, 373–378.

[204] K. Fukuyama, *Photosynth. Res.* **2004**, *81*, 289–301.

[205] A. Melis, T. Happe, *Plant Physiol.* **2001**, *127*, 740–748.

[206] I. Rasul, F. Azeem, M. H. Siddique, S. Muzammil, A. Rasul, A. Munawar, M. Afzal, M. A. Ali, H. Nadeem, **2017**, pp. 301–334.

[207] S. B. Mellor, K. Vavitsas, A. Z. Nielsen, P. E. Jensen, *Photosynth. Res.* **2017**, *134*, 329–342.

[208] C. H. Chang, P. W. King, M. L. Ghirardi, K. Kim, *Biophys. J.* **2007**, *93*, 3034–3045.

[209] S. Rumpel, J. F. Siebel, M. Diallo, C. Farès, E. J. Reijerse, W. Lubitz, *ChemBioChem* **2015**, *16*, 1663–1669.

[210] A. Günzel, V. Engelbrecht, T. Happe, *J. Biol. Inorg. Chem.* **2022**, *27*, 631–640.

[211] P. Hosseinzadeh, Y. Lu, *Biochim. Biophys. Acta* **2016**, *1857*, 557–581.

[212] J. Liu, S. Chakraborty, P. Hosseinzadeh, Y. Yu, S. Tian, I. Petrik, A. Bhagi, Y. Lu, *Chem. Rev.* **2014**, *114*, 4366–4469.

[213] Y. Takayama, M. Taketa-Sato, H. Komori, K. Morita, S.-J. Kang, Y. Higuchi, H. Akutsu, *Bull. Chem. Soc. Jpn.* **2011**, *84*, 1096–1101.

[214] G. Battistuzzi, M. Bellei, C. A. Bortolotti, M. Sola, *Arch. Biochem. Biophys.* **2010**, *500*, 21–36.

[215] E. D. Duée, E. Fanchon, J. Vicat, L. C. Sieker, J. Meyer, J.-M. Moulis, *J. Mol. Biol.* **1994**, *243*, 683–695.

[216] G. Backes, Y. Mino, T. M. Loehr, T. E. Meyer, M. A. Cusanovich, W. V. Sweeney, E. T. Adman, J. Sanders-Loehr, *J. Am. Chem. Soc.* **1991**, *113*, 2055–2064.

[217] Z. Dauter, K. S. Wilson, L. C. Sieker, J. Meyer, J.-M. Moulis, *Biochemistry* **1997**, *36*, 16065–16073.

[218] M. Heghmanns, A. Günzel, D. Brandis, Y. Kutin, V. Engelbrecht, M. Winkler, T. Happe, M. Kasanmascheff, *Biophys. Rep.* **2021**, *1*, 100016.

[219] N. L. Breton, J. J. Wright, A. J. Y. Jones, E. Salvadori, H. R. Bridges, J. Hirst, M. M. Roessler, *J. Am. Chem. Soc.* **2017**, *139*, 16319–16326.

[220] J. Jacobs, S. Pudollek, A. Hemschemeier, T. Happe, *FEBS Lett.* **2009**, *583*, 325–329.

[221] J. F. Cerda, C. X. Guzman, H. Zhang, E. J. Amendola, J. D. Castorino, N. Millet, A. L. Fritz, D. N. Houchins, M. H. Roeder, *Electrochem. Commun.* **2013**, *33*, 76–79.

[222] P. V. Bernhardt, *Chem. Methods* **2023**, *3*.

[223] Z. Fetahaj, L. Ostermeier, H. Cinar, R. Oliva, R. Winter, *J. Am. Chem. Soc.* **2021**, *143*, 5247–5259.

[224] H. Cinar, S. Cinar, H. S. Chan, R. Winter, *Chem. A Eur. J.* **2018**, *24*, 8286–8291.

[225] E. Reijerse, F. Lendzian, R. Isaacson, W. Lubitz, *J. Magn. Reson.* **2012**, *214*, 237–243.

[226] R. Tschaggelar, B. Kasumaj, M. G. Santangelo, J. Forrer, P. Leger, H. Dube, F. Diederich, J. Harmer, R. Schuhmann, I. García-Rubio, G. Jeschke, *J. Magn. Reson.* **2009**, *200*, 81–87.

[227] C. E. Davoust, P. E. Doan, B. M. Hoffman, *J. Magn. Reson., Ser. A* **1996**, *119*, 38–44.

[228] A. Sienkiewicz, B. G. Smith, A. Veselov, C. P. Scholes, *Rev. Sci. Instrum.* **1996**, *67*, 2134–2138.

[229] I. Gromov, J. Forrer, A. Schweiger, *Rev. Sci. Instrum.* **2006**, *77*, 064704.

[230] M. Judd, G. Jolley, D. Suter, N. Cox, A. Savitsky, *Appl. Magn. Reson.* **2022**, *53*, 963–977.

List of Figures

List of Tables

List of Abbreviations

A	*adenine*
C	*cysteine*
CW	*continous wave*
DEER	*Double electron-electron resonance*
DFT	*density functional theory*
DNA	*Deoxyribonucleic acid*
ENDOR	*Electron nuclear double resonance*
EPR	*Electron paramagnetic resonance*
ESE	*electron spin echo*
ESR	*electron spin resonance*
G	*guanine*
GQ	*G-quadruplex*
hf	*hyperfine interaction*
MD	*Molecular dynamic*
mRNA	*messenger ribonucleic acid*
mw	*microwave*
NMR	*Nuclear Magnetic Resonance*
OD	*outer diameter*
PTFE	*polytetrafluoroethylene*
RF	*radio frequency*
RMSD	*root-mean-square deviation*
S/N	*signal-to-noise ratio*
spp	*shots per point*
T	*thymine*
TEMPO	*(2,2,6,6-Tetramethylpiperidin-1-yl)oxyl or (2,2,6,6-tetramethylpiperidin-1-yl)oxidanyl*

List of used Tools

Matlab:	Used for simulation and analysis of EPR data, accessed through privately bought licenses and university licenses
EasySpin:	Simulation toolbox for EPR simulations in Matlab. Downloaded in its current active version from the EasySpin website.
Origin labs:	Graphic plotting program used to visualize EPR results and spectra, accessed via the Technical University Dortmund faculty license.
Illustrator:	Adobe graphic design software used for figure design. The license was acquired privately.
Word:	Used to write the PhD thesis and accessed through the Microsoft Office student package offered by the Technical University Dortmund, paid privately.
Grammarly:	Grammar, spelling, and AI writing assistant. It was used for spellchecking and grammar corrections in this thesis. Accessed through the official Grammarly website and privately paid for the Pro version.
Moxie AI:	Academic writing AI software. Used for feedback on the first four chapters of this thesis at the request of Prof. Kasanmascheff and accessed via the official Moxielearn website. The 7-day free test version was used.
PyMOL:	Used to generate figures of 3D DNA strucutres. The free version was downloaded from the PyMOL website and was used without a lisence.

Affidavit